Preliminary Destructive Examination Results for Sibling Pin Cladding

Spent Fuel and Waste Disposition

Prepared for
US Department of Energy
Spent Fuel and Waste Science and Technology

Argonne National Laboratory
M.C. Billone and T.A. Burtseva

February 28, 2020 Rev. 2
M3SF-20AN010201011
ANL-19/53 Rev. 2

SUMMARY

This report satisfies SFWD-SFWST-2020 milestone M3SF-20AN010201011.

The High Burnup Cask Demonstration Project (Demo Project) is being conducted to assess the integrity of high-burnup (HBU >45 gigawatt-days per metric ton of uranium) pressurized water reactor fuel rods under drying, long-term storage, and post-storage transport conditions. In support of this project, 25 fuel rods irradiated to HBU have been provided for characterization and testing: (a) 15 fuel rods for Oak Ridge National Laboratory (ORNL), (b) 10 fuel rods for Pacific Northwest National Laboratory (PNNL), and (c) the equivalent of about 1.4 m of defueled cladding for Argonne National Laboratory (ANL). The 25 fuel rods are referred to as sibling pins because they were either extracted from fuel assemblies loaded into the Demo Cask or from assemblies with irradiation histories similar to assemblies loaded into the Demo Cask. ANL's role in the test plan is to conduct characterization and testing to determine if cladding retains ductility following drying and long-term storage. Retaining ductility is desirable during all phases of storage and transportation, particularly during post-storage transport.

Twelve defueled sibling-pin cladding segments, each 90-mm long, were received from ORNL in May 2019. Six segments were in the as-irradiated condition: (a) M5® fuel rod 30AD05 (two axial locations), (b) ZIRLO® fuel rod 3D8E14 (two axial locations) and (c) low-tin Zircaloy-4 (Zry-4) fuel rod 3A1F05 (two axial locations). Six segments (two per rod) were sectioned from M5®, ZIRLO®, and Zry-4 fuel rods (30AE14, 3F9N05, and F35P17, respectively) subjected to heat treatment at 400°C peak cladding temperature (PCT) for 8 hours followed by cooling at ≤5°C/h. In accordance with the High-Burnup Spent Fuel Rod Phase 1 Test Plan, all 12 segments were inspected visually and preliminary destructive examinations were conducted on two M5® segments (baseline and heat-treated). Eight ring compression test (RCT) samples per segment were sectioned, deburred and squared. Future Argonne work will include characterization and RCTs for the 12 ORNL cladding segments, as well as cladding segments to be received from PNNL.

The axial location of the as-irradiated M5® segment (653B) was 3259−3349 mm from the bottom of fuel rod 30AD05. The outer diameter (9.38 mm) was measured at three axial locations and two orientations per location. Metallographic examination was performed for a sample at ≈3300 mm for measurement of oxide layer thickness (13±1 µm), metal outer diameter (9.35 mm), metal wall thickness (0.549 mm) and metal inner diameter (8.25 mm). Hydrides were oriented in the circumferential direction. Only two short radial hydrides (7−10% of cladding wall thickness) were observed. The oxide layer thickness and density of hydrides suggest 90±10 wppm hydrogen content, which requires direct-measurement confirmation. Based on previous experience, full RCT ductility is expected at 20°C.

The axial location of the heat-treated M5® segment was 3309-3399 mm from the bottom of fuel rod 30AE14. The average outer diameter was 9.41 mm. Metallographic examination was performed at two locations (3360 mm and 3390 mm from rod bottom) to determine metal outer diameter (9.39 mm), oxide layer thickness (10±1 µm), metal wall thickness (0.568 mm), and inner metal diameter (8.26 mm). The average hoop stress at the peak cladding temperature (PCT =401°C) was 52 MPa based on extrapolation of the measured internal pressure (3.2 MPa at 25°C). The hoop stress was higher during the initial overheating (485°C), but only the hoop stress at the beginning of the cooling ramp is significant with respect to radial hydride precipitation assuming that partial annealing of irradiation damage did not occur during the overheating. For the surface at 3360 mm, the maximum radial hydride length (i.e., radial hydride continuity factor [RHCF]) was about 60% of the cladding wall thickness with an average value of 22±15% based on 21 images at locations that included radial hydrides. For the surface

at 3390 mm, 46 overlapping images covering the full surface had average radial hydride lengths of 18±10% with a maximum value of about 50%. The average values were considerably lower than values for M5® subjected to higher hoop stresses: 44±18% for 89 MPa, 54±16% for 111 MPa and 62±17% for 142 MPa. Also, radial hydrides were not as continuous as those previously observed for samples subjected to higher hoop stresses prior to cooling. The procedure for continuity determination allows up to a 5-µm gap in the radial direction. Many of the hydrides that appeared continuous in 100X images were shown in 200X images to have gaps in the range of 1−5 µm and >5 µm between short radial hydrides. The observed radial hydrides do not appear to be damaging to RCT ductility even at room temperature. RCTs will be conducted to determine ductility as a function of test temperature.

Prior to initiating examination of the sibling-pin cladding, additional work was conducted to confirm the high ductility observed for the ring closest to the top, hollow end fixture of ZIRLO® rodlet 646B. The 646B ZIRLO® rodlet with 350±70 wppm hydrogen was subjected to peak conditions of 350°C and 96-MPa hoop stress for one hour prior to cooling at 5°C/h down to 130°C. Finite element analysis (FEA) calculations were used to determine the axial extent of the stress discontinuity region (5.6 mm from weld) and metallographic examinations were performed at 8 axial locations, including the hollow-insert/cladding region, to determine the RHCF as a function of axial location, cracking patterns, and gap between the top insert and the cladding. This work is important to the interpretation of data for this particular test, for tests conducted previously, and for providing guidance on sample selection for future testing. In simplistic terms, the average cladding hoop stress is essentially zero at the weld and increases to the pressurized-tube-predicted value beyond the stress discontinuity region.

The results of the analytical-experimental effort indicated that the ring tested at 170°C had a radial hydride fraction equivalent to the average value (24±9%) for samples farther away from top and bottom end fixtures. A similar approach was used to disqualify the high ductility exhibited at 100°C by the ring closest to the lower end cap with the solid insert. Thus, valid data points were generated for rings (other than the bottom ring) tested at 100°C (brittle), 120°C (brittle), 150°C (low ductility) and 170°C (full ductility). The ductility transition temperature (DTT) was about 140°C (143°C). By contrast, the 646D ZIRLO® rodlet, with essentially the same hydrogen content and dimensions, had a DTT of about 30°C (28°C) following cooling from 350°C and 87 MPa. Consistent with the ductility results for 646D, the RHCF for the 87-MPa rodlet was lower (19±10%). These results confirm the high sensitivity of ZIRLO® DTT to cladding hoop stress in the range of about 90±5 MPa at the peak cladding temperature. Previous results for stress levels of 88−89 MPa (ductile at room temperature) and 93-94 MPa (125−140°C DTT) showed the same trend, but these results included variables other than peak hoop stress: 350°C and 400°C PCT, 560−650 wppm hydrogen, one-to-three temperature cycles during heat treatment, controlled cooling down to 200°C and 130°C, and cladding dimensions.

FEA calculations were also conducted for as-fabricated M5® benchmark samples to correlate RCT structure ductility with the maximum material strain and to determine residual stresses following unloading. These results, along with the results for discontinuity stress length, will be used in the ASTM guidance documents for radial hydride treatment and for ductility determination from RCT load-displacement curves. The FEA results are significant because they are used to quantify regions of peak stress and strain at the 12 and 6 o'clock orientations (highest) and the 3 and 9 o'clock orientations (40% lower elastic tensile hoop stress). They also demonstrate that following elastic-plastic deformation, the unloaded ring contains significant residual stresses.

CONTENTS

FIGURES

TABLES

Page intentionally blank

REVISION HISTORY

Date	Revision	Changes
12/31/2019	0	Initial draft completion; distributed on 1/2/2020
1/3/2020	0	Updated M3SF Number; uploaded into PICS:NE
1/9/2020	1	Corrections based on Bruce Bevard's input
2/28/2020	2	Modifications: technical reviews by K. Sorenson & J. Kessler

Page intentionally blank

ACRONYMS, UNITS AND SYMBOLS

ACRONYMS

AF	as-fabricated
ANL	Argonne National Laboratory
CWSRA	cold-worked, stress-relief annealed
DOE	U.S. Department of Energy
DTT	ductility transition temperature
EPRI	Electric Power Research Institute
FEA	finite element analysis
FHT	full-length heat treatment
HAZ	heat-affected zone
HBU	high burnup
IFBA	integral fuel burnable absorber
KAERI	Korea Atomic Energy Research Institute
LT	low tin
NRC	Nuclear Regulatory Commission
ORNL	Oak Ridge National Laboratory
PCT	peak cladding temperature
PNNL	Pacific Northwest National Laboratory
PWR	pressurized water reactor
RCT	ring compression test
RHCF	radial hydride continuity factor (%)
RHT	radial-hydride treatment
RT	room temperature
RXA	recrystallized-annealed
SFWST	Spent Fuel Waste and Science Technology
TIG	tungsten inert gas (welding)
TMT	thermal-mechanical treatment
WEC	Westinghouse Electric Company
Zry-4	Zircaloy-4

UNITS

°C	degree Celsius
cm	centimeter
GWd/MTU	giga-watt-days per metric tonne of uranium
h	hour
K	Kelvin
kN	kilo-newton
m	meter
mm	millimeter
µm	micro meter (micron)
MPa	mega-pascal
N	newton
s	second
wppm	weight parts per million

SYMBOLS

C_H	total hydrogen content in weight parts per million (wppm)
D_{mi}	inner diameter of cladding alloy (mm)
D_{mo}	outer diameter of cladding alloy (mm)
D_o	cladding outer diameter (includes outer-surface oxide layer if present, mm)
d_p	permanent displacement (pre-test minus post-test diameter in loading direction, mm)
d_p/D_{mo}	permanent strain (%)
δ	controlled sample displacement (mm) at the 12 o'clock sample position
δ_e	elastic displacement (mm)
δ_{max}	maximum sample displacement (mm) at the 12 o'clock sample position
Δp	pressure difference across cladding wall ($p_i - p_o$, MPa)
δ_p	corrected offset displacement (mm)
δ_{pt}	traditional offset displacement (mm)
δ_p/D_{mo}	corrected offset strain (%)
δ_{pt}/D_{mo}	traditional offset strain (%)
E	Young's modulus (GPa)
ε_θ	hoop strain calculated using small strain assumption
e_θ	hoop strain calculated from large-strain theory
h_m	cladding alloy wall thickness (mm)
h_{ox}	thickness of outer surface oxide layer (µm)
K_{LC}	calculated loading slope (i.e., loading stiffness) for RCT samples (kN/mm)
K_{LM}	measured linearized loading slope (kN/mm)
K_U	calculated linearized unloading slope (kN/mm)
K_{UM}	measured linearized unloading slope (kN/mm)
L	length of RCT sample (mm)
M_{max}	maximum RCT bending moment (N•m)
ν	Poisson's ratio
P	measured RCT load at the 12 o'clock sample position
P_e	load during elastic displacement (N)
p_i	internal gas pressure (MPa)
P_{max}	maximum RCT load (N)
p_o	external gas pressure
R_{mi}	inner radius of cladding alloy (mm)
R_{mid}	mid-wall radius of cladding alloy (mm)
σ_θ	hoop stress (MPa)
T	temperature (˚C)
T_D	hydrogen dissolution temperature (˚C)
T_P	hydrogen precipitation temperature (˚C)

1. INTRODUCTION

The High Burnup Cask Demonstration Project (Demo Project) is a DOE-Industry effort that addresses the effects of long-term, dry-cask storage and transportation on high-burnup (HBU, >45 gigawatt-days per metric ton uranium [GWd/MTU]) pressurized water reactor (PWR) fuel rods. The overall goal of the program is to assess the integrity of HBU PWR fuel rods under long-term storage and post-storage transportation. In November 2017, thirty-two PWR fuel assemblies, which were irradiated in Dominion's North Anna Power Station to HBU, were loaded into an instrumented cask, dried, and transferred to the storage pad. In addition to collecting valuable thermal and gas sampling data during drying, transfer, and early storage, the cask will be stored for about ten years, during which time it will be transported to a DOE facility for post-storage/transport inspection, characterization, and possible testing.

In support of the Demo Project, 25 fuel rods irradiated to HBU in the same power station were sent to Oak Ridge National Laboratory (ORNL) for nondestructive examination (NDE). The rods are referred to as sibling pins (previously called sister rods) because they have similar designs and irradiation histories as the stored fuel rods with many of the rods extracted from fuel assemblies loaded into the Demo Cask. A full description of these 25 fuel rods, along with NDE results, is presented in Ref. 1. Destructive examinations (DEs) are being performed at ORNL, Pacific Northwest National Laboratory (PNNL), and Argonne National Laboratory (ANL) in accordance with the Phase 1 Test Plan [2]. This plan calls for characterization and mechanical-properties determination of fuel-rod cladding in the as-irradiated condition and following heat treatment at 400°C and cooling at ≤5°C/h. The 400°C heat-treatment temperature is consistent with the peak cladding temperature (PCT) limit of 400°C recommended by the Nuclear Regulatory Commission (NRC) [3]. ORNL [4] and PNNL [5] have already performed preliminary DEs, including rod internal pressure (RIP) measurements for 18 fuel rods. PNNL has received 10 of the 25 fuel rods and ANL is scheduled to receive about 1.4 m of defueled cladding from ORNL and PNNL, as well as PNNL cladding ring compression test (RCT) samples. The defueled cladding samples from ORNL and PNNL will be characterized and subjected to RCTs to determine ductility as a function of test temperature. Maintaining ductility is desirable for all phases of drying, transfer, storage and transport, especially post-storage transport.

In May 2019, ORNL shipped to ANL 12 defueled cladding segments (1.1 m), each 90-mm long, from fuel rods clad in M5®, ZIRLO®, low-tin (LT) Zircaloy-4 (Zry-4), and standard Zry-4. Six of these segments were in the as-irradiated condition and six were from three fuel rods subjected to full-length heat treatment (FHT): heat pressurized rod to 400°C, hold at 400°C for 8 hours, and cool at ≤5°C/h. One purpose of the FHT is to determine if radial hydrides precipitate during cooling and if they have any detrimental effect on cladding mechanical properties, particularly ductility. The uniform peak cladding temperature (PCT) of 400°C bounds internal rod pressures and cladding hoop stresses for fuel rods subjected to drying, transfer, and storage during normal operation. The 12 cladding segments are described in Section 2. Preliminary DE results for two of the M5® segments are given in Section 5. Future ANL work will include characterization, RCTs, and post-RCT characterization of the 12 ORNL cladding segments, as well as cladding segments (0.3-m) to be received from PNNL.

Section 2 describes the ANL protocol for heat-treating rodlets at various PCTs and peak hoop stresses followed by cooling at 5°C/h. This process is called radial hydride treatment (RHT). The section includes lessons learned from finite element analysis (FEA) calculations regarding how far from the weld or Swagelok fitting that RCT samples should be sectioned to avoid the stress discontinuity region due to weld or Swagelok restraint on radial displacement of ends of the samples. It also includes methods for determining ductility from RCT load-displacement curves, as well as the embrittlement criteria.

Details of the FEA calculations are presented in Section 3. Calculations include: (a) elastic stress discontinuity zone for a pressurized tube with welded ends; (b) hoop stress and strain distributions for RCT displacements in the elastic regime; and (c) hoop stress and strain distributions for RCT displacements in the elastic-plastic regime prior to, and after, load removal. The calculations are performed for as-fabricated (AF) 17×17 M5® benchmark-test rings displaced to 0.7 mm and 1.7 mm. M5® is a recrystallized-annealed (RXA) alloy.

The high sensitivity of the ductility transition temperature (DTT) of ZIRLO® cladding to peak RHT hoop stresses has been documented [6,7]. For peak RHT hoop stresses in the range of 87−89 MPa, the DTT was <30°C. For RHT hoop stresses in the range of 93−96 MPa, the DTT was 125−140°C. However, the samples used to fabricate the rodlets differed in hydrogen content and dimensions. Also, there were differences in PCT (400°C and 350°C), number of thermal cycles (1 to 3), and minimum temperature for controlled cooling (130°C vs. 200°C).

Two of the ZIRLO® rodlets (note: these are from fuel rods irradiated for four cycles to 66 GWd/MTU in the North Anna Power Station with very different power histories than experienced by the sibling pins) had the same RHT PCT (350°C), number of thermal cycles (1), and minimum controlled cooling temperature (130°C). They were only 160-mm apart in the parent fuel rod and had similar hydrogen contents and cladding dimensions. The only significant difference was peak RHT hoop stress: 87 MPa for rodlet 646D and 96 MPa for 646B. RCT ductility data and RHCF were presented in Ref. 7 for these two rodlets with the caveat that the high ductility at 170°C for the 646B sample closest to the top end fixture needed confirmation. The concern was that the ring may have been in the stress discontinuity zone (i.e., too close to the top insert and weld) such that the wall-averaged hoop stress might be <96 MPa for part of the ring. Results of FEA calculations and metallographic examination are presented in Section 4 to confirm the validity of the data for the top-most ring, as well as to invalidate the data for the bottom-most ring. The DTT data for these two rodlets are very important in establishing rod internal pressures and drying conditions that may lead to embrittlement at temperatures greater than room temperature (RT). Cladding integrity depends both on cladding ductility and on transportation loads during normal conditions of transport (NCT) and accident conditions. If cladding stresses induced by transport loads are well below the nominal yield stress of the cladding, then ductility is not required for cladding integrity.

2. HBU-FUEL CLADDING MATERIALS AND TEST METHODS

2.1 HBU-FUEL CLADDING MATERIALS

The first two ZIRLO® rodlets in Table 1 were heat treated at 350°C using ANL's standard RHT protocol (see Section 2.2). Rodlet internal pressure for these cases are reasonable values for ZIRLO®-clad fuel rods (5.6 MPa) irradiated to above the licensing limit (62 GWd/MTU) and for Integral Fuel Burnable Absorber (IFBA) fuel rods (6.1 MPa) irradiated to within the licensing limit. The next six cladding segments are from sibling pins that were heat treated by ORNL using the FHT protocol [4] prior to puncturing for rod internal pressure (RIP) measurements, sectioning, defueling and shipment to ANL. The ORNL segment ID number can be determined by combining the fuel rod number with the axial distances from the bottom of the fuel rod (e.g., ANL segment 654A is equivalent to ORNL ID 30AE14 2694 2784). For items listed in bold black, new data are presented in Section 4 for 646B and new data are given in Section 5 for sibling pin segments 654B (following FHT) and 653B (as-irradiated). Additional characterization results are presented in subsequent sections. TBD is to be determined and σ_θ is the wall-averaged hoop stress at the PCT.

Table 1 HBU-fuel cladding materials used in studies of cladding ductility for as-irradiated cladding and for irradiated cladding following simulated drying and storage RHT at PCT.

Cladding Alloy	Burnup, GWd/MTU	ANL ID	Fuel Rod ID	Axial Span, mm	RIP at 25°C, MPa	PCT, °C	σ_θ(PCT), MPa
ZIRLO®	**66**	**646B**	**AM2-F01**	**2430–2510**	**6.1**	**350**	**96**
ZIRLO®	66	646D	AM2-F01	2590–2670	5.6	350	87
M5®	54	654A	30A-E14	2694–2784	3.2	350	52
M5®	**54**	**654B**	**30A-E14**	**3309–3399**	**3.2**	**400**	**52**
ZIRLO®	54	656A	3F9-N05	2572–2662	4.0	400	TBD
ZIRLO®	54	656B	3F9-N05	3241–3331	4.0	400	TBD
Zry-4	60	658A	F35-P17	2555–2645	4.7	400	TBD
Zry-4	60	658B	F35-P17	3069–3159	4.7	400	TBD
M5®	54	653A	30A-D05	2429–2519	3.5	---	---
M5®	**54**	**653B**	**30A-D05**	**3259–3349**	**3.5**	**---**	**---**
ZIRLO®	54	655A	3D8-E14	2213–2303	4.2	---	---
ZIRLO®	54	655B	3D8-E14	2565–2655	4.2	---	---
LT-Zry-4	51	657A	3A1-F05	2555–2645	3.7	---	---
LT-Zry-4	51	657B	3A1-F05	3015–3105	3.7	---	---

The 12 ORNL segments were unloaded from shielding containers and aluminum-alloy shipping tubes in ANL's Irradiated Materials Laboratory Hot Cell 3. The shipping tubes were sealed with a screw-on cap at one end. Most of the shipping tubes were dented, apparently from tight gripping with one ORNL manipulator while the other manipulator was use to screw on the cap. The Cell 3 manipulators could not apply enough torque to remove most of the screw-on caps. Two of the shipping tubes containing M5® segments 654B and 653B were moved to a glove box in DL-114 for retrieval of the cladding segments, visual examination, and metallographic examination. Photographs of these two segments are shown in Fig. 1. Each segment has a mark near the left end indicating the top of the segment relative to the orientation of the fuel rod. The appearance (ignoring color differences) of these two segments is consistent with NDE results [1]. Figure 2 shows quite a different appearance of ZIRLO® segment 656B

following FHT of fuel rod 3F9-N05. The dark spots indicate possible regions of oxide spallation. The photograph was taken through the liquid zinc-bromide shield window of the hot cell, which accounts for the poor contrast-focus and the red-yellow hue. However, the indicated regions of oxide spallation are consistent with NDE results [1] generated prior to the shipment. A better focus-contrast image will be taken after the segment is moved to a glove box for imaging, sectioning, and metallographic examination. The remaining 10 sibling-pin segments were retrieved from ORNL shipping tubes in Hot Cell 3 after new equipment (e.g., vise, tube cutter, etc.) was moved into the cell. They were examined visually, inserted into segment-ID-marked ANL storage tubes, and are currently stored in Hot Cell 4. The visual examination did not reveal any damage to cladding segments from the denting of the shipping tubes.

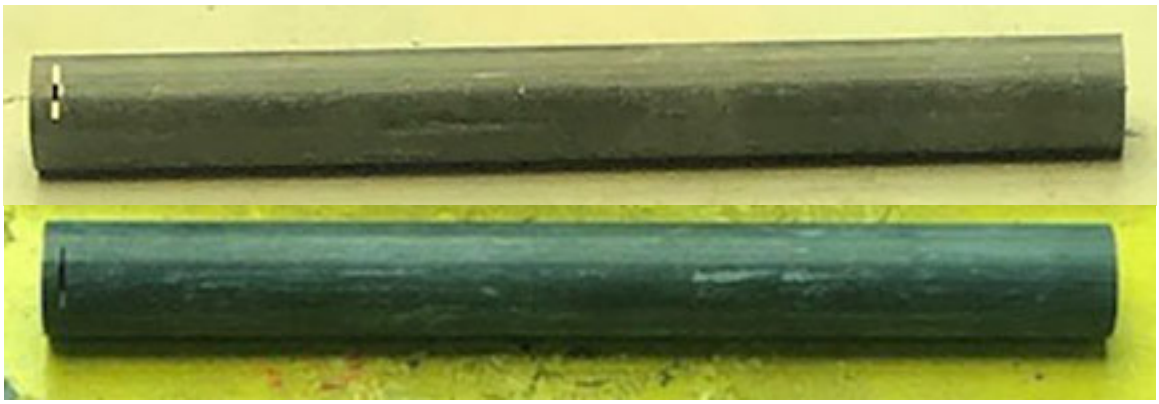

Figure 1: Physical appearance of M5® cladding segments 654B (top) and 653B (bottom).

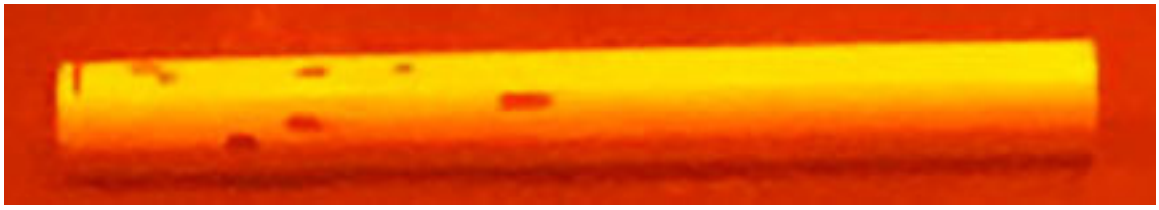

Figure 2: Physical appearance of ZIRLO® cladding segment 656B.

2.2 TEST METHODS

The ANL protocol for single-cycle heating-cooling tests consists of: (a) simulated drying and storage testing during which a sealed, pressurized rodlet is heated to, and stabilized at, the PCT within 1 h, held at the PCT for 1 h, cooled at 5°C/h to 130°C, and cooled at a higher-then-slower rate to RT and (b) ring-compression testing at three to four temperatures from RT to 200°C and at 5 mm/s (reference value) displacement rate to a maximum sample displacement (δ_{max}) of 1.7 mm. The temperature history for rodlet 646B is shown in Fig. 3. The same heating and cooling rates were used for rodlet 646D, but the hold times were different: 1 h for 646B and 24 h for 646D.

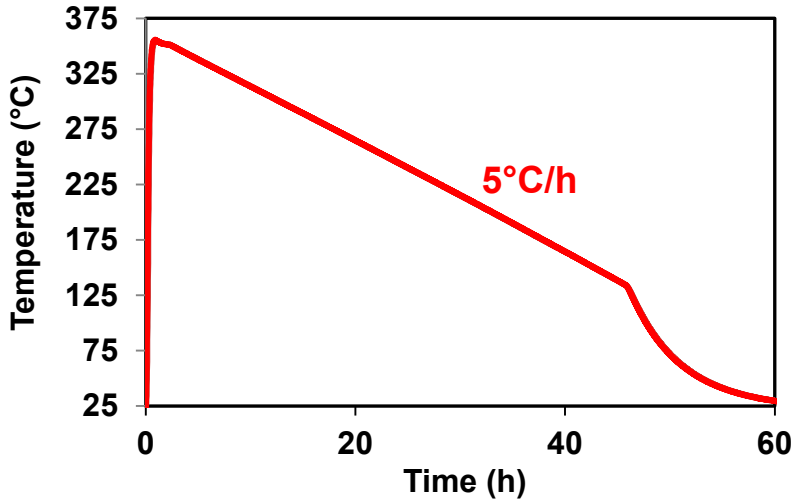

Figure 3: Rodlet 646B temperature history for controlled cooling from 350°C to 130°C.

HBU-fuel cladding segments were used to fabricate the sealed and pressurized (with argon) rodlets. Following outer- and inner-surface oxide removal at the ends of the samples, as well as squaring of the ends, the components to be assembled are shown in Fig. 4. From left to right, these components include the solid bottom end fixture with a 15-mm insert (Zircadyne-702), the 25-mm-long zirconia pellet used to reduce gas volume and stored energy, the HBU-fuel cladding segment, and the hollow top end fixture with a 15-mm insert (Zircadyne-702) and a small hole at the top to allow for pressurization. In general, the fabrication sequence consisted of circumferential welding of the bottom end fixture, loading of the pellet, circumferential welding of the top end fixture, pressurization in a chamber, laser-welding the top end-fixture hole with the rodlet in the chamber, and checking to ensure that the rodlet was indeed sealed and did hold pressure. All rodlets with the exception of 646B were fabricated from the components shown in Fig. 4

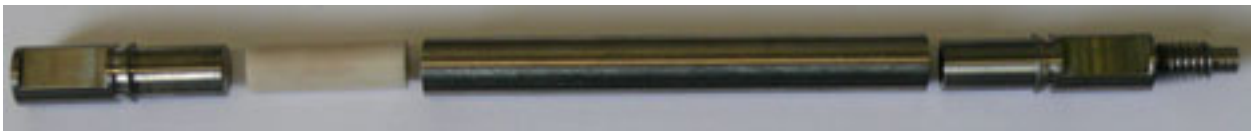

Figure 4: Rodlet bottom end fixture, zirconia pellet, cladding segment, and top end fixture.

Although performing the circumferential weld is the most difficult fabrication step, a successful weld depends on the quality of the oxide removal, especially removal of the inner-surface oxide layer. For the long end caps shown in Fig. 4, inner-surface oxide removal must extend about 15−19 mm from each end of the cladding segment. Inner-surface oxide removal is performed by stationary reamers with the

sample rotating in a mini-lathe. With such a crude setup, it is difficult to remove all the inner-surface oxide within the end span without thinning the cladding wall at the ends. The end caps were re-designed such that the length of the inserts was reduced from 15 mm to 10 mm (see Fig. 5). This reduced the length of the heat-affected zone (HAZ). The main purpose of the insert is to stabilize the position of the end fixture relative to the end of the cladding segment. The primary weld occurs between the flange just above the insert and the cladding wall. The Astro Arc welder used for circumferential welding has a thin (1-mm in diameter) electrode that revolves around the joint to be welded. Welding is conducted in an argon chamber and the process is essentially tungsten-inert-gas (TIG) welding.

Figure 5: Rodlet bottom end fixture (redesigned), cladding segment, and top end fixture (redesigned).

Prior to rodlet pressurization, the outer diameter (D_o) is measured for each cladding segment at two orientations (90° apart) and at three axial locations. These values are averaged to give D_o for the rodlet. The thickness of the outer-surface oxide layer (h_{ox}) is estimated from data for similar rods or from interpolation or extrapolation of data from the same fuel rod at different axial locations. The same approach is used to estimate the cladding-alloy wall thickness (h_m). The outer diameter of the cladding alloy (D_{mo}) is calculated from $D_o - 2\ h_{ox}$, and the cladding alloy inner diameter (D_{mi}) is simply $D_{mo} - 2\ h_m$. The ratio R_{mi}/h_m, where R_{mi} is the cladding alloy inner radius ($D_{mi}/2$), is used in Eq. 1 to calculate the average hoop stress (σ_θ) from the pressure difference ($\Delta p = p_i - p_o$) across the cladding wall, where p_i and p_o (0.1 MPa during fabrication at 23°C and 0.17 MPa in the RHT furnace) are internal and external pressures, respectively.

$$\sigma_\theta = (R_{mi}/h_m)\ \Delta p - p_o \qquad (1)$$

The ideal gas law is used to relate p_i at the PCT to p_i at 23°C: $p_i(\text{PCT}) = ([\text{PCT} + 273\text{K}]/296\text{K})\ p_i(23°\text{C})$. Given the target σ_θ at the PCT, the fabrication pressure at 23°C is calculated using Eq. 1.

Equation 1 is valid for both thick- and thin-wall pressurized tubes. In many reports, papers, and textbooks, R_{mi} is replaced by the mid-wall radius ($R_{mid} = [D_{mo} - h_m]/2$) for thin-wall tubes. For as-fabricated 17×17 cladding with 9.50-mm D_{mo} and 0.57-mm h_m, this approximation leads to a 7% overestimation of the average cladding hoop stress for $p_o << p_i$.

Following RHT, the rodlet is depressurized and sectioned for C_H samples, RCT samples, and metallographic examination samples, from which precise values of the geometrical parameters in Eq. 1 are determined. Using this procedure, the calculated target peak rodlet σ_θ has been found to be within ±3 MPa of the actual value. Actual values are reported for each rodlet.

The second phase of the test protocol consists of RCTs. Figure 6 shows a schematic of RCT. The displacement (δ) is controlled by controlling the displacement rate and the load (P) is measured. The loading induces maximum hoop bending stresses (σ_θ) at the inner surfaces of the 12 (under load) and 6 (above support) o'clock positions. Tensile hoop stresses also occur at the 3 and 9 o'clock outer surfaces. Associated with these tensile stresses are tensile strains (ε_θ). Within the elastic range, hoop stresses at 3 and 9 o'clock are about 40% less than hoop stresses at 12 and 6 o'clock. Also, because the length (L ≈ 8 mm) of the rings is much greater than the cladding wall thickness (0.54 to 0.57 mm for HBU-fuel ZIRLO® and M5®), an axial stress is induced that is up to 0.37 times the hoop stress within the elastic deformation regime. The maximum sample displacement (δ_{max} = 1.7 mm) is chosen to give ≈10% This maximum displacement gives an "S" shaped curve with a "lower-shelf" plastic strain <2% and an "upper-shelf" plastic strain of about 10% from which the DTT can be determined. The reference displacement rate is 5 mm/s. A repeat test with an adjacent sample may be conducted at 0.05 mm/s to allow real-time viewing of the evolution of the load-displacement curve and stopping of the test at the first significant load drop.

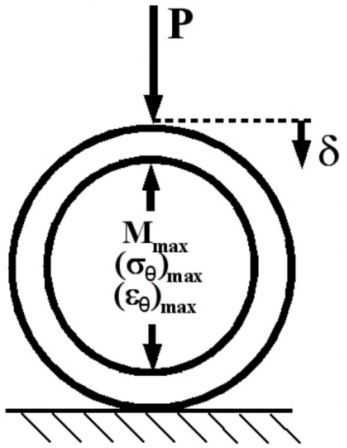

Figure 6: RCT measured load (P) and controlled displacement (δ).

Load-displacement curves and post-test diameter measurements are used to determine offset (δ_p) and permanent (d_p) displacements, respectively. These are normalized to D_{mo} to give relative plastic displacement (i.e., plastic strain) for the ring structure. Permanent displacement is defined as the difference between pre- and post-test diameter measurements along the loading direction. Figures 7 and 8 show how traditional (δ_{pt}) and corrected (δ_p) offset displacements are determined from benchmark load-displacement curves for as-fabricated (AF) 17×17 M5® rings subjected to displacements of 1.7-mm (Fig. 7) and 0.5-mm (Fig. 8). For the benchmark samples, D_{mo} = 9.49 mm in the loading direction, h_m = 0.57 mm, and L = 8.06 mm. The traditional offset-displacement methodology calls for unloading the sample at the same slope as the measured linearized loading slope (K_{LM}). It should be noted that K_{LM} is less than the calculated ring stiffness (K_{LC}) due to the influence of machine compliance. For the case shown in Fig. 7, this approach gives δ_{pt} = 1.24 mm, which is greater than the more accurate d_p = 1.10 mm. Thus, there is an inherent error in the traditional approach as the measured linearized unloading slope (K_{UM}) is always less than K_{LM}. K_{UM} is determined from the slope of the line connecting δ_{max} to the displacement axis value based on the measured value of d_p at zero load. Normalizing these displacements to D_{mo} gives 13% traditional offset strain and 11.6% permanent strain, which is also the corrected offset strain (δ_p/D_{mo}) for these benchmark tests. For Fig. 7, K_{UM}/K_{LM} is 0.771.

As the total and traditional-offset displacements decrease, the difference between δ_{pt} and d_p decreases. This is shown in Fig. 8 for which δ_{pt} is 0.11 mm, d_p is 0.09 mm, and K_{UM}/K_{LM} is 0.944.

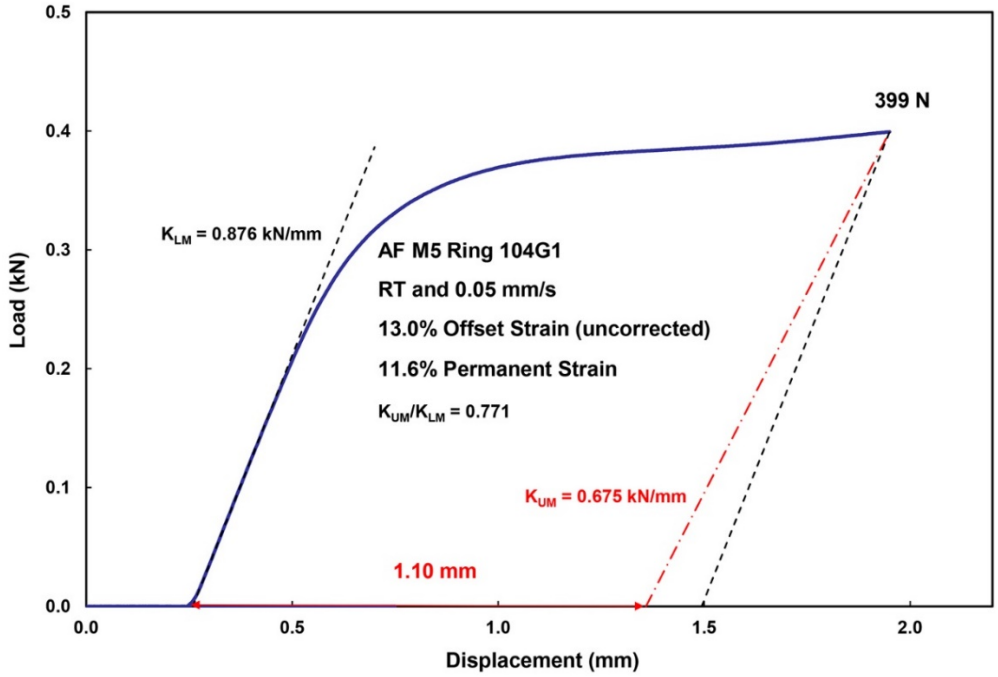

Figure 7: Load-displacement curve for AF M5® ring tested at RT and 0.05 mm/s to 1.7-mm ring displacement.

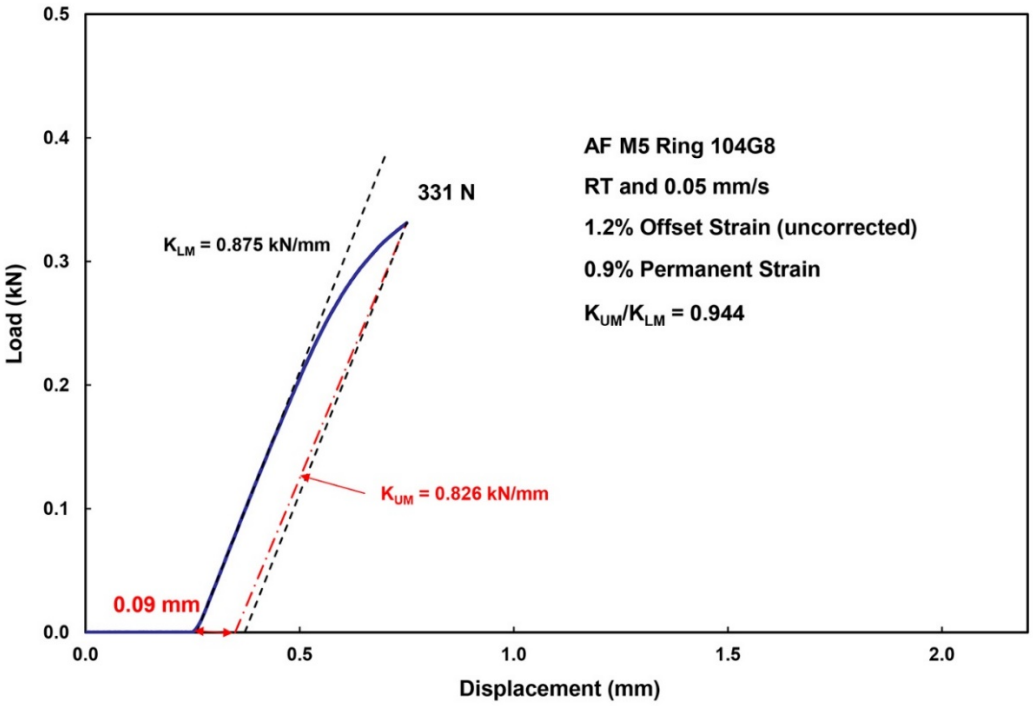

Figure 8: Load-displacement curve for AF M5® ring tested at RT and 0.05 mm/s to 0.5-mm ring displacement.

Energy methods were used to determine the bending moment as a function of circumferential orientation. Both wide-beam and narrow-beam assumptions were used to relate the bending moment to bending stresses and strains within the elastic-deformation regime, as well as the relationship between the elastic load (P_e) and elastic displacement (δ_e). The curvature of the ring was not taken into account in the bending analysis. The calculated loading stiffness is $K_{LC} = P_e/\delta_e$, where

$$P_e = f(\nu) \{(E\ L)/(1.79)\} (h_m/R_{mid})^3\ \delta_e \quad (2)$$

In Eq. 2, E is Young's modulus (91.9 GPa for RXA alloys at room temperature [8]) and ν is Poisson's ratio (0.37 for RXA and CWSRA alloys at RT to 400°C [9]). For a narrow beam (in terms of the length [L] to h_m ratio), $f(\nu) = 1$. For a wide beam ($L/h_m >> 1$), it is difficult for the material to expand or contract in the length direction and the assumption of plane strain in the axial direction leads to $f(\nu) = 1/(1 - \nu^2) = 1.16$. However, no guidance is given in the literature for determining $f(\nu)$ as a function of L/h_m. FEA calculations were used to determine that $f(\nu) = 1.09$ for L = 8 mm and h_m = 0.57–0.61 mm (L/h_m = 13.1 to 14.0), which is close to half way between the narrow- and wide-beam solutions.

For HBU-fuel cladding rings that crack during the 1.7-mm displacement, d_p cannot be determined accurately. Thus, one must rely on a correlation for the unloading slope to determine the corrected offset displacement prior to the first significant crack, from which the ductility is determined. The correlation developed for this application is based on the results from a large number of benchmark tests with permanent displacements ranging from 0.09 mm to 1.4 mm, displacement rates of 0.03−50 mm/s, and temperatures of 20−150°C. Results of these benchmark tests are shown in Fig. 9 for the ratio of measured unloading/loading (K_{UM}/K_{LM}) slope vs. traditional offset strain (δ_{pt}/D_{mo}). Also shown in Fig. 9 are results from nine RCTs with HBU-fuel M5® (solid red circles) that exhibited no cracking after 1.7-mm total displacement. The blue hollow-circle data points are from RCTs conducted with AF 17×17 M5® (48 points) and AF 17×17 ZIRLO® (6 points) cladding samples. Outer diameters were 9.49±0.1 mm and nominal cladding wall thickness values were 0.61 mm (reference case) and 0.57 mm (6 ZIRLO® data points and 15 M5® data points). The data set includes RCT results from two machines: (a) the screw-type Instron 5556 and (b) the servo-hydraulic Instron 8511. Results are also shown for shorter (6 mm) and longer (10 mm) rings, as well as larger-diameter 15×15 M5® rings.

The correlation for the ratio K_U/K_{LM} as a function of δ_{pt}/D_{mo} (in %) is:

$$K_U/K_{LM} = 1 - 0.0303\ \delta_{pt}/D_{mo} \text{ for } \delta_{pt}/D_{mo} \leq 8.0\% \quad (3a)$$

$$K_U/K_{LM} = 0.758 \text{ for } \delta_{pt}/D_{mo} > 8.0\% \quad (3b)$$

The stiffness ratio for HBU-fuel M5® with >8% traditional offset strain is 0.746, which is in good agreement with the 0.758 determined for AF cladding materials.

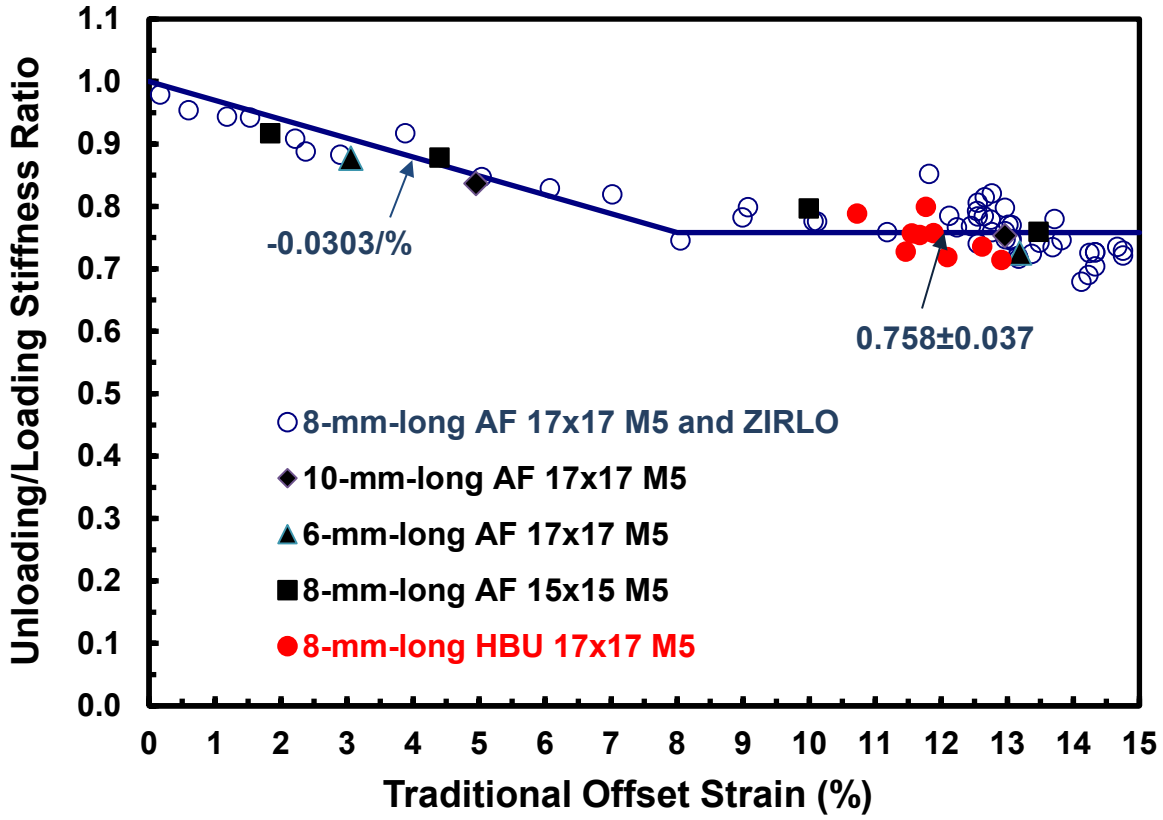

Figure 9: RCT benchmark results for determining the ratio of unloading/loading stiffness as a function of the traditional offset strain.

There is reasonable confidence in using Eqs. 3a and 3b to calculate the corrected offset displacement (δ_p) and corresponding corrected offset strain (δ_p/ D_{mo}) for cladding rings that do not crack prior to a significant load drop. However, with the possible exception of HBU-fuel M5® with long radial hydrides, sparsely distributed circumferential hydrides, and a thin oxide layer (≈10±3 µm), most HBU-fuel cladding samples exhibited some cracking prior to the maximum displacement or prior to a significant load drop. The effects of minor cracks (e.g., multiple short cracks through the hydride rim) can reduce the unloading slope by as much as 25%. A large number of tests with HBU-fuel cladding would be needed to develop a correlation for unloading slope as a function of number and depth of cracks. Until such tests are performed, uncertainty in the determination of the corrected offset strain is taken into account in the formulation of the embrittlement criterion. A set of criteria is described in the following.

Two of the criteria for determining embrittlement remain unchanged for cladding with radial and circumferential hydrides: δ_p/D_{mo} <2% prior to >25% load drop or >50% decrease in re-loading slope. In previous work [10–11], it was established that >25% load drop or >50% decrease in re-loading slope corresponded to a crack or cracks extending through >50% of the wall thickness. A third criterion was added within the past two years for load-displacement curves that indicated major cracking could occur within the transition from elastic to elastic-plastic displacement without exhibiting either a 25% load drop or a 50% decrease in elastic re-loading slope, for which an "implied" load drop >25% is used. Although such cases are relatively infrequent, the implied load drop criterion can result in a significant decrease in ductility. The implied load drop is illustrated in Figure 10 for a HBU-fuel M5® sample (80±7 wppm) from a rodlet subjected to peak RHT conditions of 350°C/89-MPa, which led to long radial

hydrides (44±18% RHCF). The solid blue load-displacement curve is for the ring tested at 23°C. The dashed-line black curve is for the ring tested at 60°C. The 23°C load-displacement curve shows a series of minor load drops that initiated during elastic loading. The segment of the curve after the first load drop from 310 N to 262 N is too short to determine a reliable re-loading slope. This is followed by two additional small load drops before the load increases smoothly with displacement. If severe cracking is assumed to occur during the first load drop, the sample would have an offset strain of only 0.3% and be considered brittle. If severe cracking were assumed to occur during the second load drop, the sample would appear to have an offset strain >2% and be considered ductile. However, the unloading slope from the peak of the second load drop would be much smaller than predicted by Eq. 3a due to cracking. Figure 11 shows that the sample had a through-wall crack at the 12 o'clock orientation. There was also a long crack at the 6 o'clock orientation. However, the 60°C ring achieved a peak load of 438 N prior to the 39% load drop, which resulted in an offset strain of only 1.6% (brittle). This was followed by a second severe load drop indicating at least two long cracks. It is evident that the 23°C ring was as severely cracked as the 60°C ring because they both had about the same load-carrying capacity beyond 1.2 mm on the displacement axis. This comparison indicates that severe cracking occurred during the first load drop for the 23°C ring even though the observed load drop was only 15%. The implied load drop is >25% and as much as 40% for this case.

The 2% offset strain limit is based on the uncertainty in the measurement of the permanent displacement (pre-test diameter minus post-test diameter, d_p) for HBU-fuel cladding and the added uncertainty in the permanent displacement measurement for HBU-fuel cladding due to flaking off of the oxide layer under the applied loading plate and above the support plate. Multiple cracks through the oxide layer and the hydride rim lower the unloading stiffness to values less than shown in Fig. 9, which has also been factored into the 2% offset-strain limit. An additional consideration is that the maximum material strain is generally less than the ring structural strain (i.e., permanent and corrected-offset displacements normalized to the cladding outer diameter). The peak elastic strain in the material is about 0.3 times the structural strain. As shown in Section 3, FEA calculations for the maximum plastic material hoop strain give 9.1% plastic strain for the M5® benchmark ring subjected to 1.7-mm displacement. The structural permanent strain for the Fig. 7 load-displacement curve was 11.6%. An apt analogy would be to consider a coiled spring that lengthens due to tensile loading. If the spring is pulled beyond the elastic limit of the coils, there is a permanent increase in length (ΔL) after unloading. From a structure perspective, the permanent strain (i.e., relative displacement) is $\Delta L/L_o$, where L_o is the initial length of the spring prior to application of the load. However, the plastic strain in the coil material is quite different from $\Delta L/L_o$ and is more of a shear strain than a tensile strain.

As the HBU-fuel M5® tested had very thin oxide layers (10±3 μm) and no hydride rim, the 2% offset strain criterion is more conservative for this HBU-fuel alloy than for the HBU-fuel Zry-4 and ZIRLO® samples tested, both of which had thicker oxide layers (30−100 μm), thick hydride rims (30−100 μm), and minor cracks through the oxide layer and the hydride rim during the RCT.

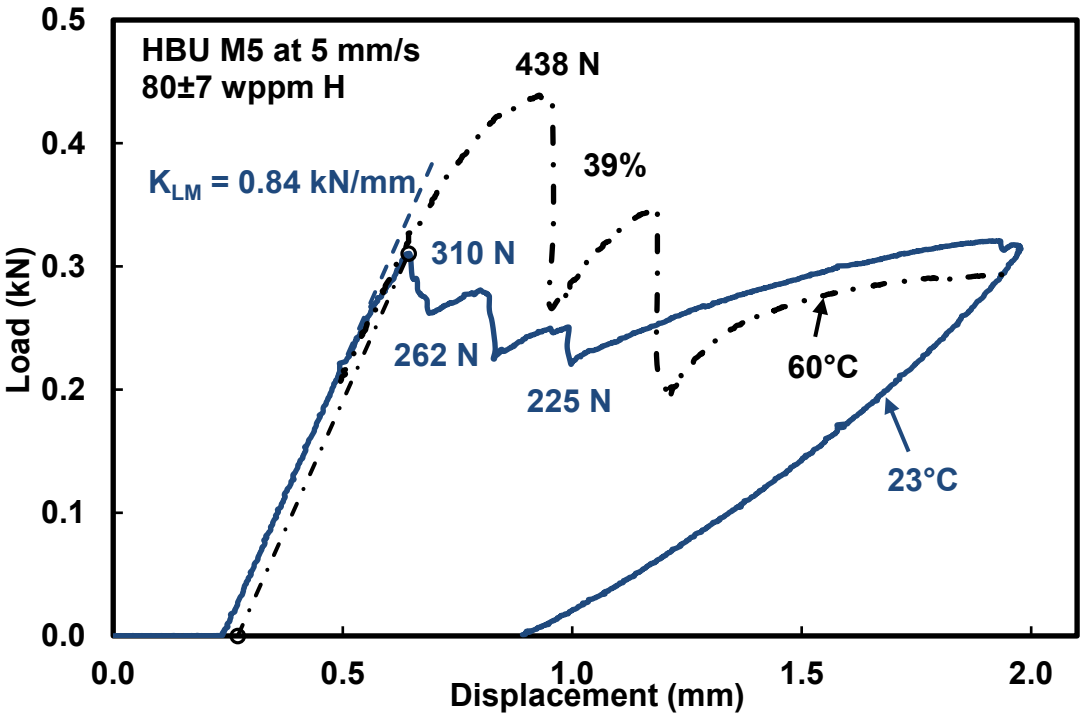

Figure 10: Load-displacement curves for HBU-fuel M5® with 80±7 wppm C_H following RHT at peak conditions of 350°C/89-MPa.

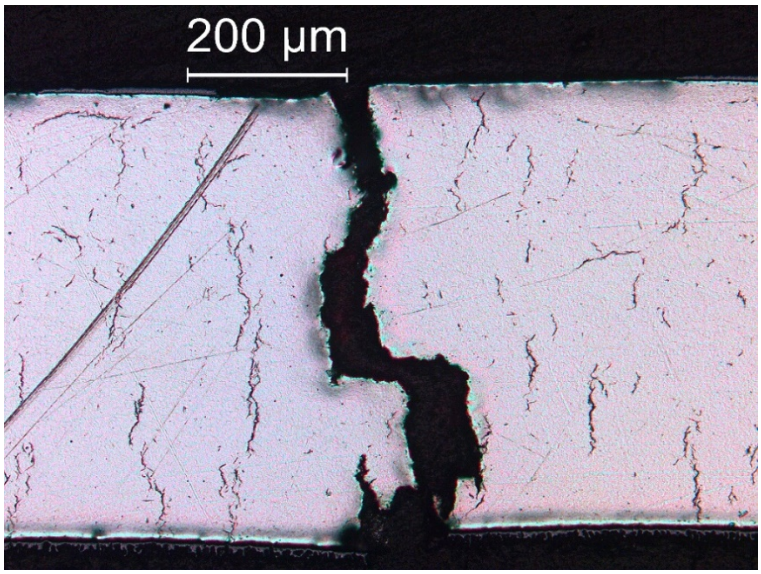

Figure 11: Through-wall crack in HBU-fuel M5® ring tested at 23°C following 350°C/89-MPa RHT.

3. FEA RESULTS FOR RHT AND RCT LOADING

The FEA model was developed using ABAQUS for cladding rings subjected to RHT pressure loading and to RCT hoop-bending loading. The model includes the machine stiffness (>10 kN/mm), elastic properties for RXA AF M5® (i.e., E= 91.9 GPa [8] and ν = 0.37 [9] at RT), large strain capability, and anisotropic plastic stress-strain properties. ABAQUS includes three anisotropy factors for principal stresses and three anisotropy factors for shear stresses. Given that parameters are adjusted to match a single load-displacement curve, there is no unique set of anisotropy factors that can be determined, as multiple combinations of anisotropy factors will result in a good fit with the measured load-displacement curve. In this section, we focus only on the anisotropy factors (ratios of yield stresses) for the hoop, axial, and radial principal yield stresses.

Literature values [12] for the hoop tensile properties of AF M5® were based primarily on results of ring-stretch tests conducted at low and high strain rates (up to 500%/s): 432 MPa hoop yield stress ($\sigma_{\theta Y}$) and 516 MPa hoop ultimate tensile stress ($\sigma_{\theta UTS}$), both at RT (22°C). Based on unpublished ANL data, the axial tensile properties measured at RT and 0.1%/s strain rate were: 400 MPa for σ_{zY} and 530 MPa for σ_{zUTS}. Although the strain-rate dependence of these properties should be relatively low, it is surprising that the literature values are treated as strain-rate independent. Use of these properties in the FEA model resulted in an under-prediction of load in the elastic-plastic displacement regime. Thus, yield stresses were modified for each ABAQUS run until good agreement was obtained between calculated and measured RCT load-displacement. In previous work [7], the best fit was obtained with 540 MPa for $\sigma_{\theta Y}$, 513 MPa for σ_{zY}, and 567 MPa for σ_{rY} (not measured). In the current work, more reasonable values of the hoop and axial yield stress values were used in combination with an elevated value of the radial yield stress: 440 MPa for $\sigma_{\theta Y}$, 400 MPa for σ_{zY}, and 638 MPa for σ_{rY}.

3.1 FEA RESULTS FOR RCT LOADING

Three cases were modeled: (a) elastic displacement of an 8-mm-long M5® ring to 0.16 mm outer surface displacement, (b) elastic-plastic M5® benchmark test with 0.7-mm displacement, and (c) elastic-plastic M5® benchmark test with 1.7-mm displacement. For the 0.16-mm elastic displacement case, nominal outer diameter (9.50 mm), wall thickness (0.57 mm), and length (8.00 mm) were assumed. For the two M5® benchmark cases, measured values for outer diameter (9.495 mm) and wall thickness (0.57 mm) were used as input parameters. The lengths of the two benchmark samples varied slightly: 8.05 mm for the 0.7-mm test and 8.07 mm for the 1.7-mm test. The FEA model for the two benchmark tests includes the effects of machine stiffness (see Fig. 12), while the 0.16-mm elastic case does not. As shown in Fig. 12, RCT loading is modeled by two rigid plates, one supplying the load (top) and the other acting as the support (bottom). The top plate is attached to a spring representing the machine stiffness. The coefficient of friction between the ring and the load/support plates was set to 0.1 for the purpose of stabilizing the FEA calculations. Sensitivity studies indicated that results were not very sensitive to the value of friction coefficient in the low range. Initially, there is loading only along the top outer diameter line. As displacement of the top plate increases, the contact area increases causing the line load to transition to a distributed area load.

Elastic Solution for Ring Displacement of 0.16 mm

The purpose of running this case using the FEA model is to determine the accuracy of the closed form solution used to derive the load-displacement stiffness given in Eq. 2. The closed form solution was derived with the assumptions of line loading, thin-straight wall, and wide beam. Closed-form predictions for maximum tensile hoop stress ($\sigma_{\theta max}$) and hoop strain ($\epsilon_{\theta max}$) are 521 MPa and 4.90×10^{-3}, respectively.

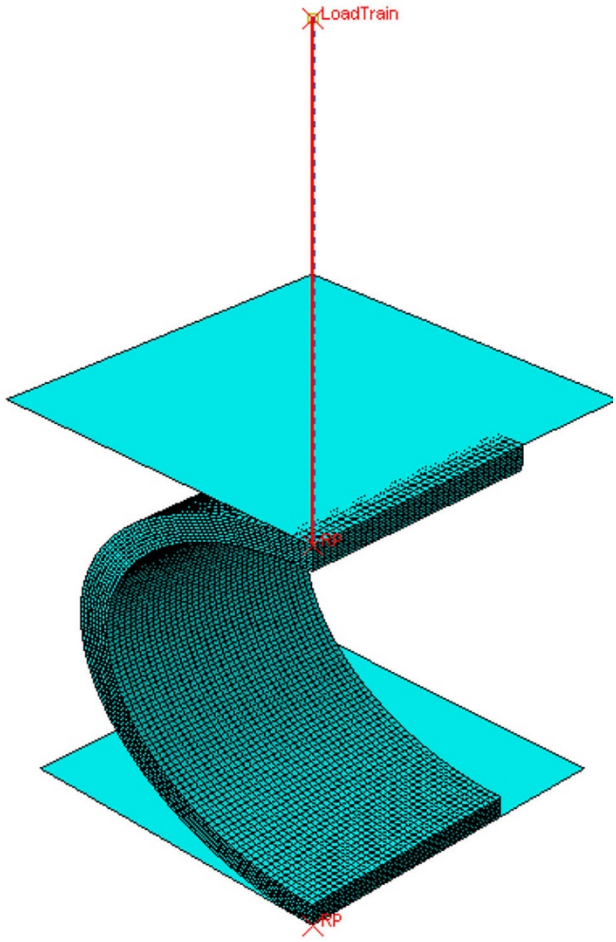

Figure 12: FEA model for RCT loading in benchmark tests.

Figures 13 and 14 show the FEA-predicted hoop stress and hoop strain contours, respectively, for the 0.16-mm displacement case. The highest values of tensile hoop stress and strain are concentrated at the inner surfaces below the loading plate (12 o'clock) and above the support plate (6 o'clock). The FEA-calculated values for maximum tensile hoop stress (535.8 MPa) and large strain ($e_\theta = 5.03\times10^{-3}$) are close to the values predicted using the closed form solution. The relationship between large strain (e_θ) and small (i.e., engineering strain) is given by $e_\theta = \ln(1 + \epsilon_\theta)$. For comparison with the closed form solution the FEA-predicted small strain would be 5.04×10^{-3}. Thus, the FEA-predicted maximum hoop stress and strain are only a factor 1.03 higher than the closed-form-solution predicted hoop stress and strain. It should be noted that FEA does not calculate stresses and strains exactly at the inner surface. These are determined by interpolations/extrapolations from mesh calculations, which means that results are dependent on mesh size. A mesh size that is not fine enough for concentrated stresses and strains can result in a "hot spot" at which the stress is over-predicted. This does not appear to be the case here. An additional calculation was performed with a finer mesh and the peak hoop stress decreased to only 535.2 MPa.

The structure strain for the 0.16-mm displacement case is 0.16-mm/9.50-mm = 0.0168 (1.68%), which is a factor of 3.33 higher than the material strain.

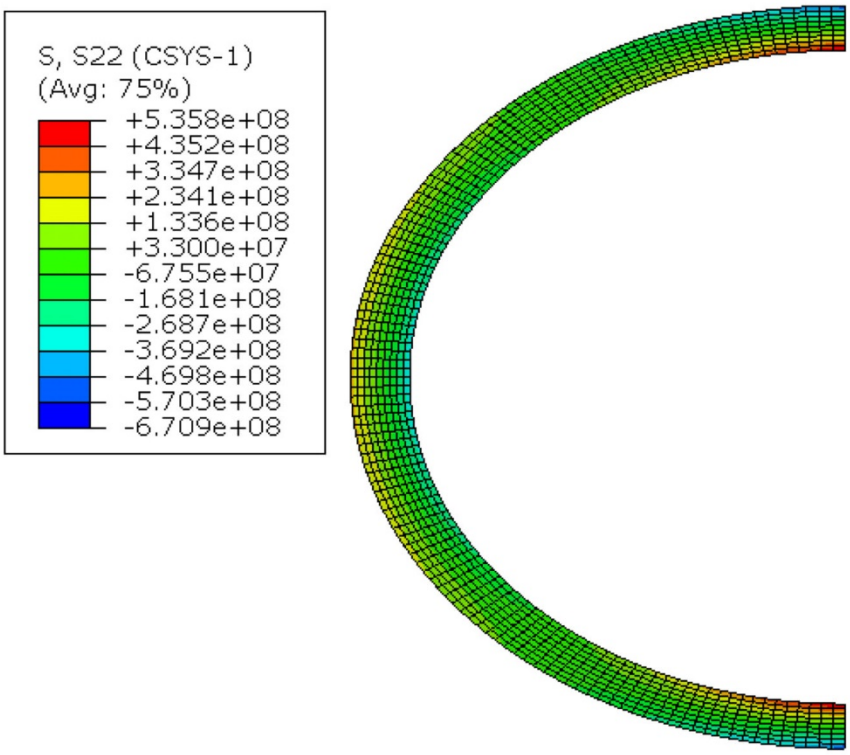

Figure 13: FEA-predicted hoop stress for 0.16-mm elastic displacement.

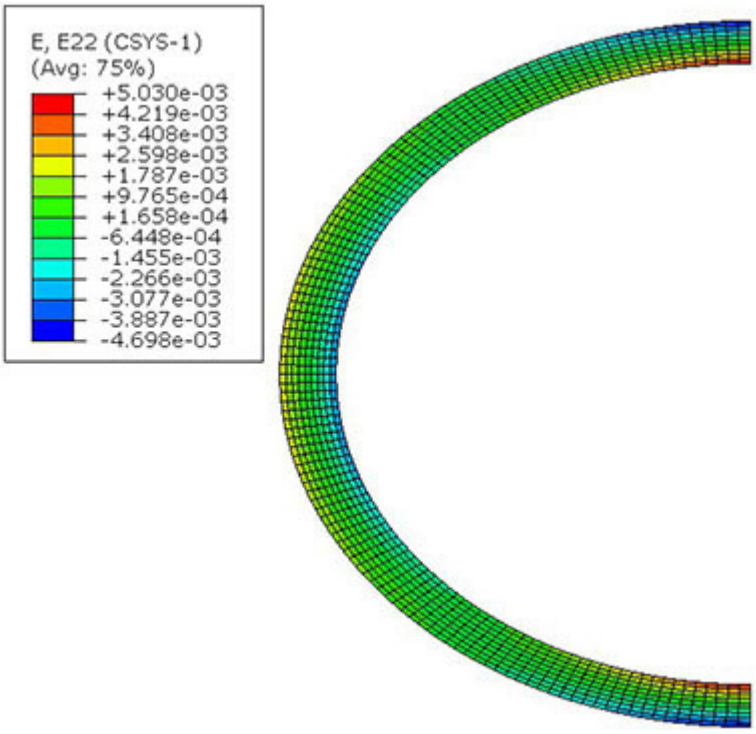

Figure 14: FEA-predicted hoop strain for 0.16-mm elastic displacement.

Elastic-Plastic Solution for the 0.7-mm Benchmark Test

Figure 15 shows the load-displacement curve for the 0.7-mm displacement benchmark test with AF M5® cladding. The permanent structure strain was 2.3%. Figure 16 shows the agreement between the FEA-predicted load-displacement curve and the measured one with hoop, axial and radial yield stress values of 440 MPa, 400 MPa, and 638 MPa, respectively.

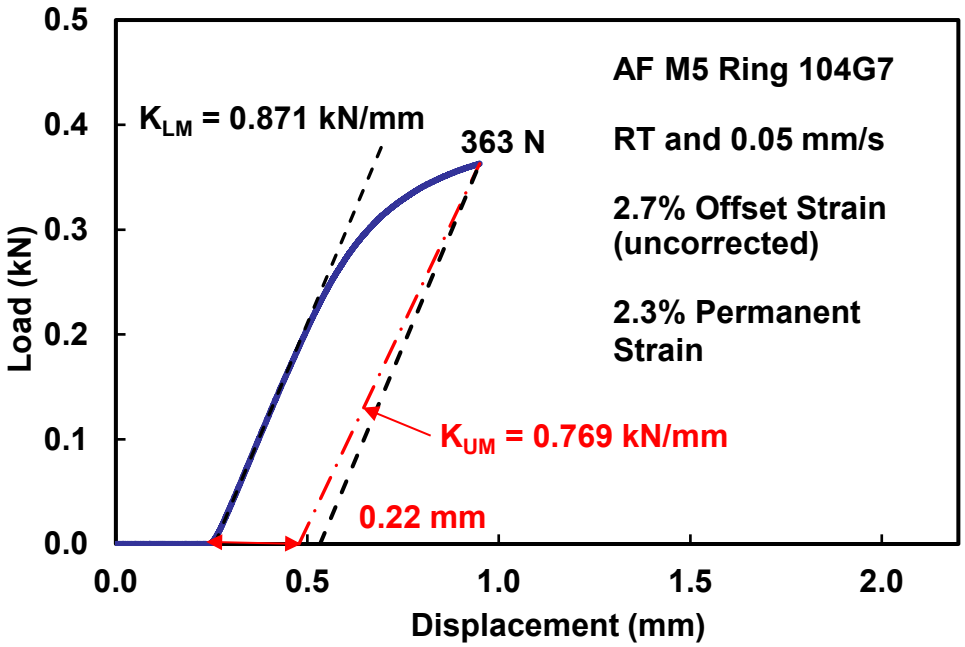

Figure 15: Load-displacement curve for AF 17×17 M5® ring displaced to 0.7 mm at RT and 0.05 mm/s.

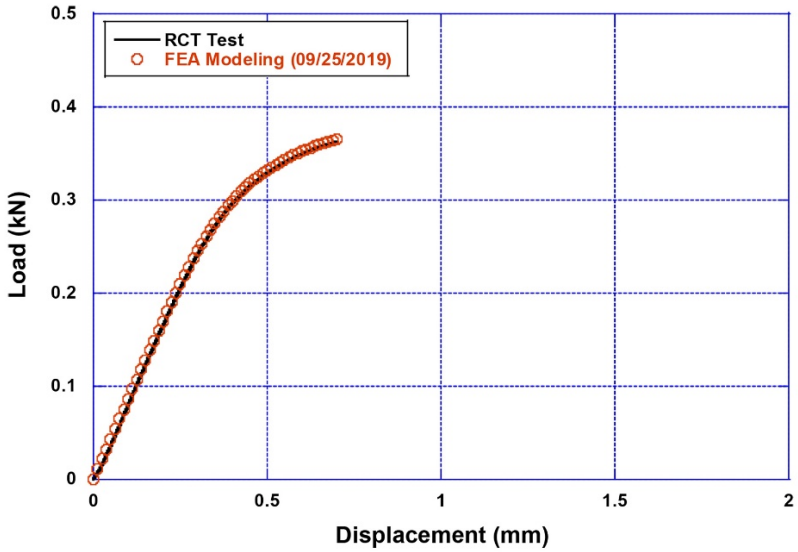

Figure 16: FEA-predicted and measured load-displacement curves for the 0.7-mm benchmark test.

FEA calculations were performed for stresses and strains prior to and after unloading. Figures 17 and 18 show the FEA hoop-stress predictions prior to unloading and following unloading, respectively. Prior to unloading, the peak tensile hoop stress was 760.2 MPa. After unloading, the peak residual tensile hoop stress was 436.5 MPa. The presence of residual stresses is due to elastic contraction with localized, non-uniform regions of plastic deformation.

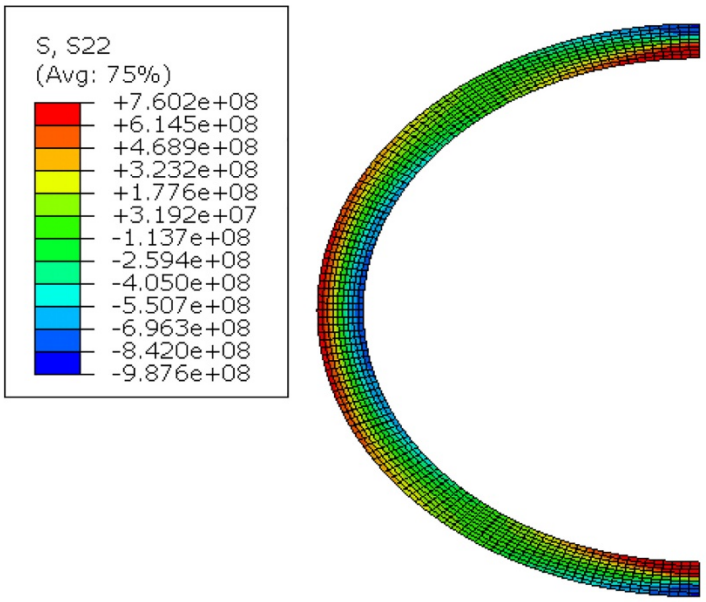

Figure 17: FEA-predicted hoop stress distribution at 0.7-mm displacement.

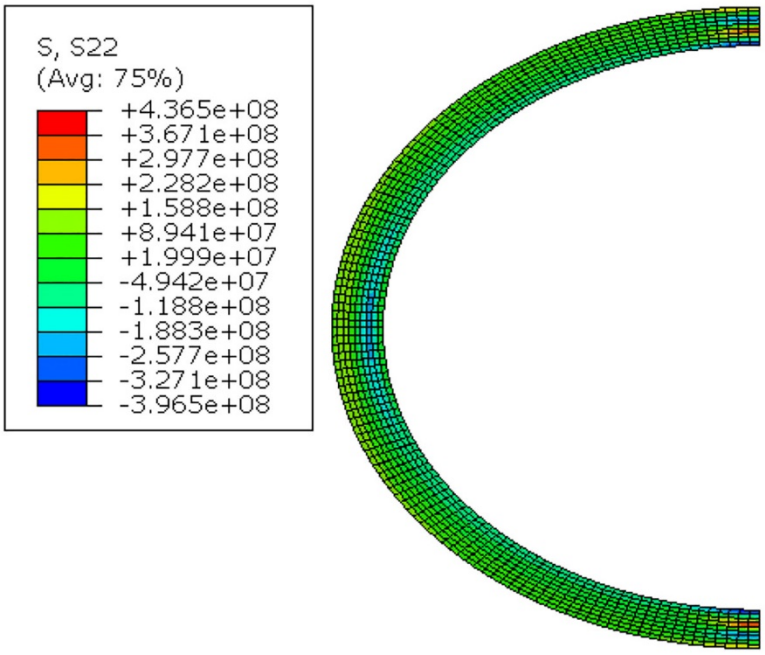

Figure 18: FEA-predicted residual hoop stress after unloading from 0.7-mm displacement.

Figure 19 shows the predicted plastic hoop strain at 0.7-mm displacement. The maximum value of 0.0299 (3.04% engineering strain) occurs at the inner surface below the load and above the support. As expected, Figure 20 shows very little change in maximum plastic hoop strain after unloading (0.02916, 2.96% engineering strain). For this displacement, the maximum plastic hoop strain (2.96%) is slightly higher than the permanent structural strain (2.3%).

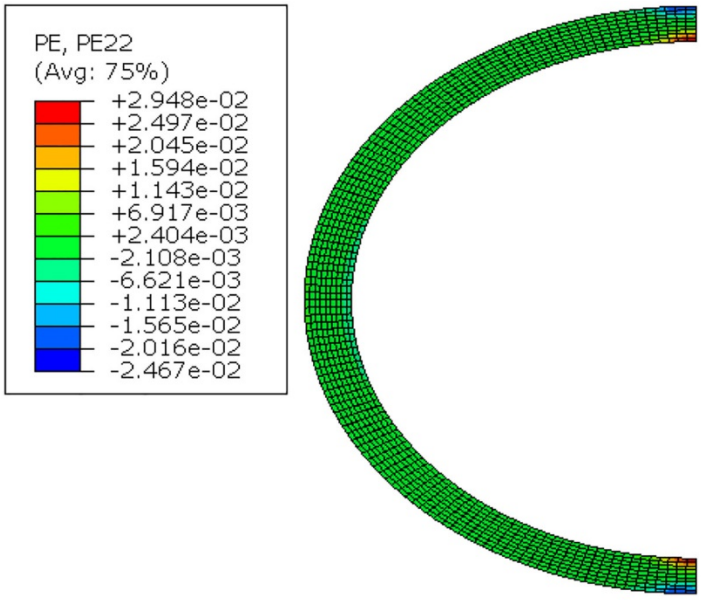

Figure 19: FEA-predicted plastic hoop strain at 0.7-mm displacement.

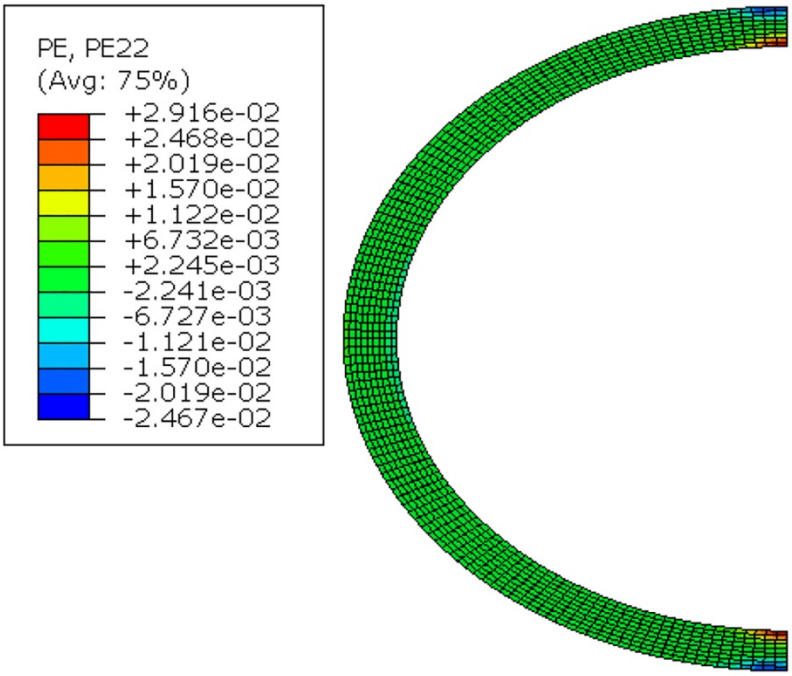

Figure 20: FEA-predicted plastic hoop strain after unloading from 0.7-mm displacement.

Elastic-Plastic Solution for the 1.7-mm Benchmark Test

Figure 21 (same as Fig. 7) shows the load-displacement curve for the 1.7-mm displacement benchmark test with AF M5® cladding. The permanent structure strain was 11.6%. Figure 22 shows the agreement between the FEA-predicted load-displacement curve and the measured one with hoop, axial and radial yield strength values of 440 MPa, 400 MPa, and 638 MPa, respectively.

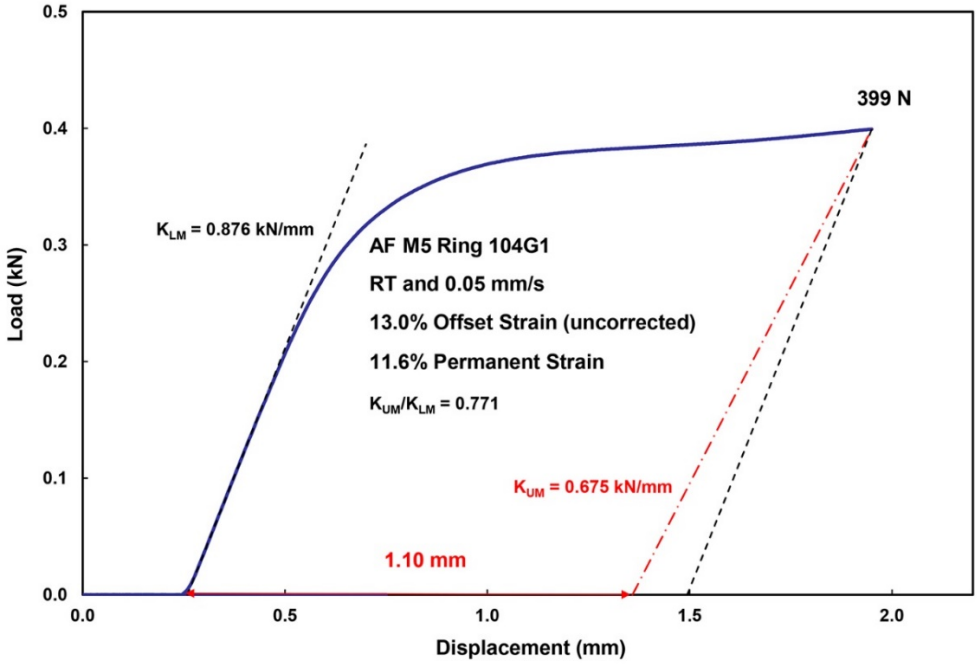

Figure 21: Load-displacement curve for AF 17×17 M5® ring displaced to 1.7 mm at RT and 0.05 mm/s.

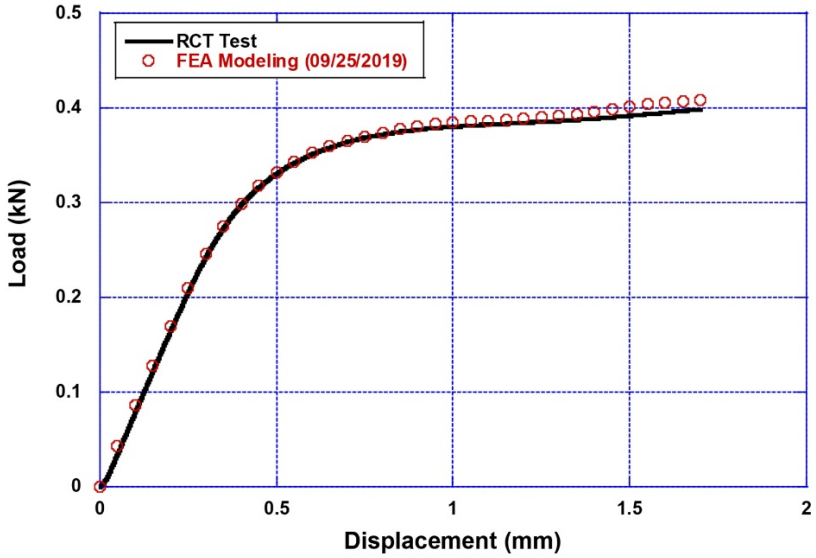

Figure 22: FEA-predicted and measured load-displacement curves for the 1.7-mm benchmark test.

FEA calculations were performed for stresses and strains prior to and after unloading. Figures 23 and 24 show the FEA hoop-stress predictions prior to unloading and following unloading, respectively. Prior to unloading, the peak tensile hoop stress was calculated to be 762.7 MPa. After unloading, the peak residual tensile hoop stress was 446.5 MPa. As for the 0.7-mm displacement test, the presence of residual stresses is due to elastic contraction with localized, non-uniform regions of plastic deformation.

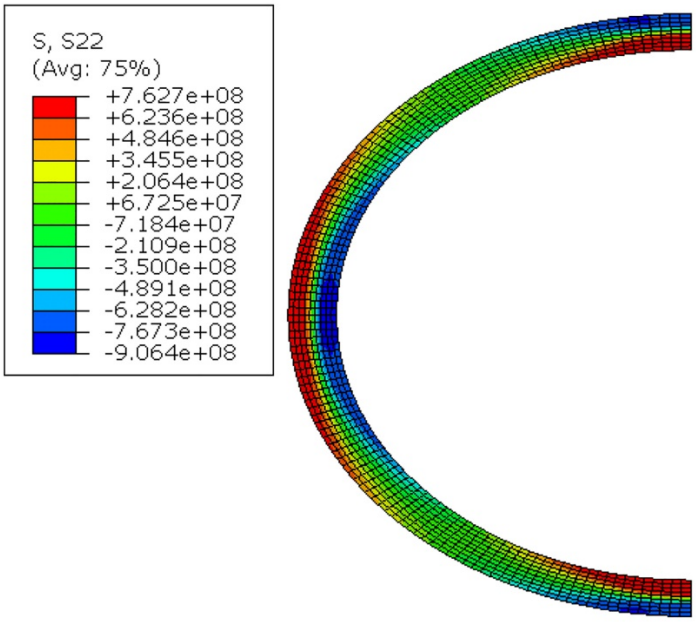

Figure 23: FEA-predicted hoop stress distribution at 1.7-mm displacement.

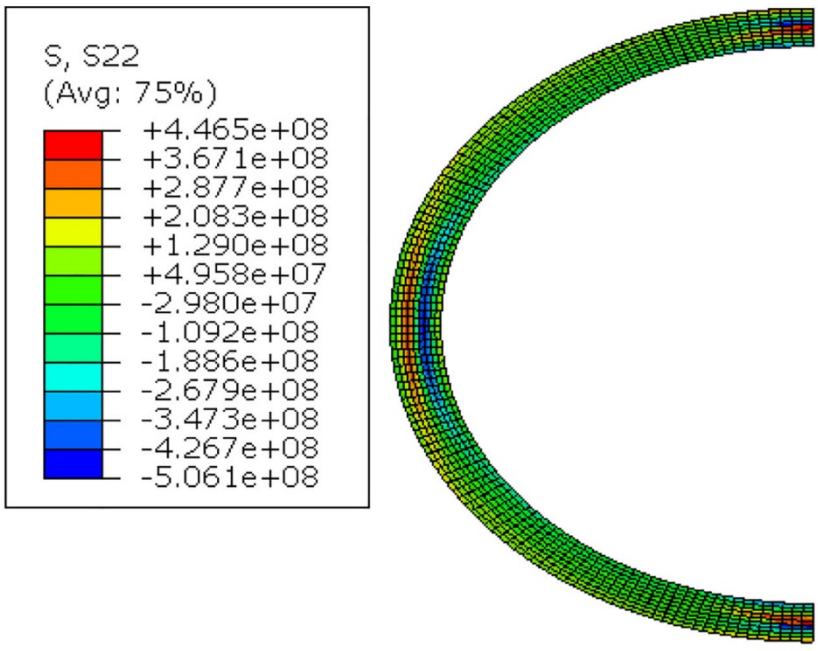

Figure 24: FEA-predicted residual hoop stress after unloading from 1.7-mm displacement.

Figures 25−26 show the FEA-calculated plastic hoop strain distributions before after unloading from 1.7-mm displacement. The maximum plastic hoop strain (0.08819, 9.2% engineering strain) occurs at the inner surface below the load and above the support. Figure 26 shows some decrease in maximum plastic hoop strain after unloading (0.08737, 9.13% engineering strain). For this displacement, the maximum plastic hoop strain (9.13%) is lower than the permanent structural strain (11.6%).

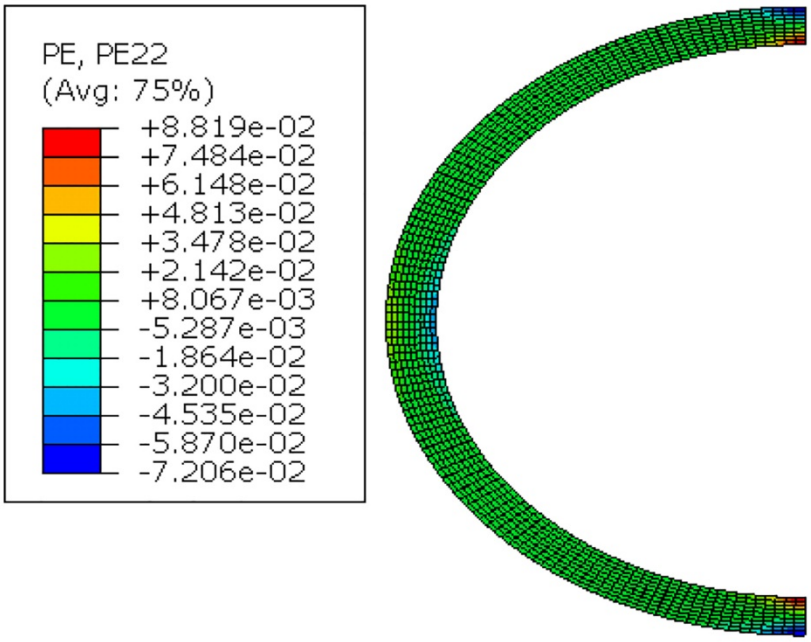

Figure 25: FEA-predicted plastic hoop strain at 1.7-mm displacement.

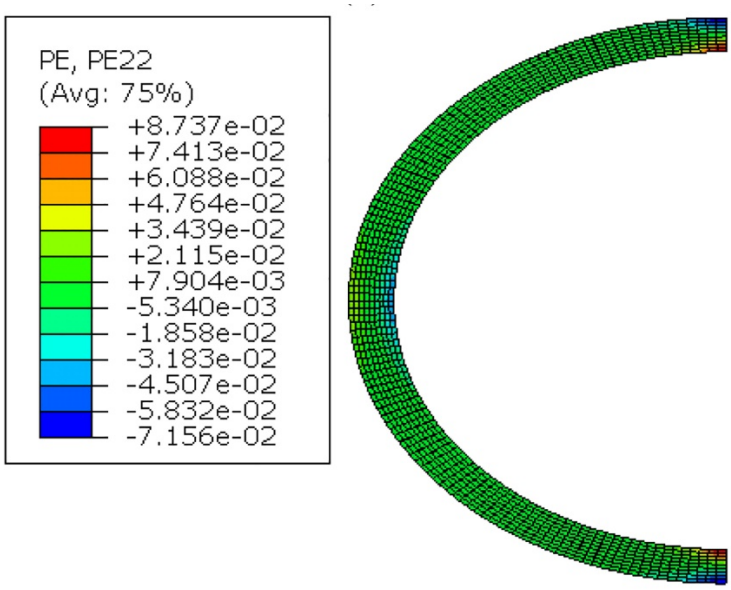

Figure 26: FEA-predicted plastic hoop strain after unloading from 1.7-mm displacement.

3.2 ELASTIC DISCONTINUITY STRESSES

For a welded pressurized tube, the weld region prevents the tube material from expanding in the radial direction. This induces axial bending stresses, which result in circumferential stresses via Hooke's law. The "rule of thumb" is that these discontinuity stresses become insignificant at a distance of one outer diameter from the weld. However, this rule of thumb is based on shell theory for thin-walled pressure vessels. FEA calculations were performed for an AF M5® tube with 9.50-mm outer diameter and 0.57-mm subject to 12.84 MPa internal pressure at RT and 0.17 MPa external pressure. These conditions result in elastic deformation of the pressure tube. The FEA calculations are compared to closed-form solutions for thick-walled tubes. The elastic properties of the tube and weld region are the same as those used for the RT RCT benchmark calculations: E = 91.9 GPa and ν = 0.37.

Figure 27 shows both the FEA-calculated hoop stress (includes effects of the weld) and the thick-wall-formula calculations (excludes end effects) for the inner surface, the wall-average value, and for the outer surface. The results are interesting from two perspectives: (a) the stress discontinuity length at which hoop stresses are within 1% of the pressurized-tube values is only 5.7 mm, which is 60% of the tube outer diameter and (b) there is a stress gradient across the cladding wall that is often ignored in correlating radial hydride precipitation with RHT hoop stress at the PCT. Additional calculations are presented in the next section for an irradiated 17×17 ZIRLO® rodlet at 350°C.

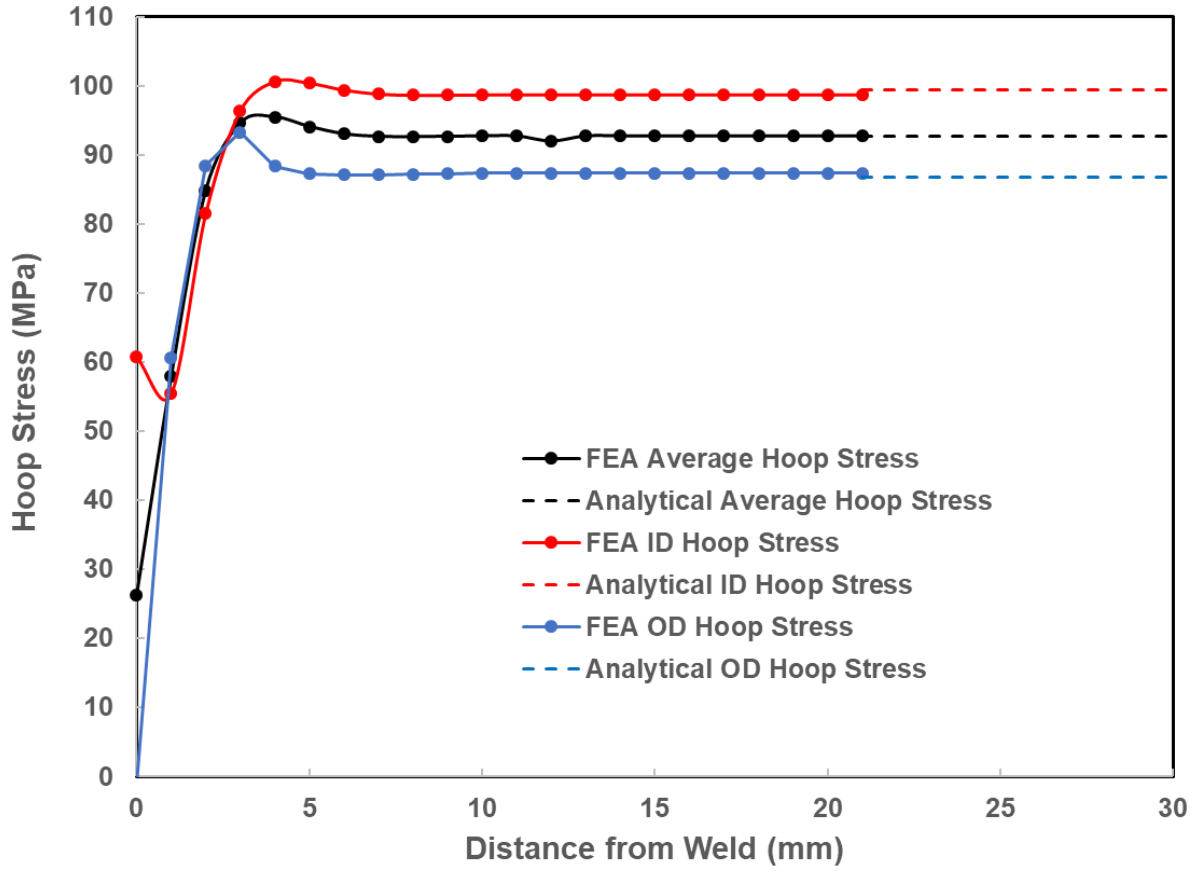

Figure 27: Axial variation of hoop stress near the welded end of a 17×17 AF M5® pressurized tube.

4. EFFECTS OF HOOP STRESS AT PCT ON ZIRLO® DTT

ZIRLO® rodlet 646B was subjected to RHT at 350°C PCT and 96-MPa wall-average hoop stress at 350°C. The RHT temperature history for this rodlet is shown in Fig. 3. RCT ductility results for 656B were given in Ref. 7 and compared to those for 646D (RHT at 350°C/87-MPa). As shown in Fig. 28, the DTT for the 87-MPa RHT sample was about 28°C, while the DTT for the 96-MPa was 143°C. The RCT results at 100°C (full ductility) for the ring closest to the bottom, solid insert were invalid due to the stress discontinuity in this region [7]. It was also argued in Ref. 7 that the RCT results at 170°C (full ductility) for the ring closest to the top, hollow insert were plausible. The data point at 170°C is not critical for determining the DTT. A simple linear interpolation between the 0.9% ductility at 120°C and the 3.5% ductility at 150°C gives 133°C DTT. Regardless of how high the ductility is for the 170°C ring, the DTT is in the range of 138±5°C. However, it is desirable to have at least two ductile data points and two brittle data points for DTT determination. Also, it is important to fully understand end effects in order to know how far from the ends RCT samples should be sectioned.

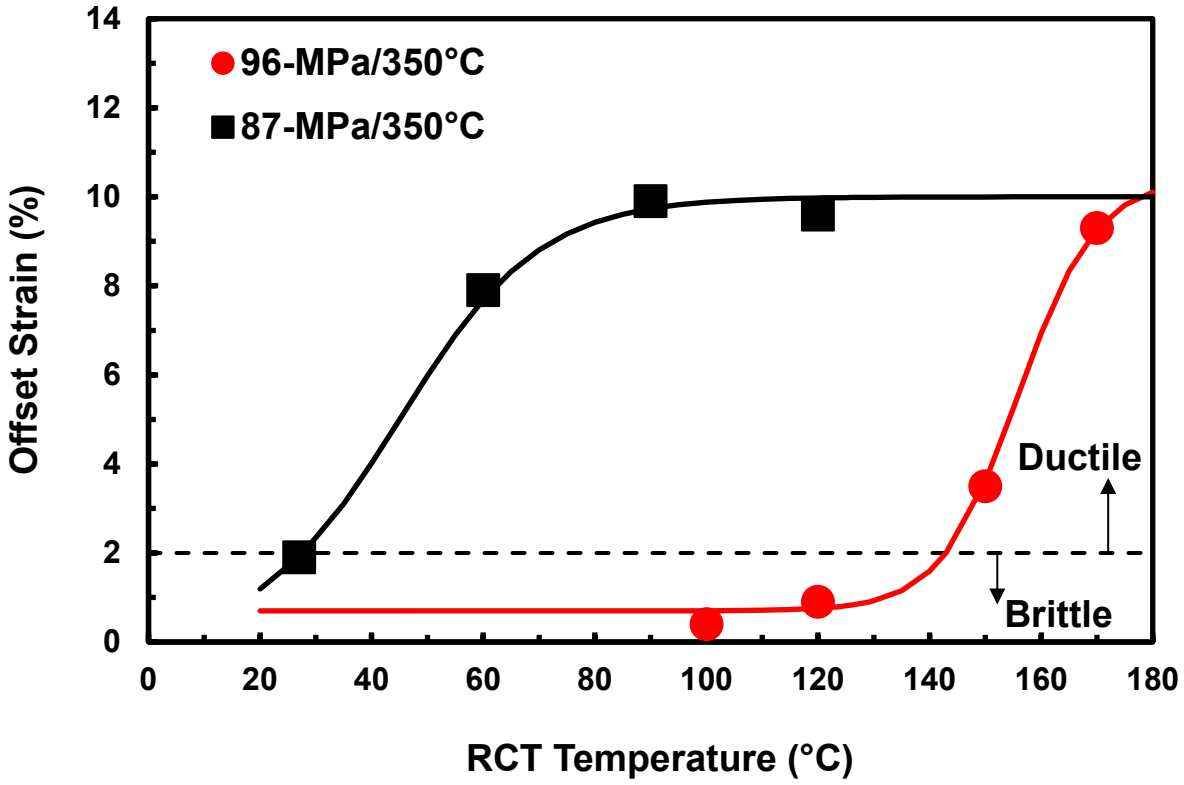

Figure 28: Ductility vs. RCT temperature results for ZIRLO® rodlets subjected to 350°C PCT and peak hoop stresses of 87 MPa (646D) and 96 MPa (646B).

The revised sectioning diagram for 646B is shown in Fig. 29. In the current work, additional metallographic examination (MET) was performed for bottom RCT Ring 3 (2, 3A, 3B, and 4), top RCT Ring 8 (8A, 8B), and 4-mm from the top weld within the 10-mm insert length.

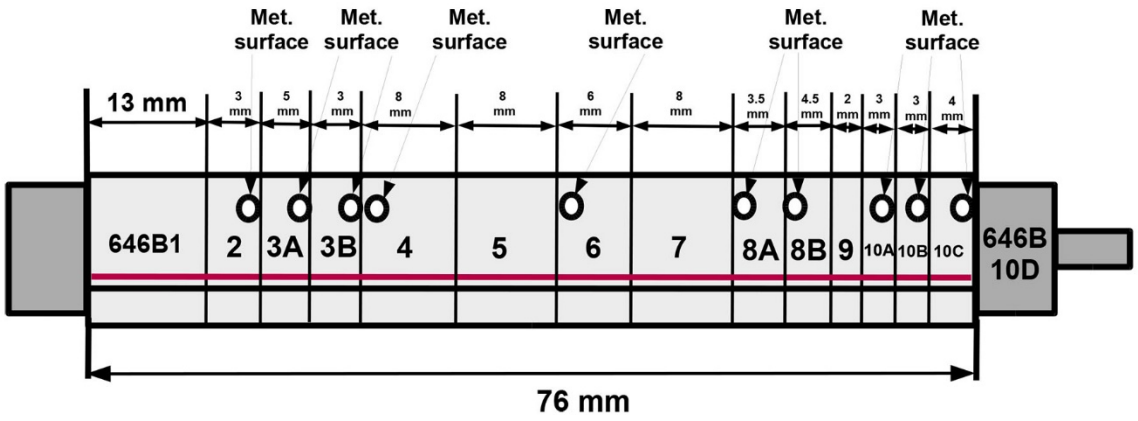

Figure 29: Revised sectioning diagram for ZIRLO® rodlet 646B.

Prior to showing the MET results, FEA stress-discontinuity results are presented because it is the combination of the analytical and experimental results that allow conclusions to be drawn. The solid bottom insert extended 10 mm into ring 646B1. For the FEA calculations, it was assumed that the solid insert is welded or bonded to the cladding. Elastic properties for highly irradiated ZIRLO® at 350°C are taken from Refs. 8–9: E = 70.1 GPa and ν = 0.37. The Zircadyne-702 end fixtures are assumed to have the same elastic properties. Measured cladding dimensions and rodlet pressures were used as inputs to the FEA model: 9.443-mm metal outer diameter (D_{mo}), 0.55-mm metal wall thickness (h_m), 12.84-MPa internal pressure (p_i) and 0.17-MPa external pressure (p_o). Away from the discontinuity zone near the ends, the thick-wall equation was used to predict hoop stresses at the inner wall (101.9 MPa), at the wall-average (95.9 MPa) and at the outer wall (90.5 MPa). Figure 30 shows the results of the FEA calculations as compared to calculated results using the thick-wall formula for hoop stress.

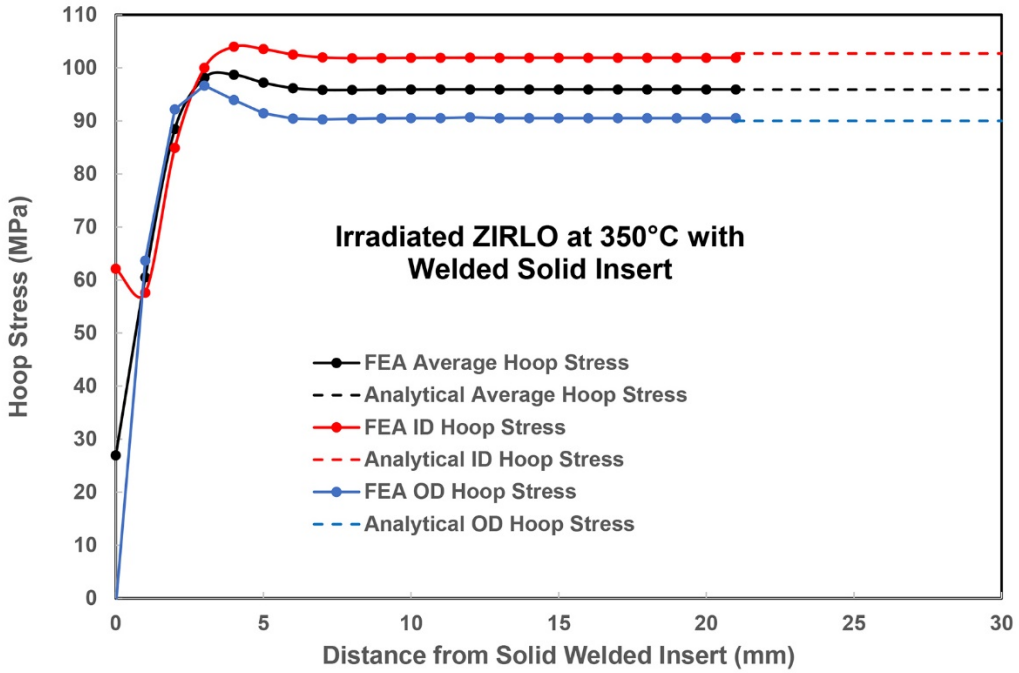

Figure 30: FEA-predicted hoop stresses for rodlet 646B at 350°C with a solid, welded bottom insert.

The FEA results are very similar to the results presented in Section 3 for M5® pressurized at RT. Inner-wall, average, and outer-wall hoop stresses are within 1% of the stresses calculated by the thick-wall formula at a distance of 5.6 mm ($0.6 \times D_{mo}$) from the end of the welded solid insert. MET was used to determine if the assumption of complete bonding of insert to cladding is too conservative (i.e., pessimistic). Recall that it took 10 attempts (two revolutions of Astro Arc weld head per attempt) to get a good weld at the bottom end-fixture flange.

The calculation was repeated for the top hollow-insert/weld region. The insert has a wall thickness of 1.41 mm and is assumed to have the same outer diameter as the measured cladding metal inner diameter (8.343 mm). The FEA-predicted axial profiles for inner-wall, average, and outer-wall hoop stresses are shown in Fig. 31. The hoop stress near the welded insert end is higher than for the welded-solid-insert case, but the stress-discontinuity region has the same axial length (5.6 mm for stresses to be within 1% of thick-wall-formula stresses). The inner-wall hoop stress at 0-mm from the insert is not shown in Fig. 30 because it is too high (118 MPa) to be consistent with the outer-wall and wall-averaged hoop stresses. The high result is considered to be a "hot spot" due to mesh spacing that is too coarse.

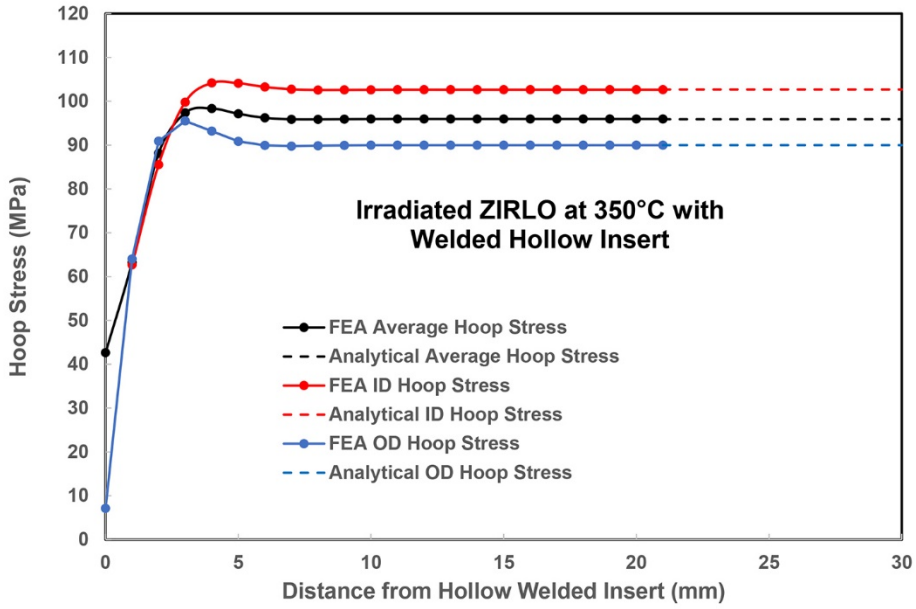

Figure 31: FEA-predicted hoop stresses for rodlet 646B at 350°C with a hollow, welded top insert.

The FEA calculated results shown in Figs. 30−31 are based on assumption of bonding between inserts and cladding at the ends of the cladding rodlet. MET can be used to refine these assumptions. The upper weld was completed with one attempt (2 rotations of the weld-head electrode). Also, to fit into the cladding, the insert has to be smaller in diameter than the cladding. Partial bonding is possible if molten weld material flows down through the small gap between the insert and the cladding and re-solidifies. Recall that the primary weld is a butt weld between the end-fixture flange and the end wall of the cladding. MET was performed for ring 10B, which was located 4 mm from the butt weld. Images of the as-polished 10B surface at 25X and 100X magnifications showed a RT gap (0−0.15 mm) between insert-outer and cladding-inner diameter (see Fig. 32 for local region of contact in 25X image). An etched-surface image was also taken at 200X to better clarify this region of contact. As shown in Fig. 33, the contact region is only 0.2-mm long and does not appear to be dense enough and strong enough to restrain cladding radial expansion.

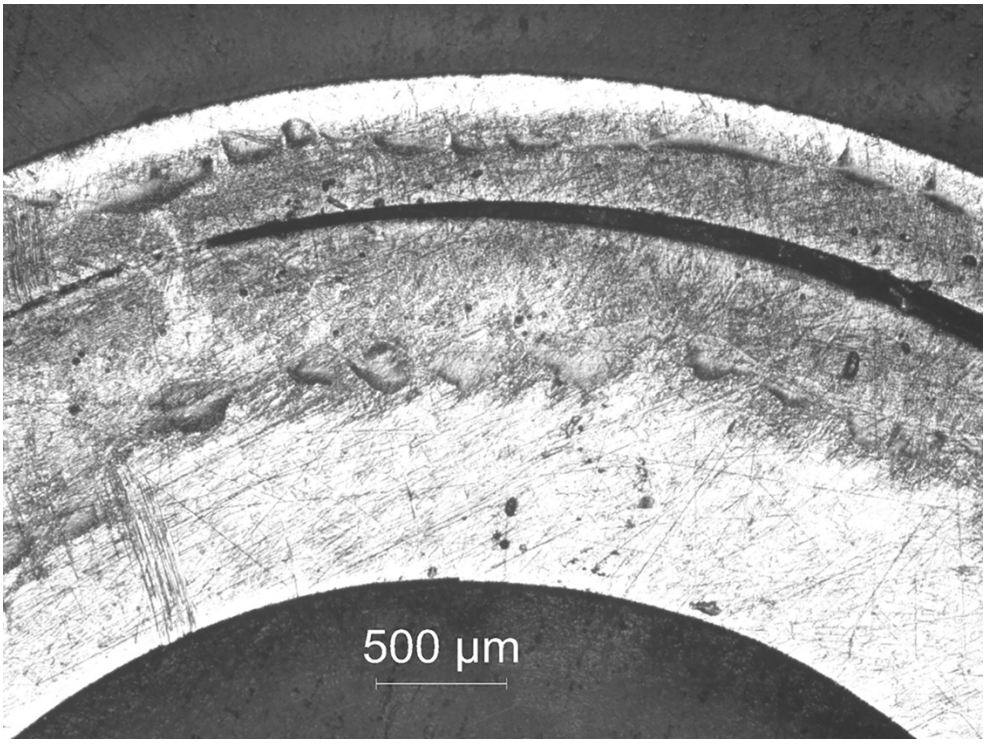

Figure 32: As-polished 25X-image of hollow insert (inner) and cladding at location 10B, 4 mm from butt weld.

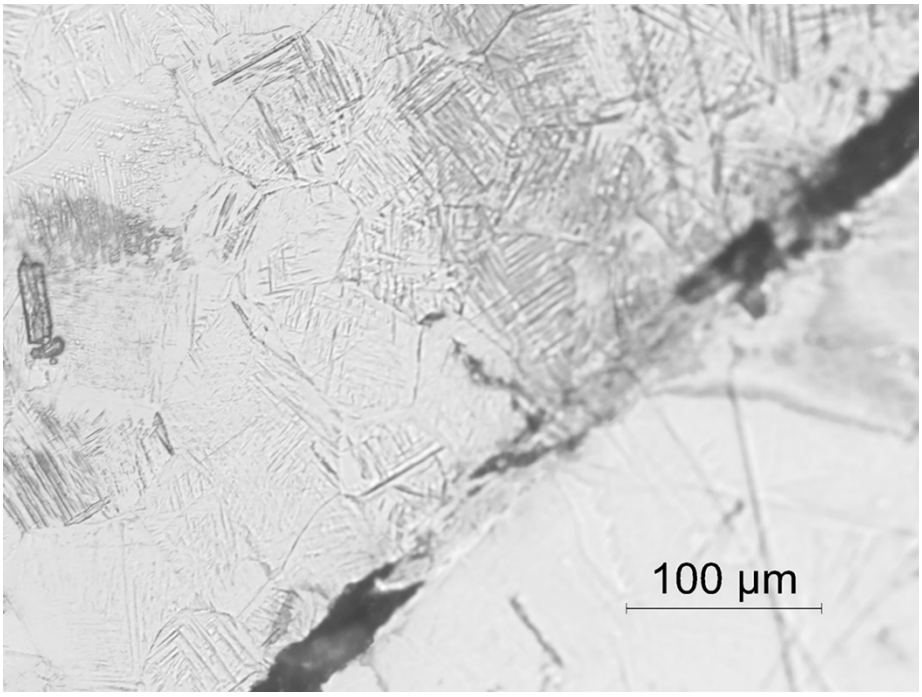

Figure 33: Etched 200X image of the contact area shown in the upper left of Fig. 32.

10B MET results suggest that the top, hollow insert would provide little-to-no restraint on cladding radial displacement. If restraint were assumed to occur at <4 mm from the weld, the stress discontinuity zone would be <9.6 mm from the weld. The RCT sample in question (8 in figure 29) was from an axial region 8−16 mm from the weld. With cutting loss, Ring 8 was closer to 8.4−16.4 mm from the upper weld. Discontinuity stresses may have had a small effect on <1.2 mm of Ring 8, which indicates valid RCT results for this ring.

The other MET surfaces identified in Fig. 29 were imaged in the etched condition to determine the effective length of radial hydrides (i.e., RHCF). The RHCF for these images was compared to the two sets of values for Ring 6 generated previously [7]. About forty 100X-magnification images were taken to visualize hydrides on the Ring 6 surface. The longer radial hydrides in each of the 100X images were imaged at 200X to determine continuity. On the basis of the longest radial hydride per 100X image, the RHCF was 26±8% and the maximum RHCF was 41%. The imaging process was repeated following regrinding/repolishing/re-etching to give 29±12% RHCF and 53% maximum RHCF. The longest radial hydride is shown in Figs. 34 (100X) and 35 (200X).

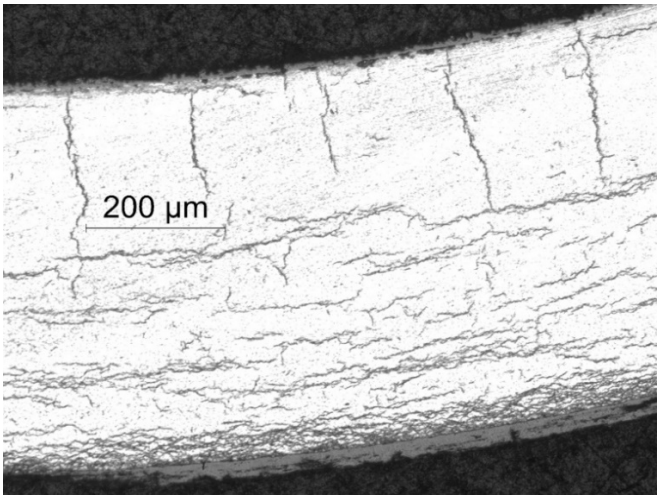

Figure 34: Longest radial hydride observed (at 100X) on the 646B6 surface.

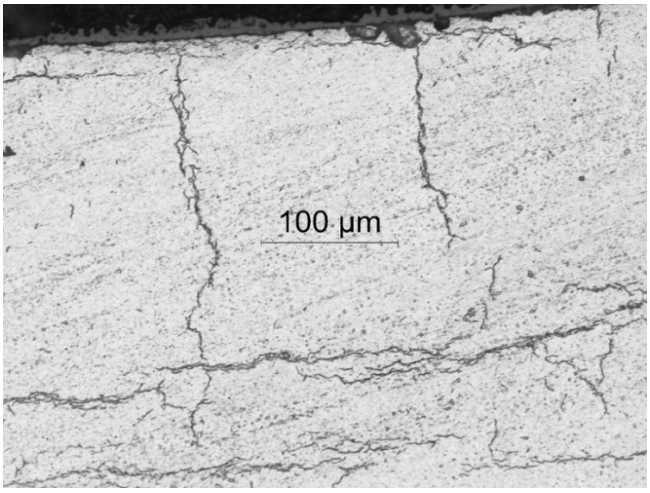

Figure 35: Longest radial hydride observed (at 200X) on the 646B6 surface.

Metallographic Examinations of Bottom RCT Ring 3

The RCT results for Ring 3 tested at 100°C (10.4% ductility) were inconsistent with RCT results for rings tested at 100°C (0.4%), 120°C (0.9%), and 150°C (3.5%). MET was conducted on the Ring 2 surface just below the bottom of Ring 3, near the mid-span of Ring 3, and at the top of Ring 3. The MET results for Ring 2, which was 6 mm from the bottom insert, clearly showed that the bottom of Ring 3 was in the stress-discontinuity region and perhaps in the heat-affected zone (HAZ). Based on 100X images at eleven circumferential locations, the RHCF was only 8±4% with 17% maximum RHCF (see Fig. 36). The circumferential hydrides below the hydride rim were much shorter than observed in images from surfaces farther away from the bottom insert. This may have been caused by hydrogen loss to the solid bottom insert and/or rapid cooling rates following welding.

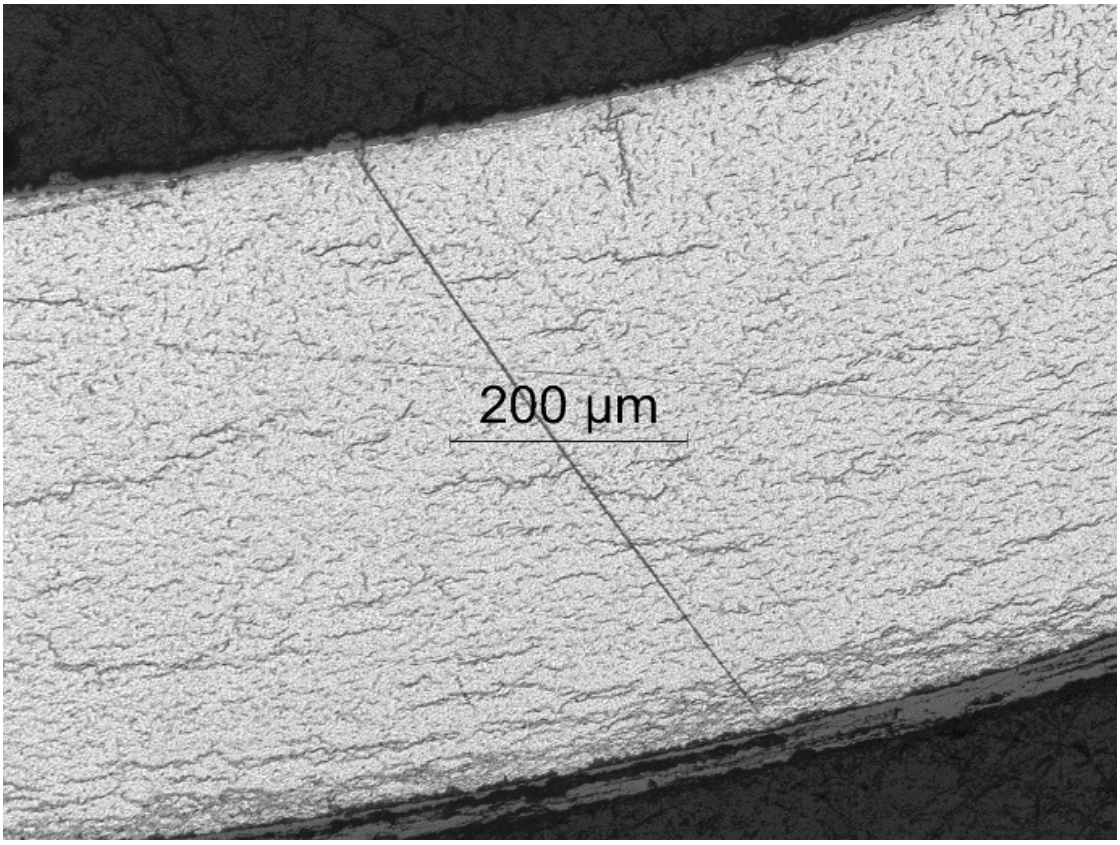

Figure 36: Maximum RHCF (17%) observed for the Ring 2 surface adjacent to the bottom of Ring 3.

Surface 3A, which was 11 mm from the bottom insert, was close to the mid-span of Ring 3. Images at 100X were taken at 15 circumferential locations. The radial hydrides were sufficiently long (23±7%) with 33% maximum RHCF (see Fig. 37). The length of the radial hydrides and the presence of mid-radius circumferential hydrides strongly suggest that the surface was located outside the stress discontinuity region and the HAZ. The continuity of radial hydrides is difficult to measure from 100X images because of the ≤5-µm gap allowed in the radial direction in the determination of continuity. The 200X image (Fig. 38) was used to determine continuity of the longest radial hydride on the 3A surface. The gap between radial hydrides was measured to be about 5 µm. It is assumed that a crack growing along the lower radial hydride could propagate rapidly to the next radial hydride across this 5-µm gap.

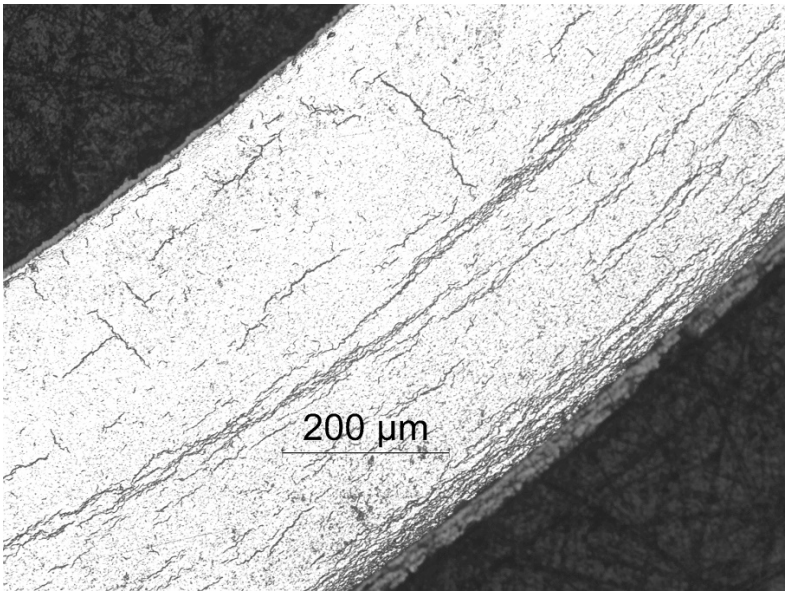

Figure 37: Maximum RHCF (33%) for surface 3A, which was 11 mm from the bottom insert.

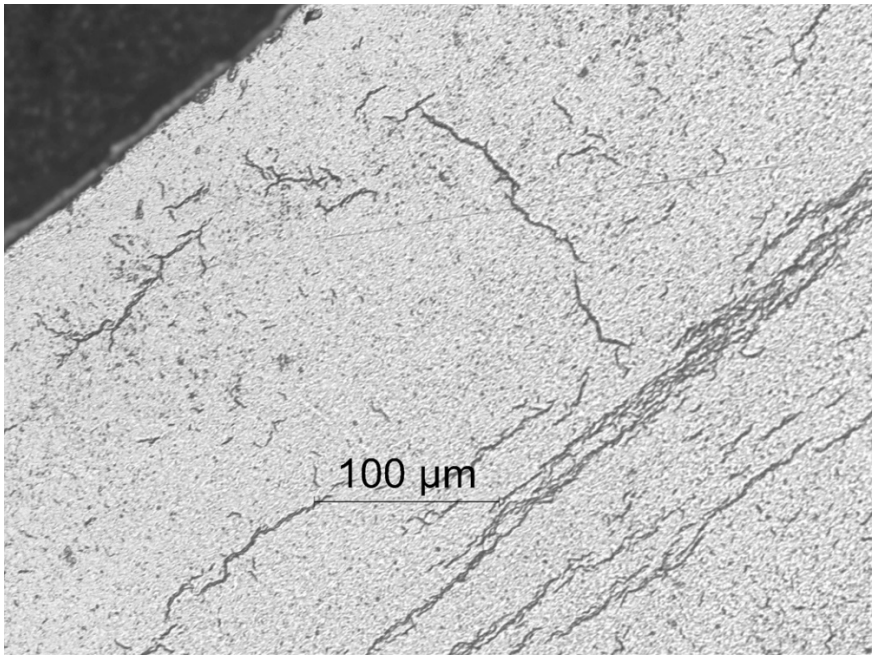

Figure 38: 200X image of longest radial hydride in Fig. 37.

The same radial hydride lengths were expected at the top of Ring 3 (surface 3B), which was 14 mm from the bottom insert. Thirty-five 100X images and selective 200X images were taken to determine that the RHCF was only 19±7% with a maximum value of 34%. The difference between the RHCF for MET samples 3A and 3B may have been due to the full-surface evaluation of radial hydrides for surface 3B because the maximum RHCF is about the same. Also, radial hydrides are not as continuous in the axial direction as circumferential hydrides are. Surface-to-surface variations are expected. Figures 39 (100X), 40 (200X) and 41 (500X) show images of the longest radial hydride on the 3B surface.

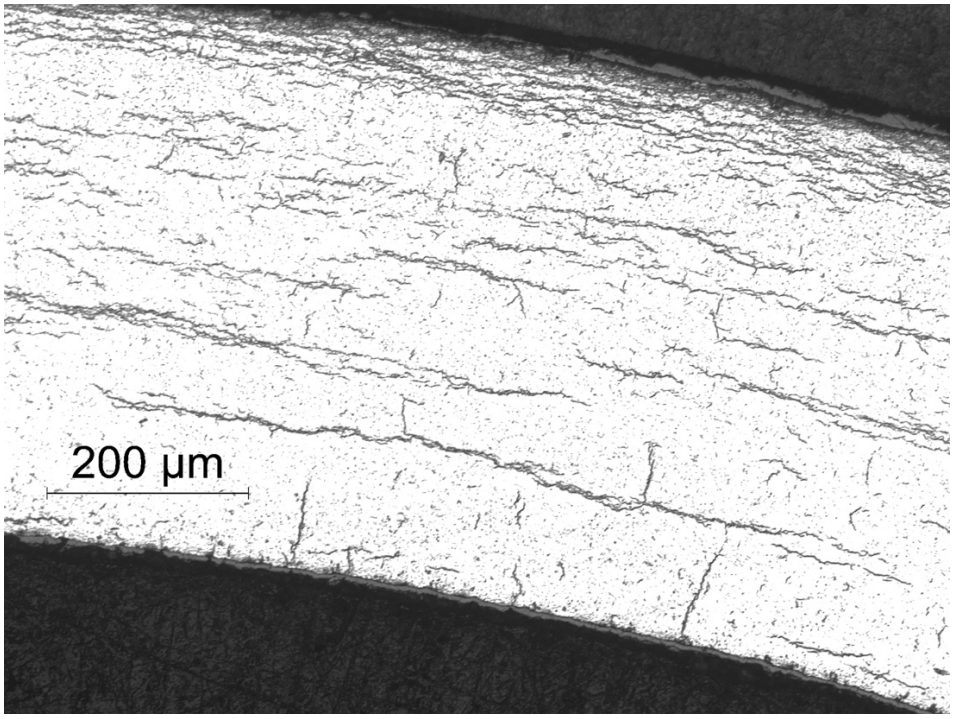

Figure 39: Maximum RHCF (34%) for surface 3B, which was 14 mm from the bottom insert.

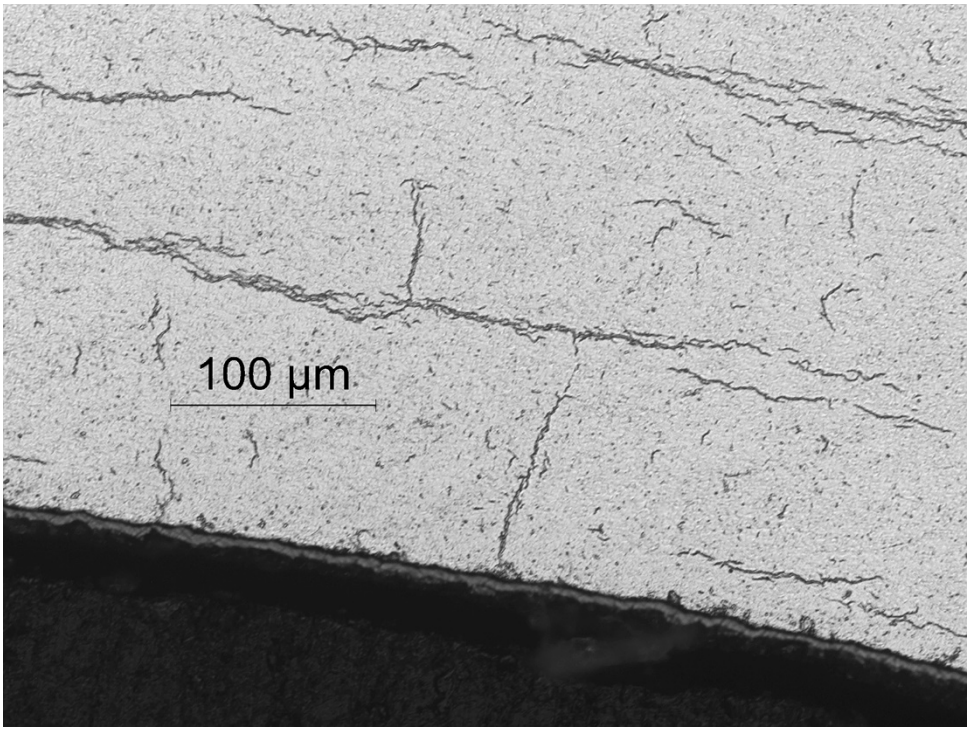

Figure 40: 200X image of the longest radial-circumferential-radial hydride in Fig. 39.

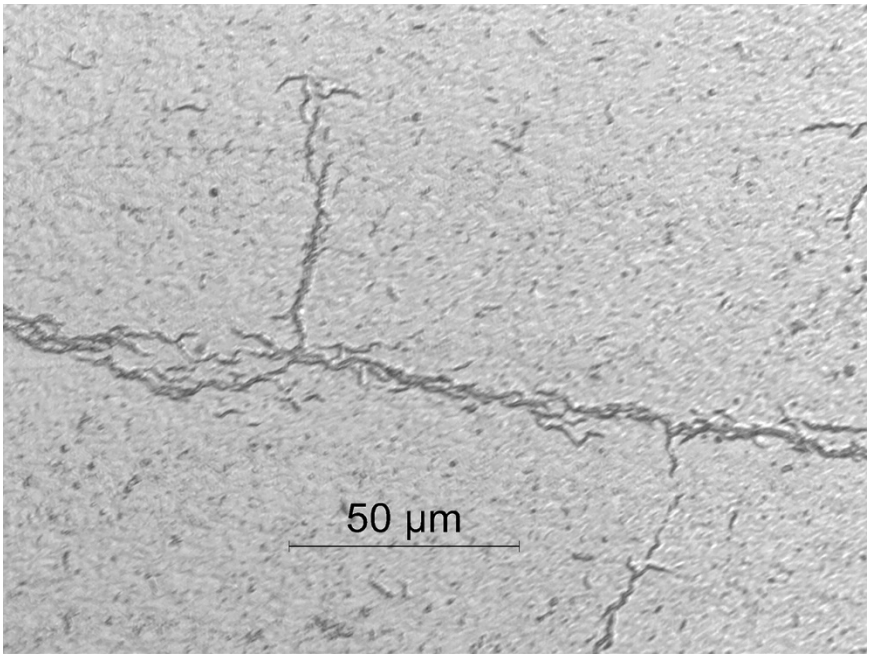

Figure 41: 500X image of location in Fig. 39 at which the two radial hydrides were assessed to be continuous (≤5-µm gap).

Minor cracks through the hydride rim were observed at the top end of Ring 3 (3B) at about the 3 o'clock location. These are shown in Fig. 42. Such end cracks were not observed at the mid-span location (3A) of Ring 3.

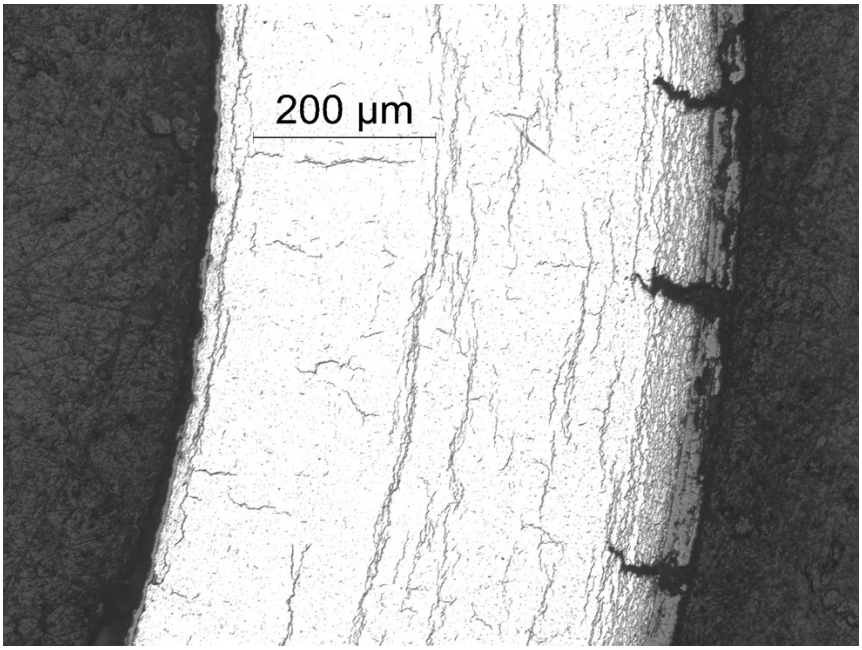

Figure 42: Minor cracks through the hydride rim at about the 3 o'clock location of surface 3B.

Averaging the RHCF values measured on surfaces 2, 3A, and 3B gives 18±9%, which is too low for significant cracking to occur during a RCT at 100°C.

The decrease in RHCF from 23±7% at 11 mm (Surface 3A) from the bottom insert to 19±7% at 14 mm (Surface 3B) from the bottom insert was not expected. However, it was within the variation measured for surface 3A. In order to double-check the 19±7% RHCF at 3B, the lower surface of Ring 4 was examined.

The plan was to look at the lower surface and mid-span of Ring 4, but the ring was visibly cracked and may not have survived the sectioning process. Taking into account sectioning (0.4 mm), and grinding (≈0.1 mm for each surface), the estimated location of the Ring 4 surface is 14.6 mm from the bottom insert. Thirty-nine overlapping 100X images were taken and 200X images were obtained for the longer radial hydrides to assess continuity. Similar results were obtained for the Ring 4 surface (20±7% RHCF with 34% maximum RHCF) as for the 3B surface. However, more and deeper cracks were observed. These cracks may have initiated within Ring 4, which should have a RHCF >25%, and propagated to the ends of the ring. The circumferential orientation of the Ring 4 surface was not preserved, so location relative to the RCT loading line is estimated for each of the three main cracks observed. Figures 43 and 44 show cracks that initiated at the cladding inner surface. These two locations are assumed to be at the 12 and 6 o'clock positions. Figure 45 shows a crack at the assumed 3 o'clock orientation that appears to have initiated at the cladding outer surface.

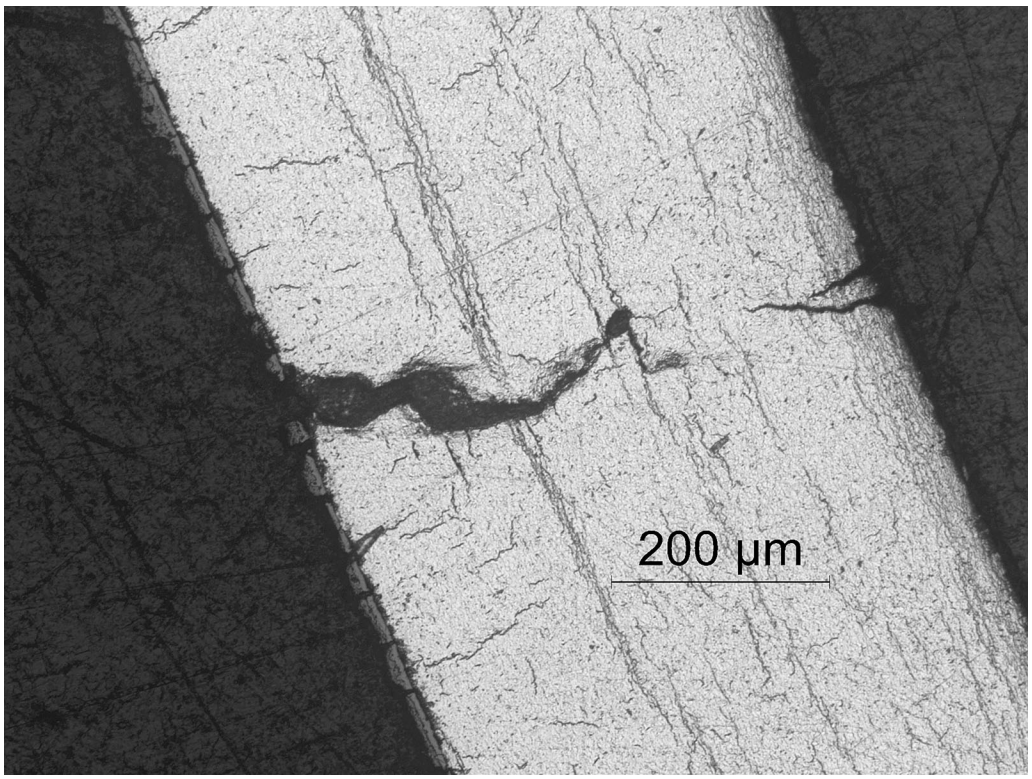

Figure 43: Cracking observed at the assumed 12 o'clock location of the bottom end of Ring 4.

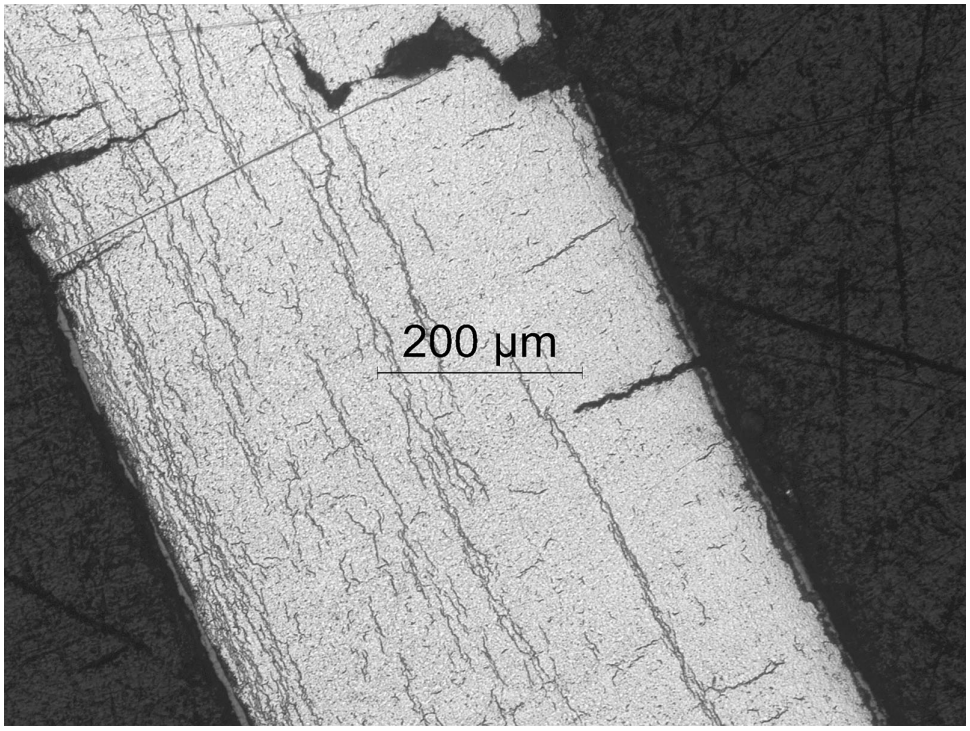

Figure 44: Cracking at the assumed 6 o'clock location of the bottom end of Ring 4.

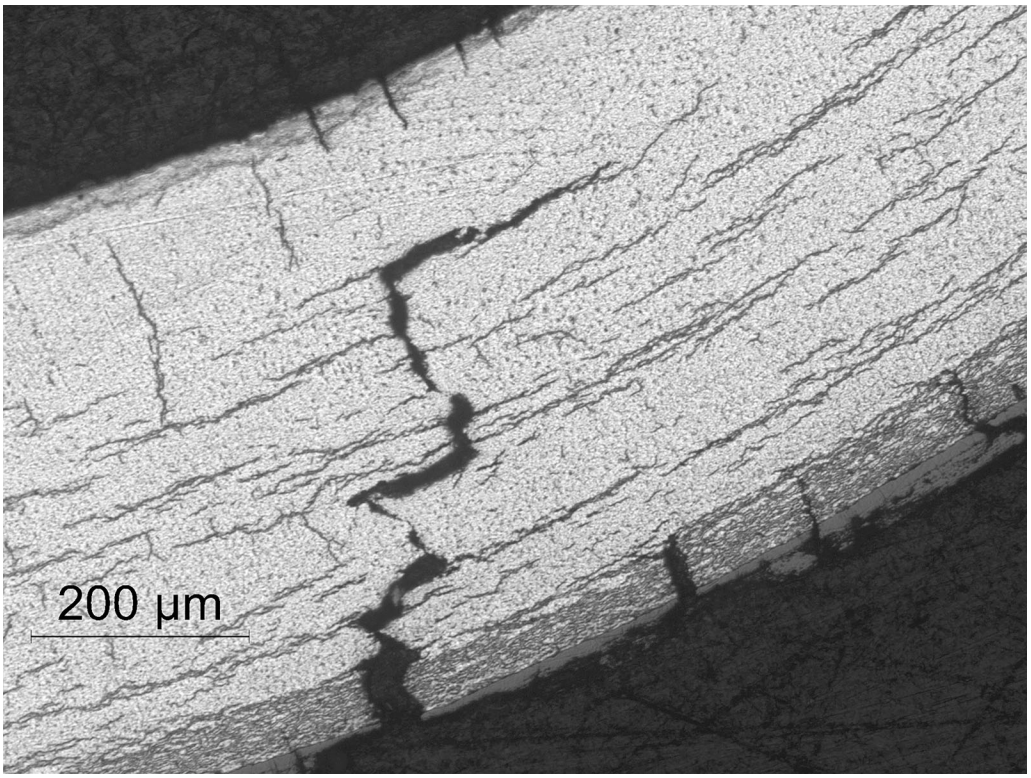

Figure 45: Cracking at the assumed 3 o'clock location of the bottom end of Ring 4.

Metallographic Examinations of Top RCT Ring 8

Surface 8A was located at the bottom of Ring 8, which was 22 mm below the top, hollow insert. Overlapping 100X images (35) were taken to get full-surface results. Images were also taken at 200X to assess radial hydride continuity. The results were within the scatter observed for MET sample 6 (28±10% RHCF with 53% maximum RHCF). The average and one-standard deviation for radial hydrides observed in the 35 images was 25±10% with a maximum value of 44%. Figures 46 (100X) and 47 (200X) show the longest radial hydride observed on the Ring 8A surface. No cracking was observed on this surface for the ring tested at 170°C.

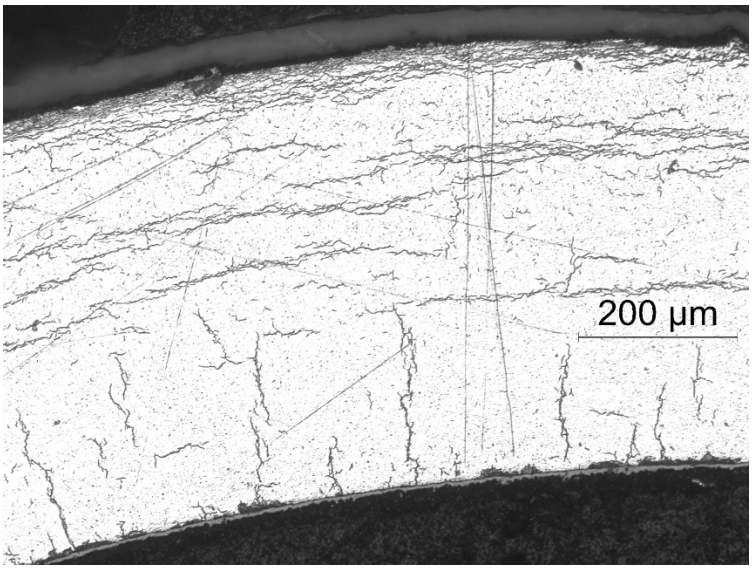

Figure 46: Maximum RHCF (44%) observed at 100X on the 8A surface.

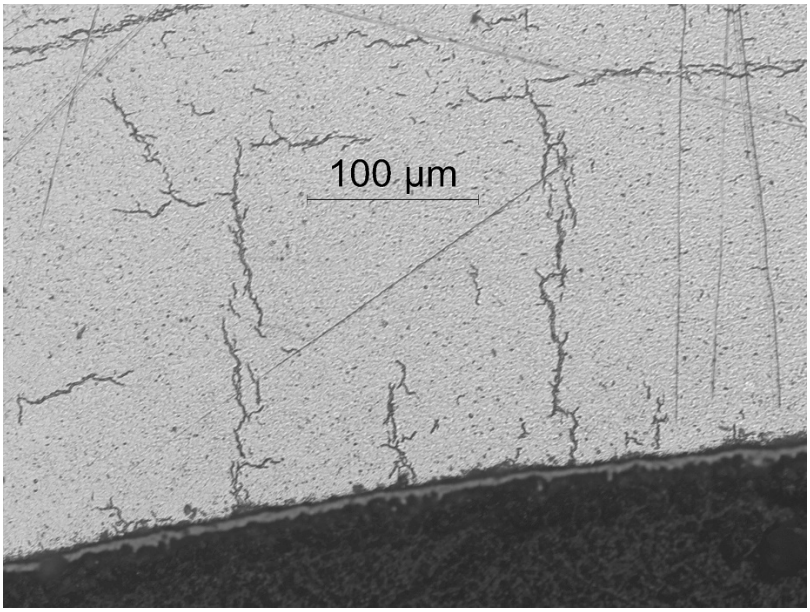

Figure 47: 200X image of the longest radial hydride observed in Fig. 46.

MET surface 8B was about 18 mm from the bottom of the top, hollow insert. Overlapping images at 100X and selective images of radial hydrides at 200X were taken to determine 26±10% RHCF with 44% maximum RHCF. Recall [7] that the first set of results for MET sample 6 were 26±8% RHCF and 41% maximum RHCF. As with surface 8A, no cracking was observed. Figures 48 (100X) and 49 (200X) show the longest radial hydride observed on the 8B surface.

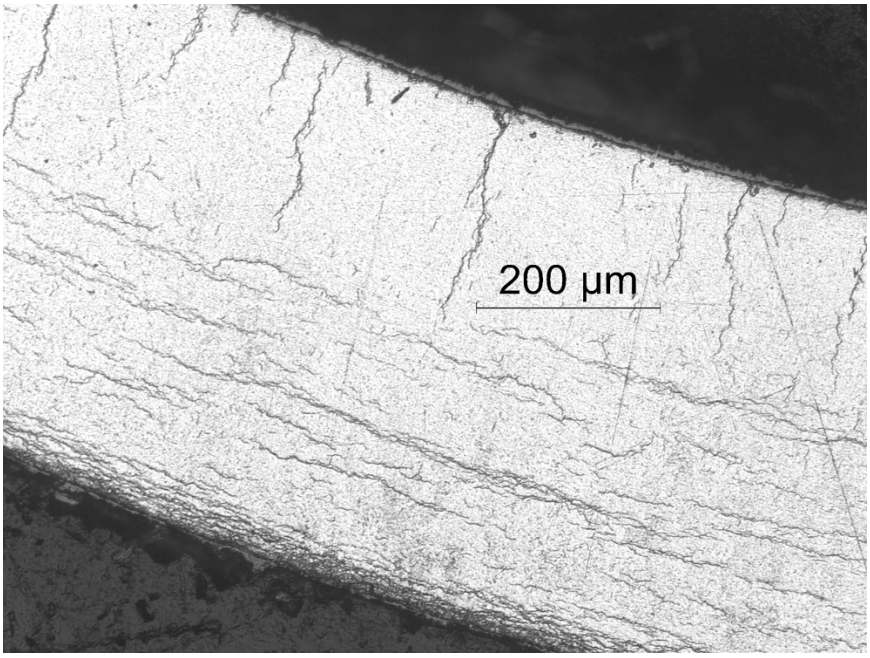

Figure 48: Image taken at 100X containing the maximum RHCF (34%) observed for Ring 8B.

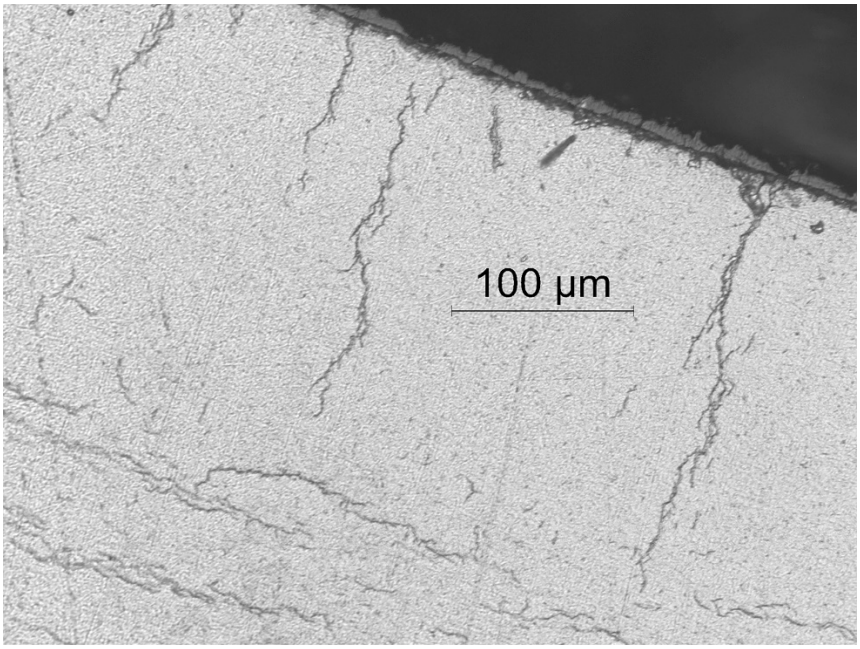

Figure 49: Image taken at 200X containing the longest radial hydride in Fig. 48.

Summary of Metallographic Examination Results for Bottom (3) and Top (8) RCT Samples

RCT and MET results confirm that the bottom RCT ring (3) was too close to the solid, bottom insert to be representative of rodlet material subjected to peak RHT conditions of 350°C and 96-MPa hoop stress. Although no MET could be performed on Ring 9 closest to the top hollow insert, the preponderance of results indicates high confidence in the RCT results at 170°C for Ring 8. Figure 50 shows the measured axial profile for RHCF. The results are consistent with our current understanding of the length of the stress discontinuity zone. The small decrease in average RHCF at 14 mm appears to be insignificant because of the scatter (i.e., standard deviation) in the data at other axial locations.

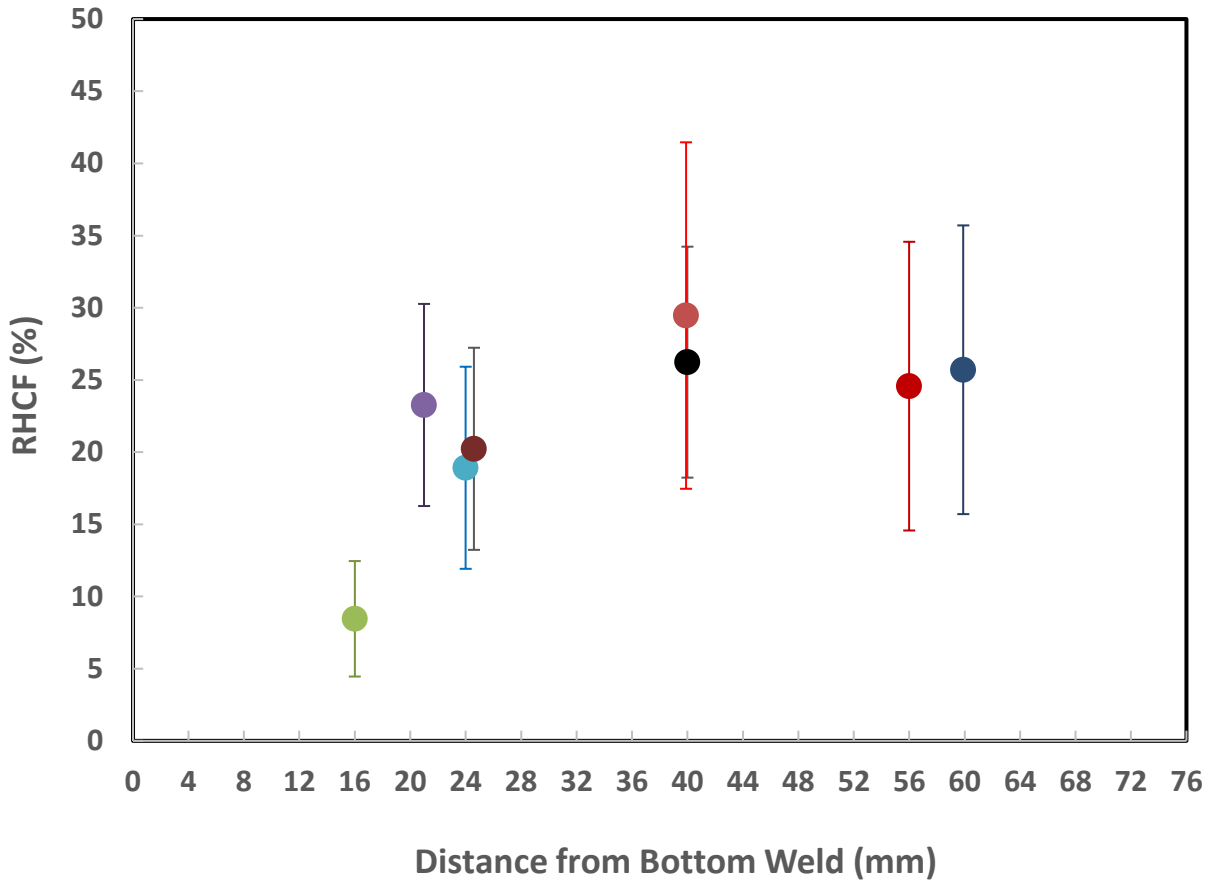

Figure 50: Axial profile of measured RHCF relative to the bottom weld. The solid weld insert was 10 mm from the bottom weld and the data point at about 60 mm was about 6.5 mm from the 10-mm top, hollow insert.

5. CHARACTERIZATION OF M5® SIBLING PIN CLADDING

The 12 sibling-pin cladding segments received from ORNL are described in Table 1. Two M5® segments were selected for metallographic examination and RCT sample sectioning: (a) 653B (ORNL ID 30AD05 3259 3349), which is in the as-irradiated condition and (b) 654B (ORNL ID 30AE14 3309 3399), which is in the FHT condition [4]. The axial locations in the ORNL IDs are approximate (not accurate to the mm) because of cutting losses. The nominally 90-mm segments were not exactly 90 mm (e.g., 653B was 89-mm long).

5.1 MET RESULTS FOR AS-IRRADIATED M5® SEGMENT 653B

Figure 51 shows the pre-sectioning diagram for segment 653B. Cutting losses and losses due to squaring/deburring resulted in about 5 mm of material loss. Figure 52 shows the post-sectioning diagram. The RCT sample lengths were in the range of 8.05±0.09 mm, where 0.09 mm is one standard deviation.

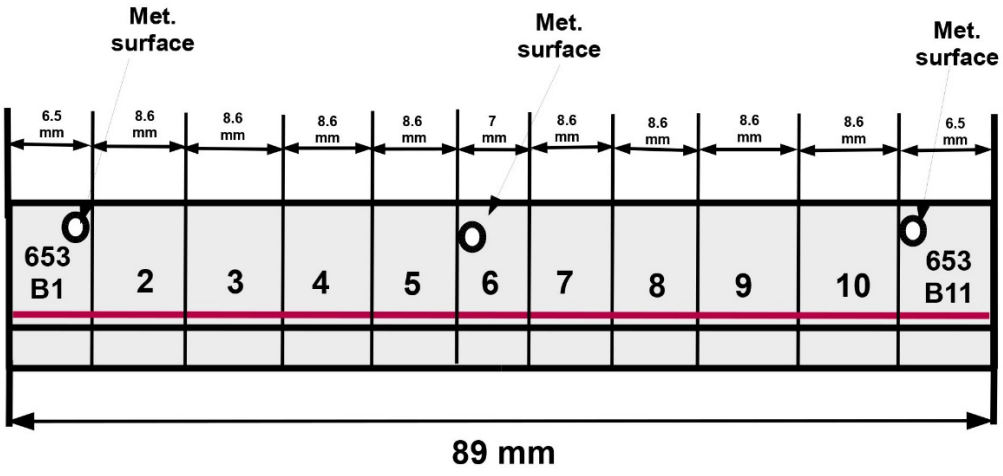

Figure 51: Pre-sectioning diagram for as-irradiated M5® segment 653B. Segment top is to the left.

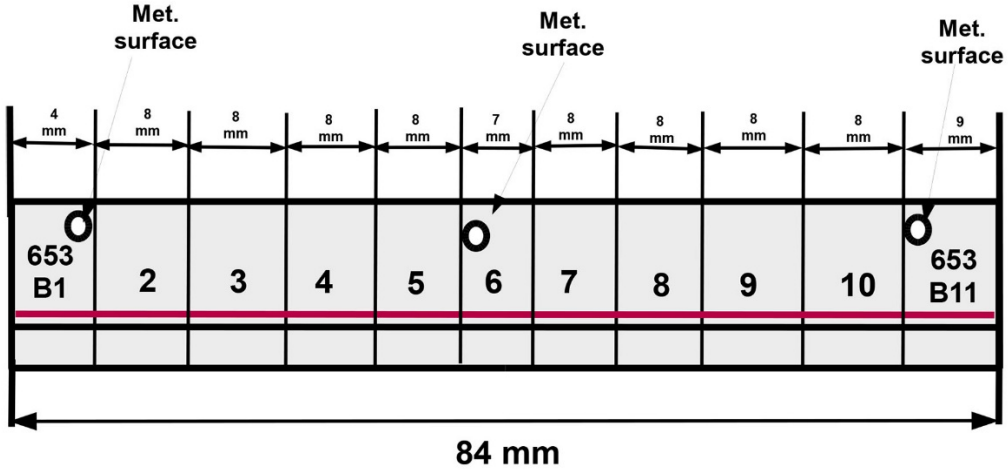

Figure 52: Post-sectioning diagram for as-irradiated M5® segment 653B. Segment top is to the left.

Prior to sectioning the outer diameter (D_o) was measured at three axial locations with two orientations per axial location. The results are accurate to two decimal places: 9.377±0.005 mm, which is essentially a uniform 9.38 mm. Metallographic examination was performed for the indicated surface of Ring 6 in Fig. 51. The approximate axial location of this surface was 3300 mm from the bottom of fuel rod 30AD05. Oxide layer thickness (h_{ox}) was measured from 500X images at 12 circumferential locations. These locations were carefully chosen to avoid regions with oxide loss that occurred during grinding. It was interesting to observe the effects of image focusing. A slight under-focus made h_{ox} appear thicker, dark gray and less distinct. A slight over-focus made h_{ox} appear thinner with regions of gray and white. The criterion for choosing a focused image (i.e., no white areas) was used consistently to determine 13±1 µm for h_{ox}. Based on previous experience, the estimated hydrogen content (C_H), which will be measured by ORNL, is 90±10 wppm. The cladding metal outer diameter (D_{mo}) was calculated from $D_o - 2\ h_{ox}$ to be 9.351±0.001 mm, which rounds off to 9.35 mm. Fourteen images at 100X were used to measure the metal wall thickness (h_m): 549±3 µm = 0.549 mm. The metal wall inner diameter (D_{mi}) was calculated to be 8.254±0.006 mm. The ratio $D_{mi}/2h_m$ = 7.526±0.045 is used to convert pressure to hoop stress.

The 653B6 surface was etched to bring out the hydrides, which were primarily in the circumferential direction. Only two short radial hydrides (7−10% of the cladding wall) were identified (see Figs. 53−54). The apparent thickness of these hydrides may result from the etching process or from higher C_H.

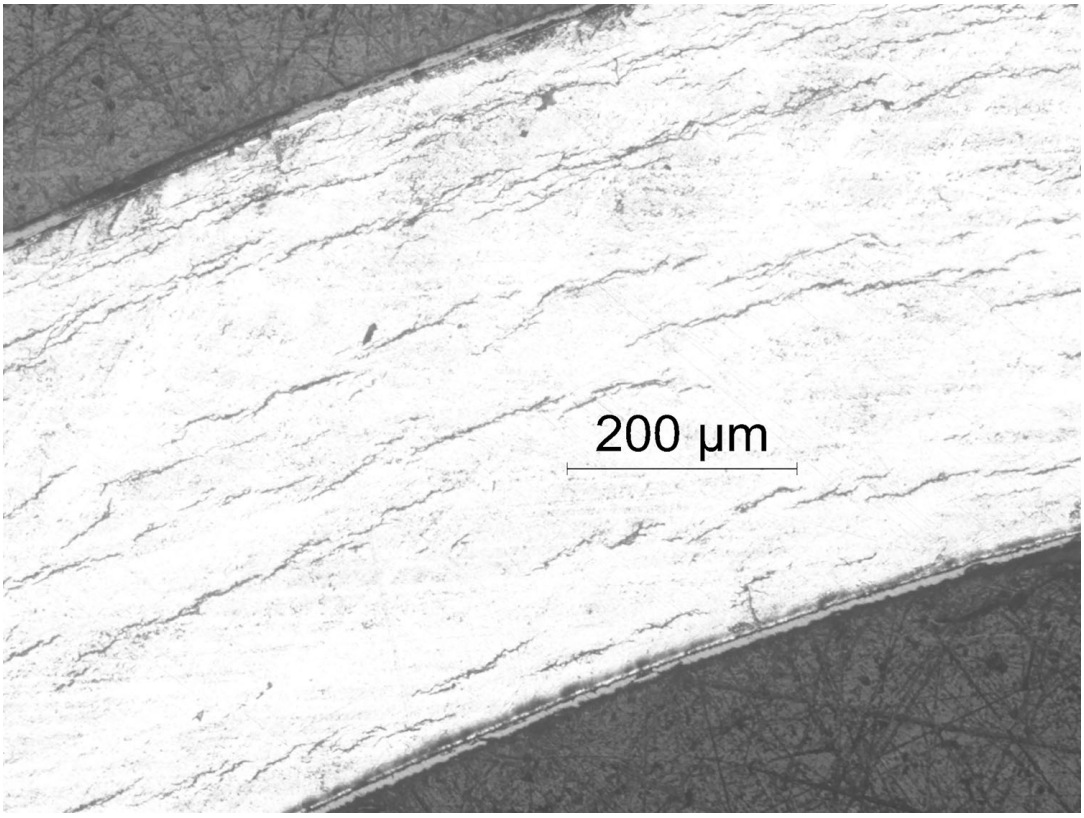

Figure 53: Short radial hydride (7%) observed on as-irradiated M5® surface of 653B6.

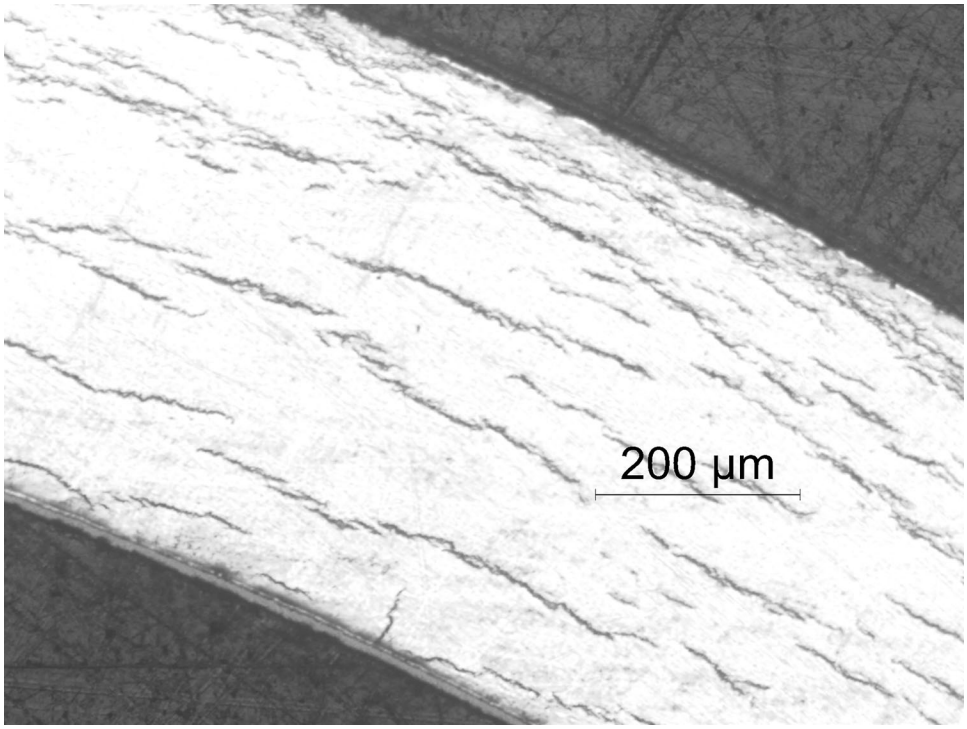

Figure 54: Short radial hydride (10%) observed on as-irradiated M5® surface of 653B6.

Figures 55−56 show hydrides previously observed [13] in as-irradiated M5® (surface 652E6G) from a fuel rod irradiated to 72 GWd/MTU in the North Anna reactors. The segment examined contained 76±5 wppm hydrogen. Radial hydrides in Figs. 55−56 were longer than the ones shown in Figs. 53−54. Also, the hydrides in Figs. 55-56 appear to be thinner than the ones shown in Figs. 53−54. Based on the differences in oxide layer thickness (8±1 µm for surface 652E6G vs. 13±1 µm for 653B6), the hydrogen content of the as-irradiated sibling-pin M5® is expected to be higher (estimated 90±10 wppm) than 80 wppm, which may account for the thicker hydrides observed.

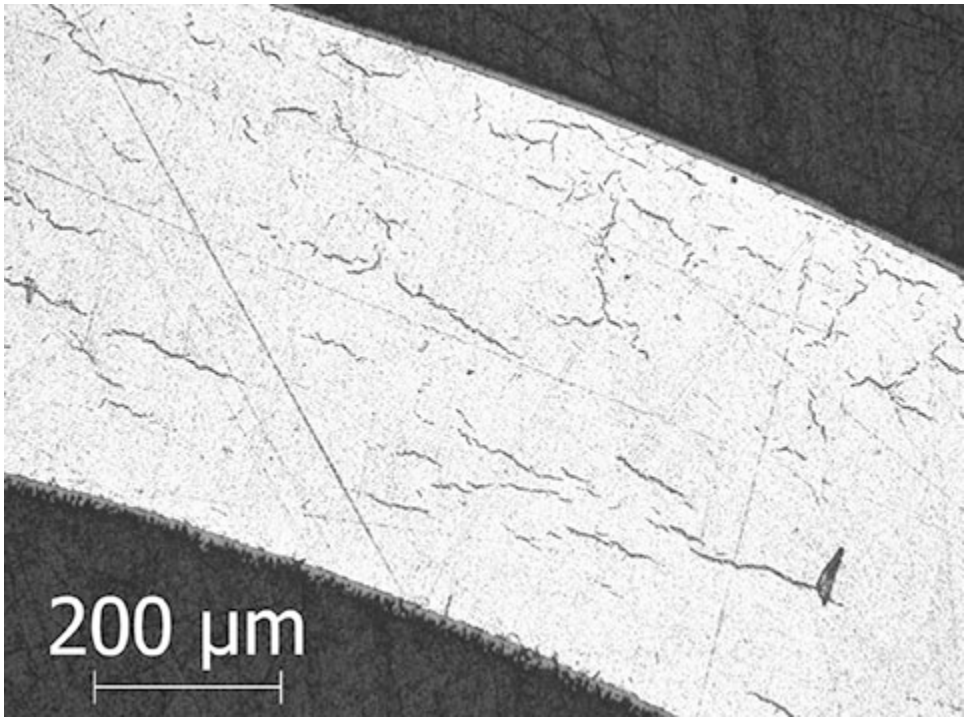

Fig. 55: Radial and circumferential hydrides in as-irradiated (72 GWd/MTU), baseline [13] M5® at the 2 o'clock position of surface 652E6G.

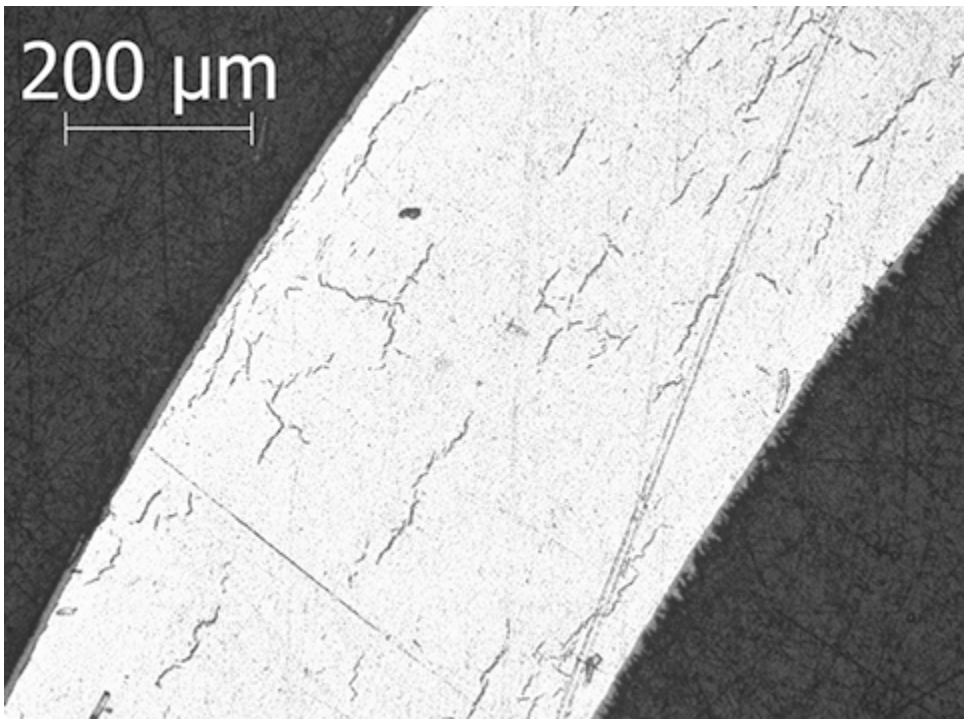

Figure 56: Radial and circumferential hydrides in as-irradiated (72 GWd/MTU), baseline [13] M5® at the 10 o'clock position of surface 652E6G.

5.2 MET RESULTS FOR HEAT-TREATED M5® SEGMENT 654B

Segment 654B is from fuel rod 30AE14 at an axial location approximately 3309−3399 mm from the bottom of the fuel rod. During FHT, control of the top heater was lost during the heating ramp such that 654B was heated initially to a peak temperature of 485°C. During the 8-h hold time, the temperature had coasted down to 401°C as the cooling was initiated at an average rate of 3.6°C/h. For M5® cladding with about 70−100 wppm hydrogen, full dissolution of hydrogen would occur rapidly at about 300−330°C, respectively. From the perspective of radial hydride dissolution and precipitation, the overheating should have had no significant effect assuming that partial annealing of irradiation damage did not occur during the 401−485°C phase of the FHT.

Figure 57 shows the pre-sectioning diagram for segment 654B. Cutting losses and losses due to squaring/deburring resulted in 8 mm of material loss. Figure 58 shows the post-sectioning diagram. The RCT sample lengths were in the range of 7.88±0.23 mm, where 0.23 mm is one standard deviation.

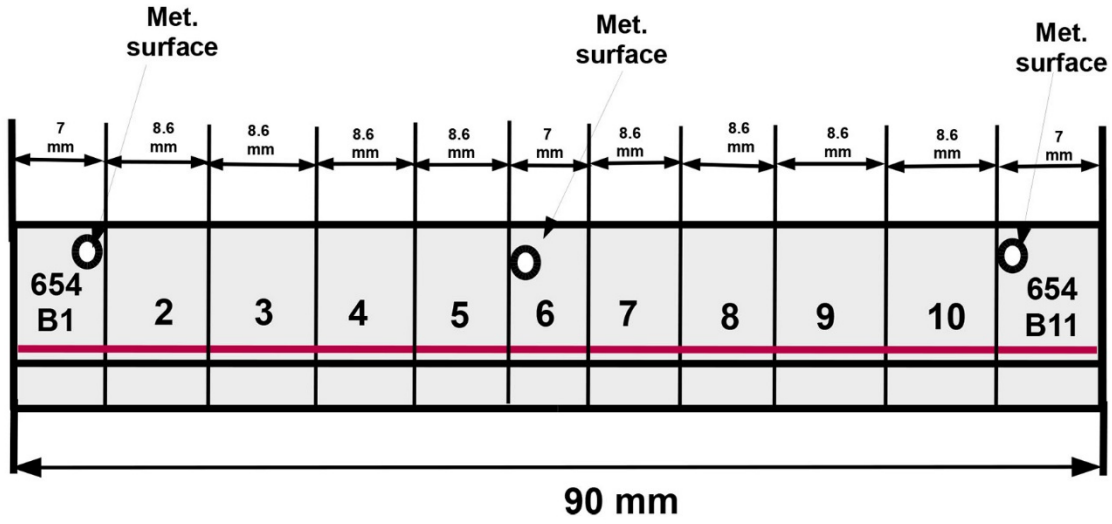

Figure 57: Pre-sectioning diagram for heat-treated M5® segment 654B. Top of segment is to the left.

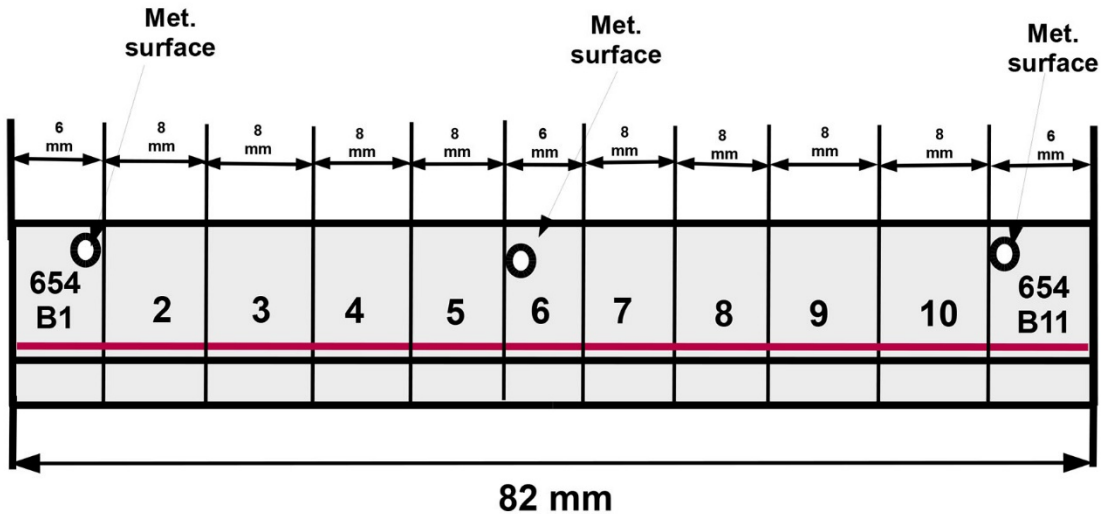

Figure 58: Post-sectioning diagram for heat-treated M5® segment 654B. Top of segment is to the left.

Prior to sectioning, the 654B-segment outer diameter was measured at three axial locations with two orientations per location. Five out of six readings gave a uniform 9.41 mm with the sixth one being 9.42 mm. Thus, the outer diameter was 9.41±0.00 mm for 654B. Two of the indicated surfaces in Fig. 57 were subjected to MET. The approximate axial locations of the two surfaces were ≈3360 mm for 654B6 and ≈3390 mm for 654B1. Based on 21 as-polished images of these surfaces at 500X magnification, the oxide layer thickness was a uniform 10±1 µm. The hydrogen content, which needs to be confirmed by direct measurement, is expected to be in the range of 80±10 wppm. Twenty-seven 100X-magnification images were used to determine the cladding wall thickness (0.568±0.005 mm). The cladding metal outer diameter was a uniform 9.39 mm and the metal inner diameter was 8.26±0.01 mm. Thus, the geometric factor in Eq. 1 is 7.28±0.07 and the pressure difference across the cladding wall is 7.14 MPa at 401°C using the measured rod internal pressure extrapolated to 25°C (3.2 MPa) and assuming a cell pressure of 0.1 MPa during FHT. The calculated wall-averaged hoop stress is 51.9±0.06 MPa, which should be rounded to 52 MPa based on measurement uncertainties. This hoop stress is considerably lower than values (89−142 MPa) used in previous ANL tests [13−15]. While 52 MPa is the hoop stress at 401°C, it must be emphasized that the relevant stress for hydride precipitation is the stress at about 65°C below the dissolution temperature (300−330°C for 70−100 wppm hydrogen). Past experience indicates that both the hoop stress at precipitation and the total hydrogen content in M5® are significant contributing factors to radial hydride length (i.e., RHCF) and DTT. The hoop stress at precipitation initiation will be calculated after the hydrogen content is measured.

The 654B surface at ≈3360 mm from the fuel rod bottom was etched and imaged at 100X− and 200X−magnification. The 20 circumferential locations imaged were ones containing radial hydrides. Therefore, the 22±15% RHCF is an upper bound of what would have been determined for full surface coverage. The maximum RHCF was 59% for the whole cross section. However, it was difficult to measure the RHCF because of the presence of numerous gaps between shorter radial hydrides and because of radial-hydride clusters. The determination of RHCF allows for ≤5−µm gaps in the radial direction between radial hydrides in the assessment of continuity. The following images at 100X and 200X magnification show the gaps between radial hydrides. These images are from the initial ground/polished/etched surface and the re-ground/re-polished/re-etched surface, which is about 0.1 mm into the initial surface.

Figures 59−60 show 100X- and 200X-magnification images of the circumferential location at which the maximum radial hydride was observed. The RHCF was assessed to be 59%. However, as observed in the 200X image (Fig. 60), the continuity of the hydride is questionable because it is composed of many shorter hydrides with ≤5-µm radial gaps between hydrides. The hydride shown in Fig. 61 appears longer than the hydride in Fig. 59. However, based on the 200X-magnification image (Fig. 62), the hydride contains two gaps >5 µm. The hydrides in Figs. 63−64 show a cluster of discontinuous hydrides with an assessed RHCF of only 20%. Figures 65−66 show thicker, more continuous radial hydrides, which are commonly observed in irradiated M5® following RHT at ≥89 MPa. The longest radial hydride in Figs. 61−62 has an RHCF of 22%.

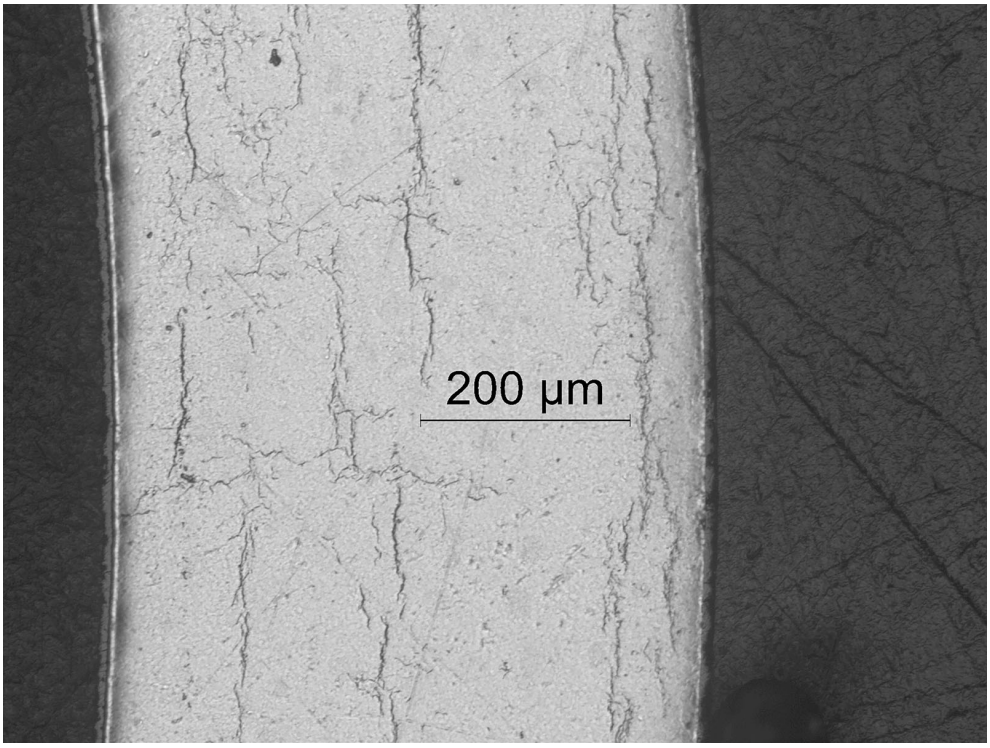

Figure 59: 100X image of the longest radial hydride (59% RHCF) observed at the 3 o'clock location of the M5® surface 654B6 located at ≈3360 mm from the bottom of FHT fuel rod 30AE14.

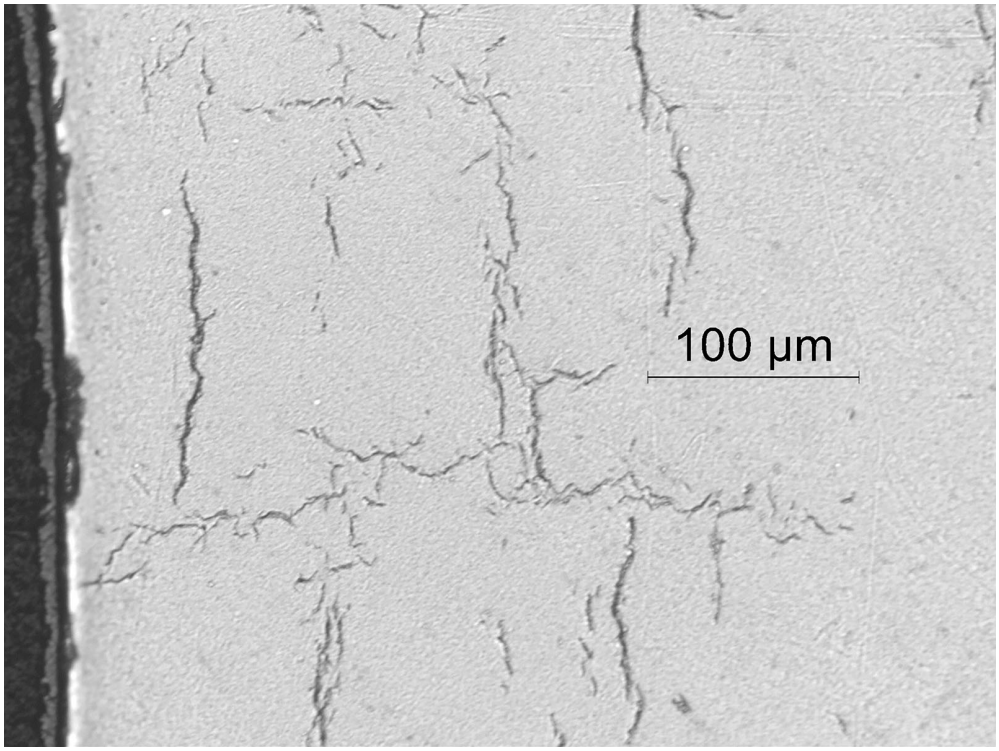

Figure 60: 200X image of the longest radial hydride (59% RHCF) observed at the 3 o'clock location of the M5® surface 654B6 located at ≈3360 mm from the bottom of FHT fuel rod 30AE14.

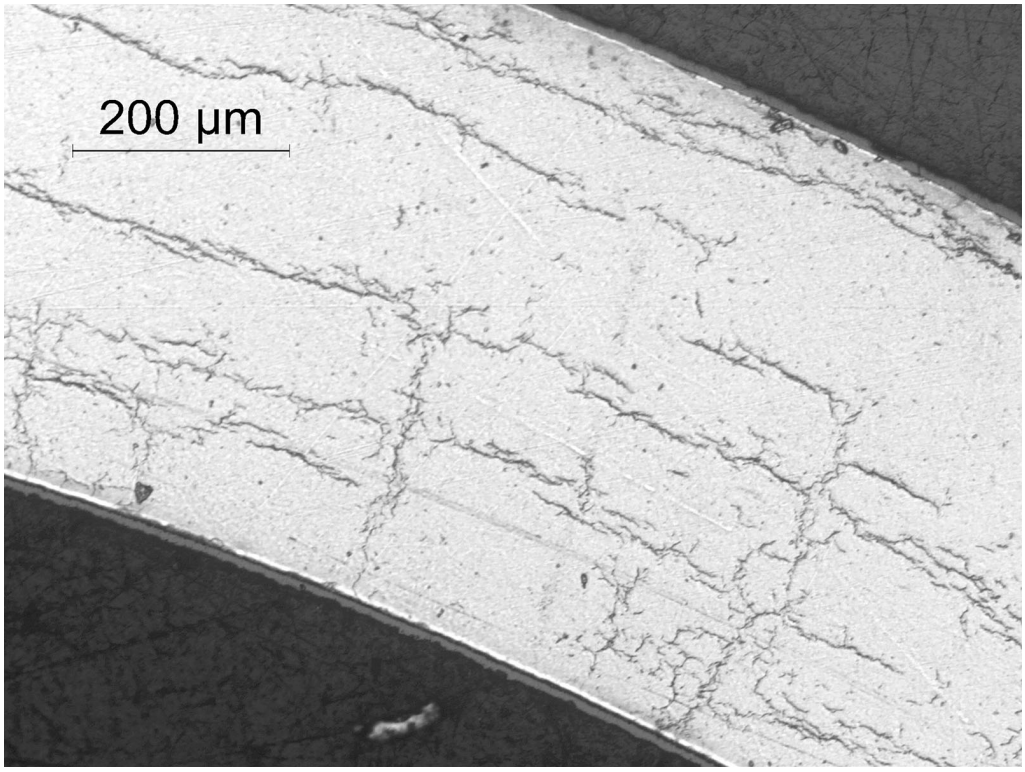

Figure 61: 100X image of a long radial hydride (56% RHCF) observed at the 2:30 o'clock location of the M5® surface 654B6 located at ≈3360 mm from the bottom of FHT fuel rod 30AE14.

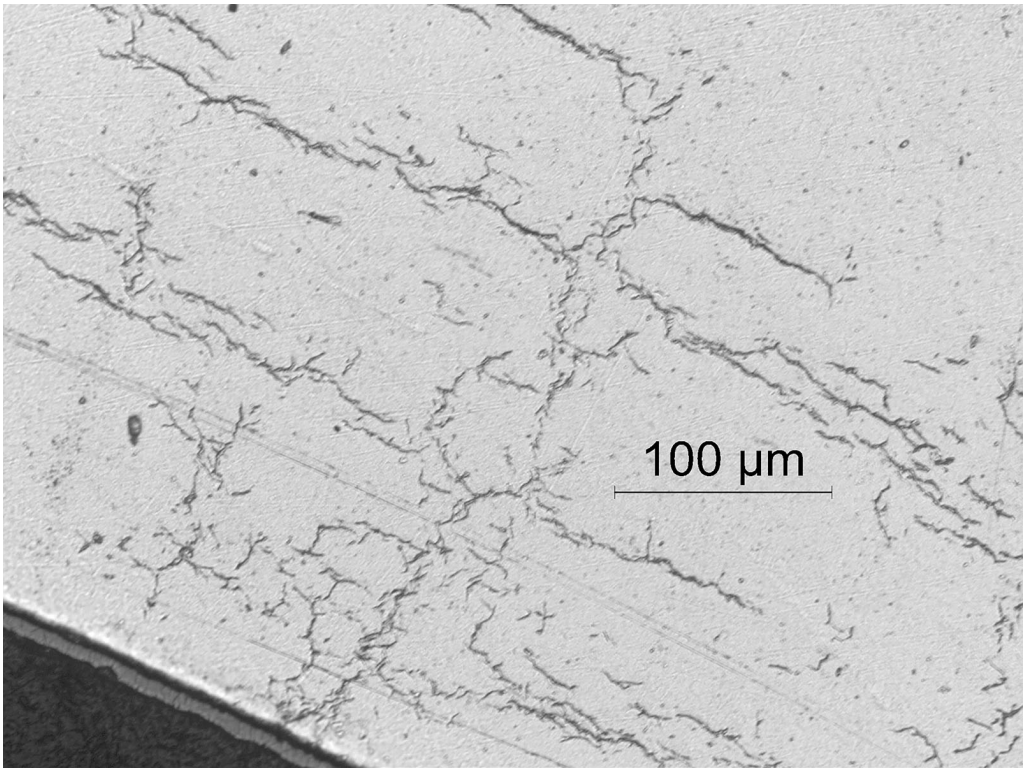

Figure 62: 200X image of a long radial hydride (56% RHCF) observed at the 2:30 o'clock location of the M5® surface 654B6 located at ≈3360 mm from the bottom of FHT fuel rod 30AE14.

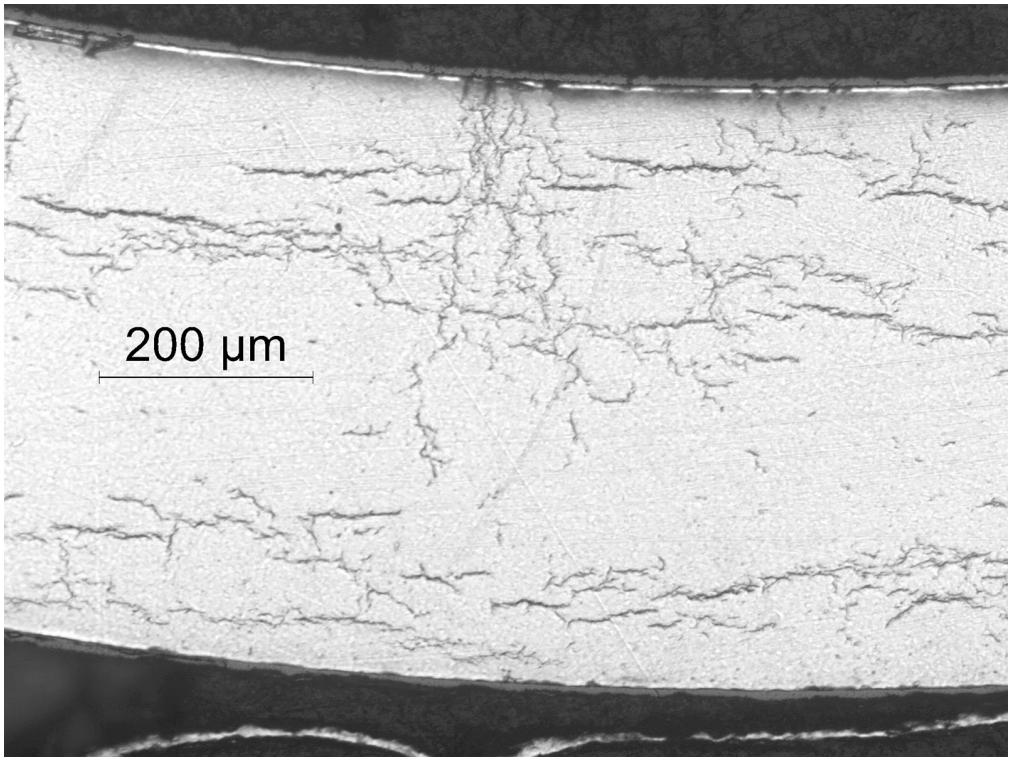

Figure 63: 100X image of a medium-length radial hydride (20% RHCF) observed at the 6 o'clock location of the M5® surface 654B6 located at ≈3360 mm from the bottom of FHT fuel rod 30AE14.

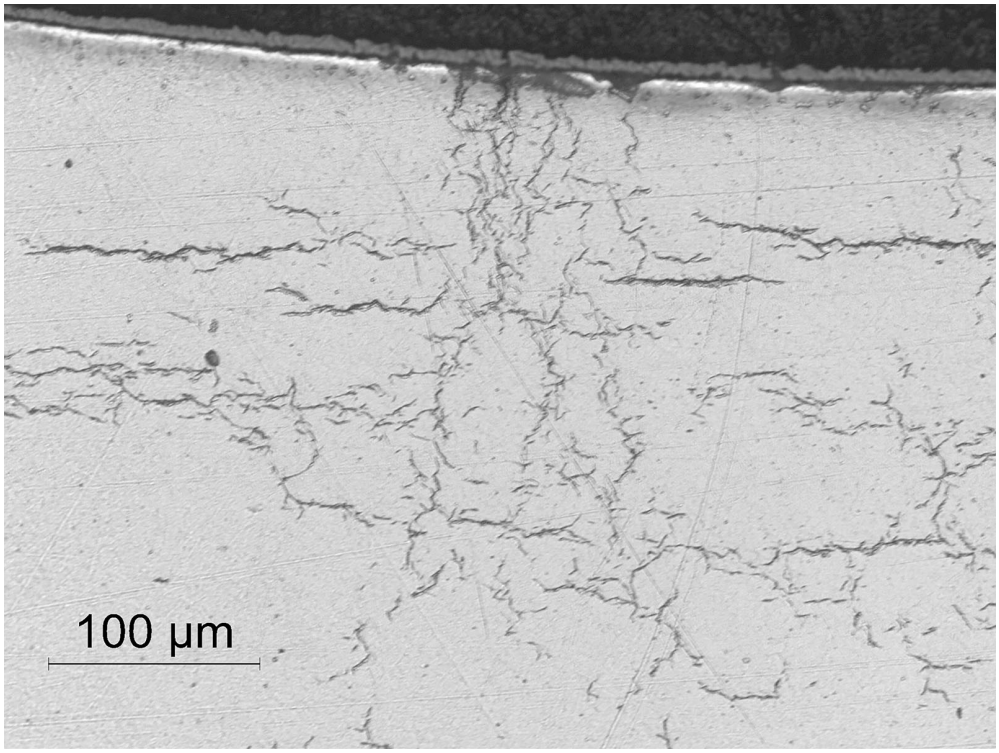

Figure 64: 200X image of a medium-length radial hydride (20% RHCF) observed at the 6 o'clock location of the M5® surface 654B6 located at ≈3360 mm from the bottom of FHT fuel rod 30AE14.

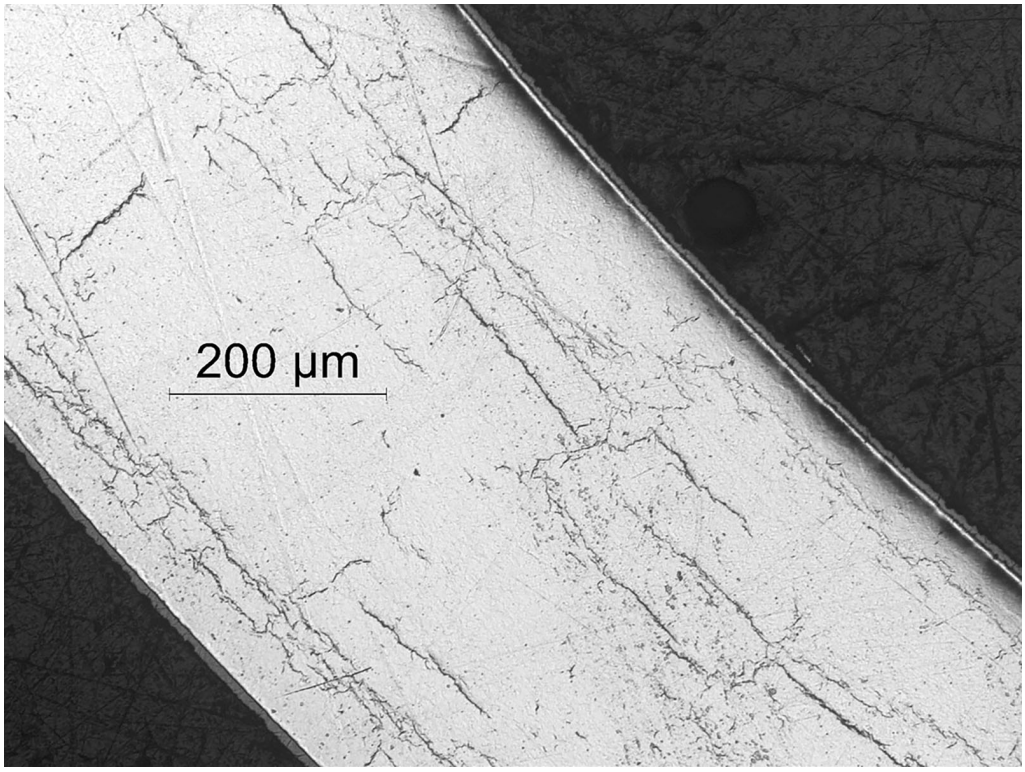

Figure 65: 100X image of a thicker radial hydride (20% RHCF) observed at the 7 o'clock location of the M5® surface 654B6 located at ≈3360 mm from the bottom of FHT fuel rod 30AE14.

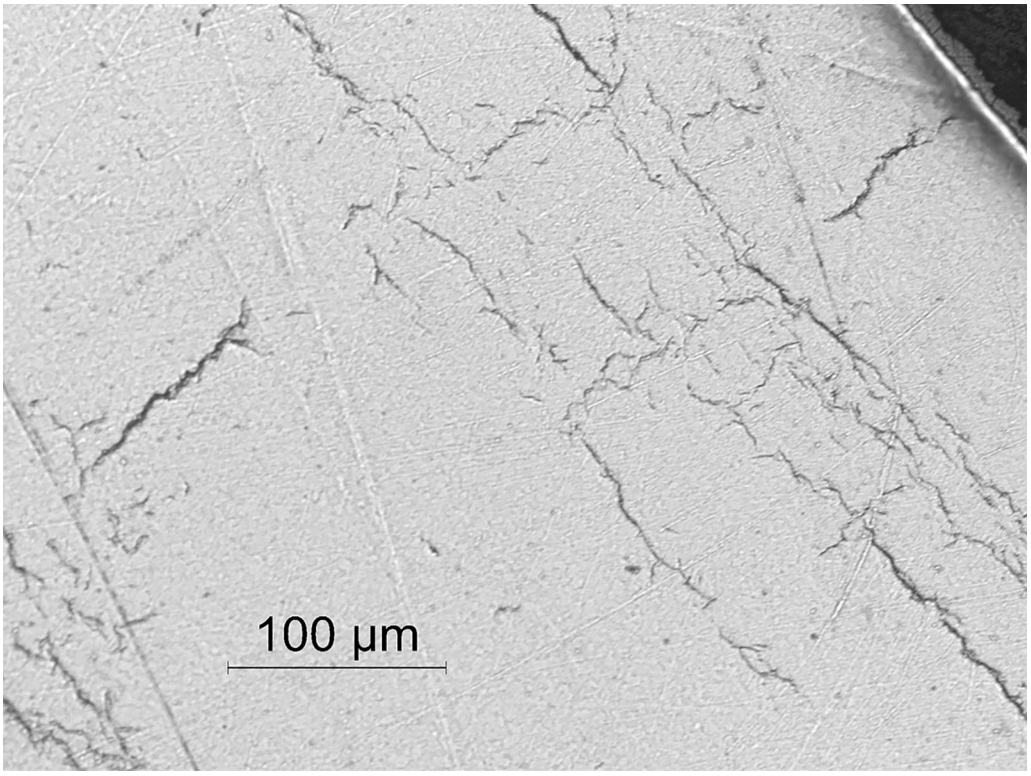

Figure 66: 200X image of a thicker radial hydride (20% RHCF) observed at the 7 o'clock location of the M5® surface 654B6 located at ≈3360 mm from the bottom of FHT fuel rod 30AE14.

Following grinding, polishing, and etching, surface 654B1 (≈3390 mm from the bottom of FHT fuel rod 30AE14) was examined at 45 circumferential locations covering the whole surface. The RHCF was 18±10% with a maximum value of 49%. Combining these results with those obtained from the 654B6 surface gives 19±12% RHCF with a maximum RHCF of 59% (from surface 654B6).

Figures 67−74 show 100X and 200X-magnification images of radial hydrides at four circumferential locations of 654B1. The radial hydrides that appear at the 2:45 o'clock location (Figs. 67−68), at the 12 o'clock location (Figs. 69−70), and the 2 o'clock location (Figs. 71−72) are similar to those shown for the 654B6 surface in that they are thin, short, clustered and have small radial gaps. The radial hydride at the 3:30 o'clock location is somewhat different in that it is not a part of a cluster of radial hydrides. While it is more traditional compared to radial hydrides precipitated in irradiated M5® after RHT at higher peak hoop stress (89−142 MPa), it does not appear to be as thick or as continuous as what has been observed.

Figures 75−78 show long radial hydrides observed previously in irradiated M5® segments following RHT at 400°C/90-MPa (Fig. 75), at 350°C/89-MPa (Fig. 76), at 400°C/111-MPa (Fig. 77), and at 400°C/142-MPa (Fig. 78). To better appreciate the combined effects of hoop stress and hydrogen content, it is useful to tabulate results and to include the hoop stress [$\sigma_\theta(T_P)$] at the hydride precipitation-initiation temperature (T_P). T_P is assumed to be 65°C lower [16] than the dissolution temperature (T_D), which increases as the hydrogen content increases [17]. The results in Table 2 show a consistent pattern for RHCF, which increases as $\sigma_\theta(T_P)$ increases: 37±17% for 67 MPa, 44±18% for 74 MPa, 54±16% for 94 MPa, and 62±17% for 127 MPa. Coincidentally, the hydrogen content of the M5® cladding segments tended to increase with the increase in $\sigma_\theta(T_P)$. The hydrogen content available for precipitation is also an important factor in the effective lengths of radial hydrides.

Sibling-pin M5® segment 654B, which was from a fuel rod subjected to FHT at 401°C/52-MPa, is expected to have a precipitation-initiation hoop stress of only about 40 MPa. For this RXA alloy, radial hydrides are likely to precipitate at such a low stress, but the radial hydrides are not expected to be as continuous in the radial and axial directions as they would be at higher precipitation-initiation hoop stresses (67−127 MPa).

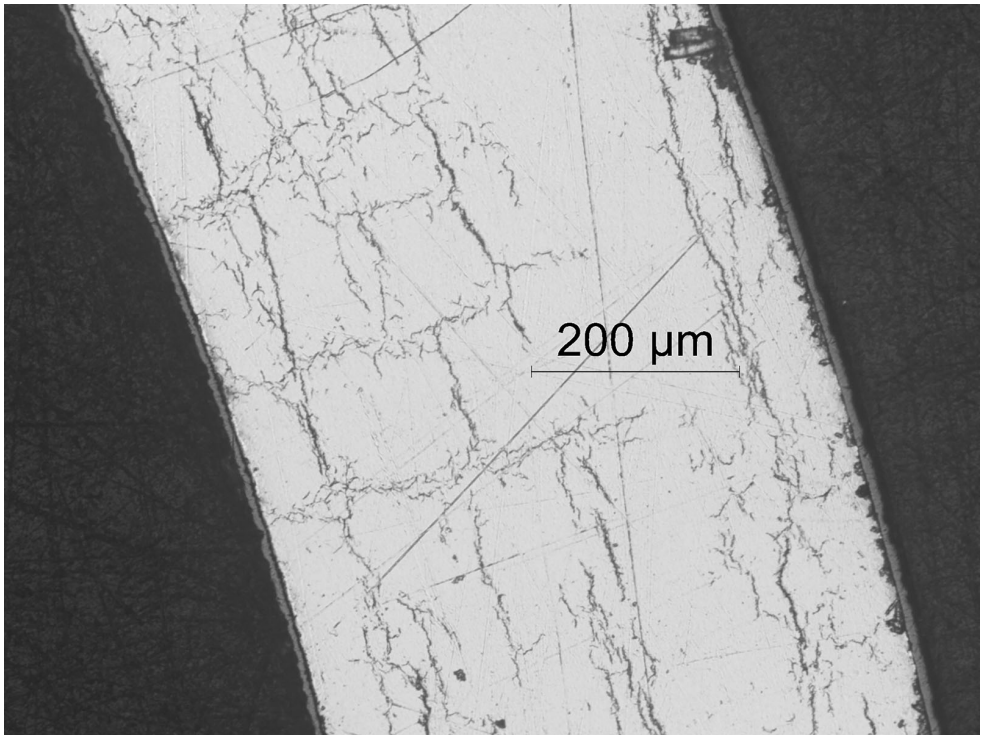

Figure 67: 100X image of the longest radial hydride (49% RHCF) observed at the 2:45 o'clock location of the M5® surface 654B1 located at ≈3390 mm from the bottom of FHT fuel rod 30AE14.

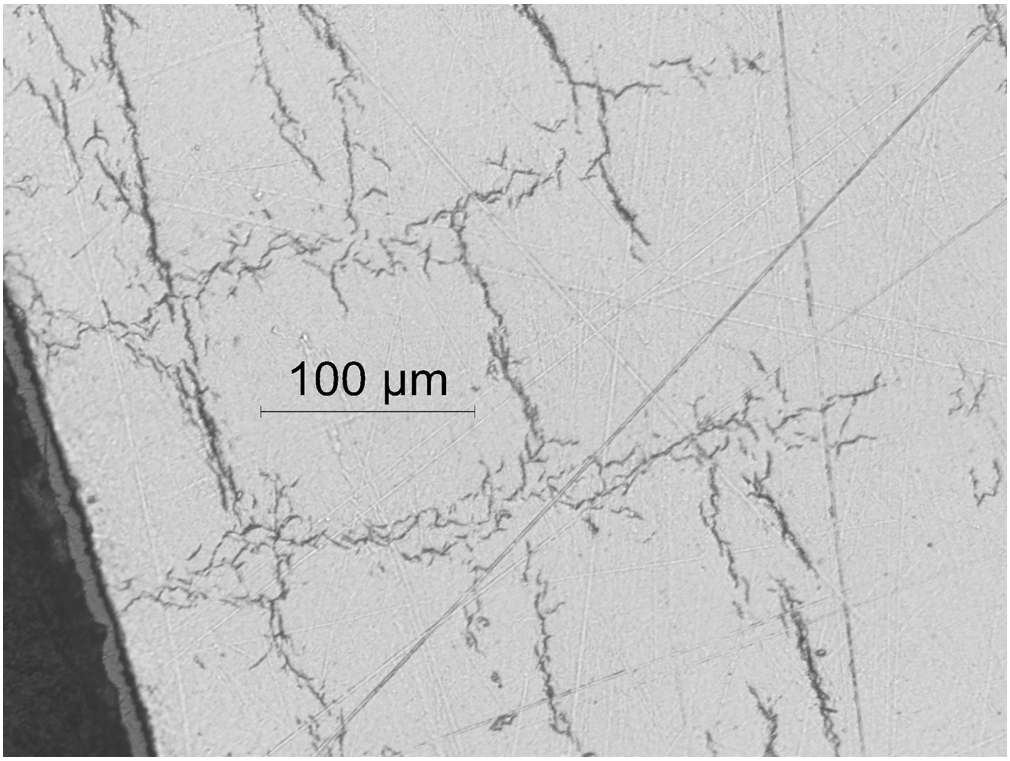

Figure 68: 200X image of the longest radial hydride (49% RHCF) observed at the 2:45 o'clock location of the M5® surface 654B1 located at ≈3390 mm from the bottom of FHT fuel rod 30AE14.

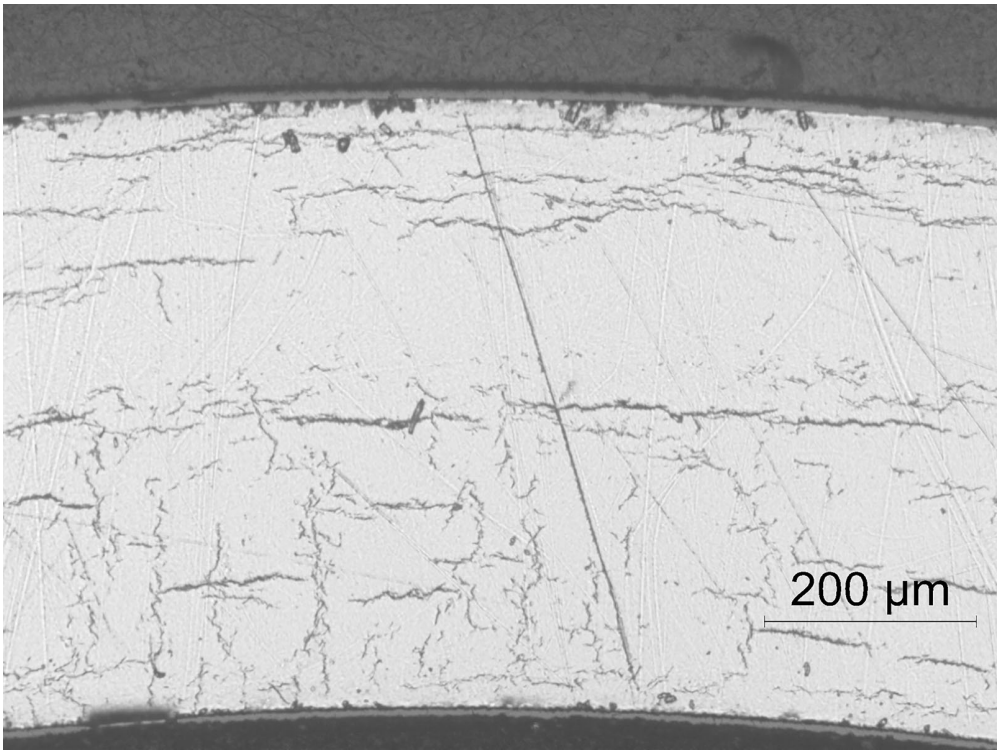

Figure 69: 100X image of a long radial hydride (40% RHCF) observed at the 12 o'clock location of the M5® surface 654B1 located at ≈3390 mm from the bottom of FHT fuel rod 30AE14.

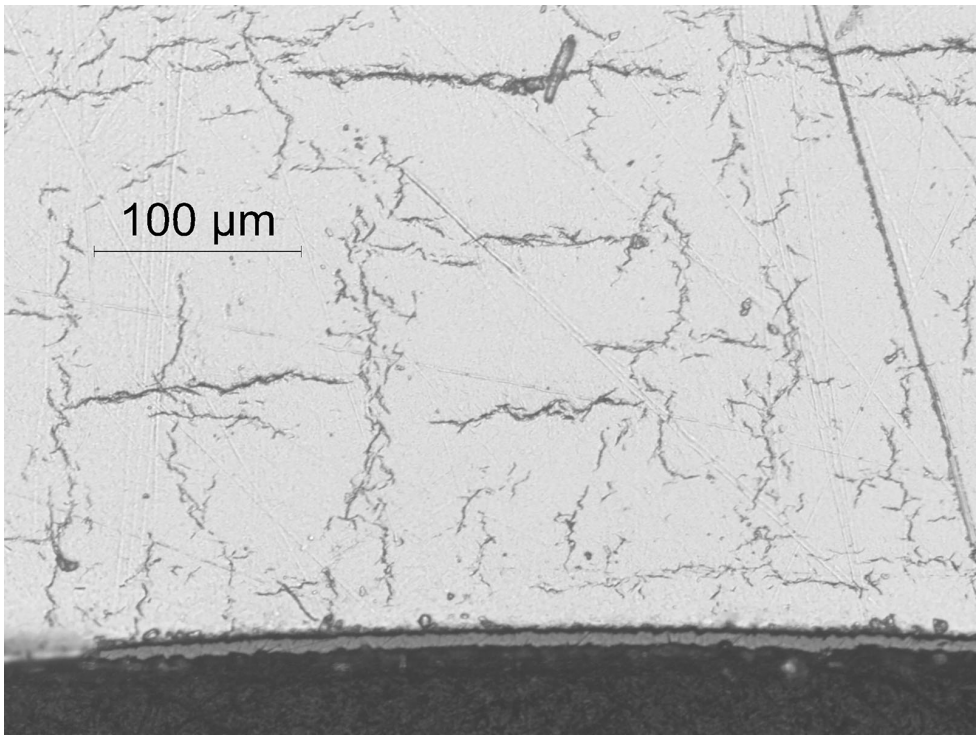

Figure 70: 200X image of a long radial hydride (40% RHCF) observed at the 12 o'clock location of the M5® surface 654B1 located at ≈3390 mm from the bottom of FHT fuel rod 30AE14.

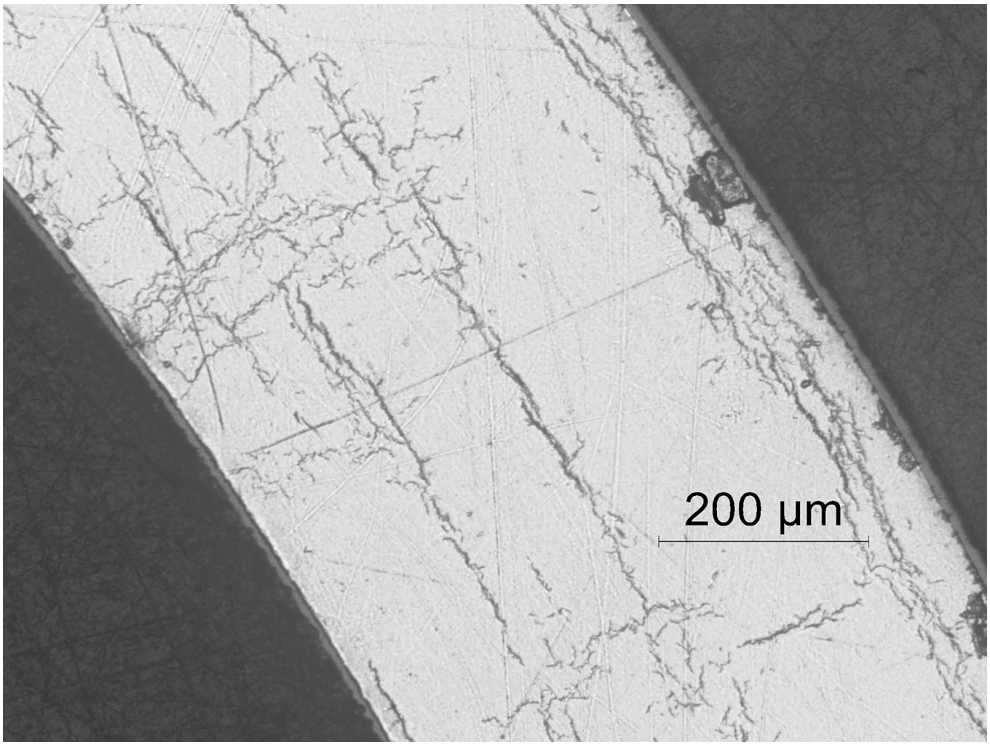

Figure 71: 100X image of a radial-hydride cluster (32% RHCF) observed at the 2 o'clock location of the M5® surface 654B1 located at ≈3390 mm from the bottom of FHT fuel rod 30AE14.

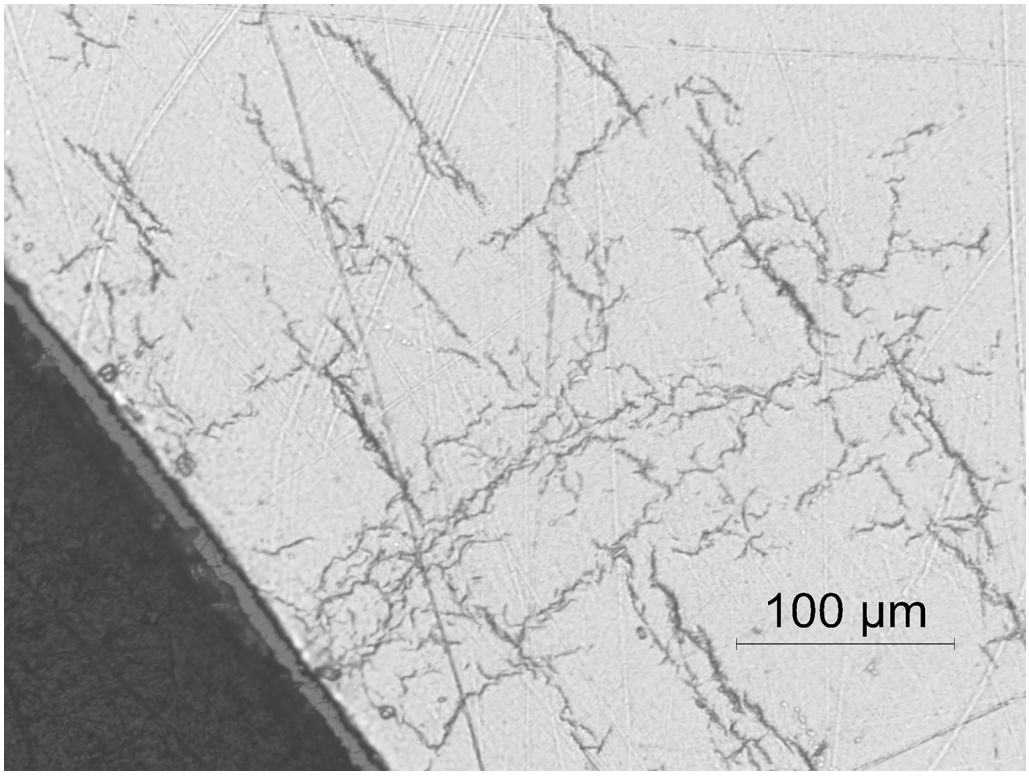

Figure 72: 200X image of a radial-hydride cluster (32% RHCF) observed at the 2 o'clock location of the M5® surface 654B1 located at ≈3390 mm from the bottom of FHT fuel rod 30AE14.

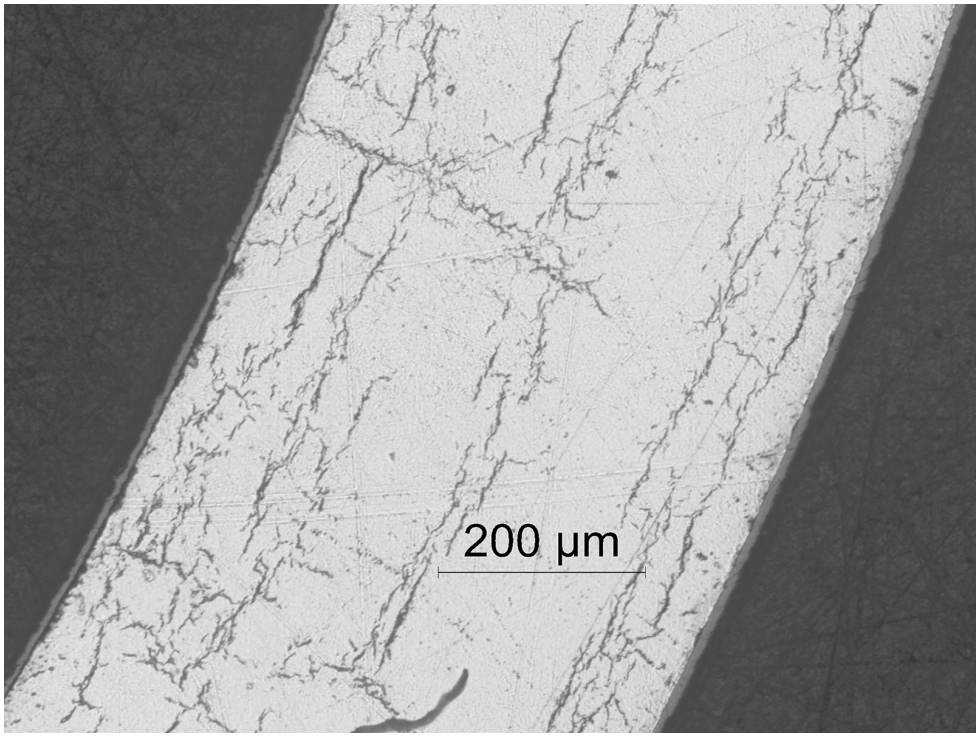

Figure 73: 100X image of a traditional radial hydride (32% RHCF) observed at the 3:30 o'clock location of the M5® surface 654B1 located at ≈3390 mm from the bottom of FHT fuel rod 30AE14.

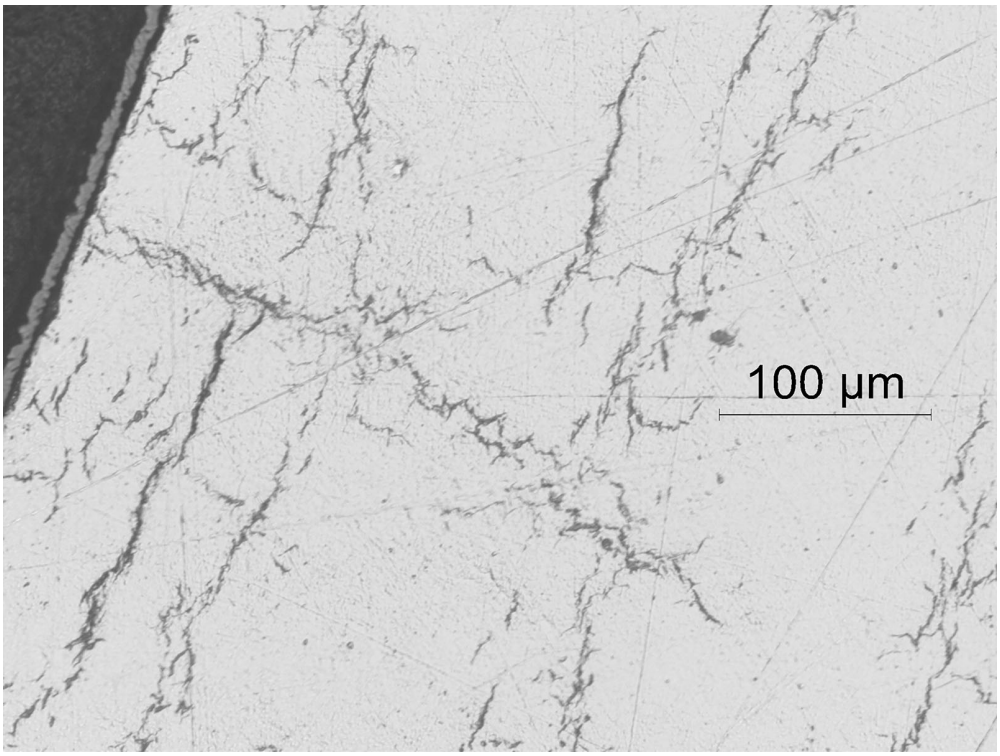

Figure 74: 200X image of a traditional radial hydride (32% RHCF) observed at the 3:30 o'clock location of the M5® surface 654B1 located ≈3390 mm from the bottom of FHT fuel rod 30AE14.

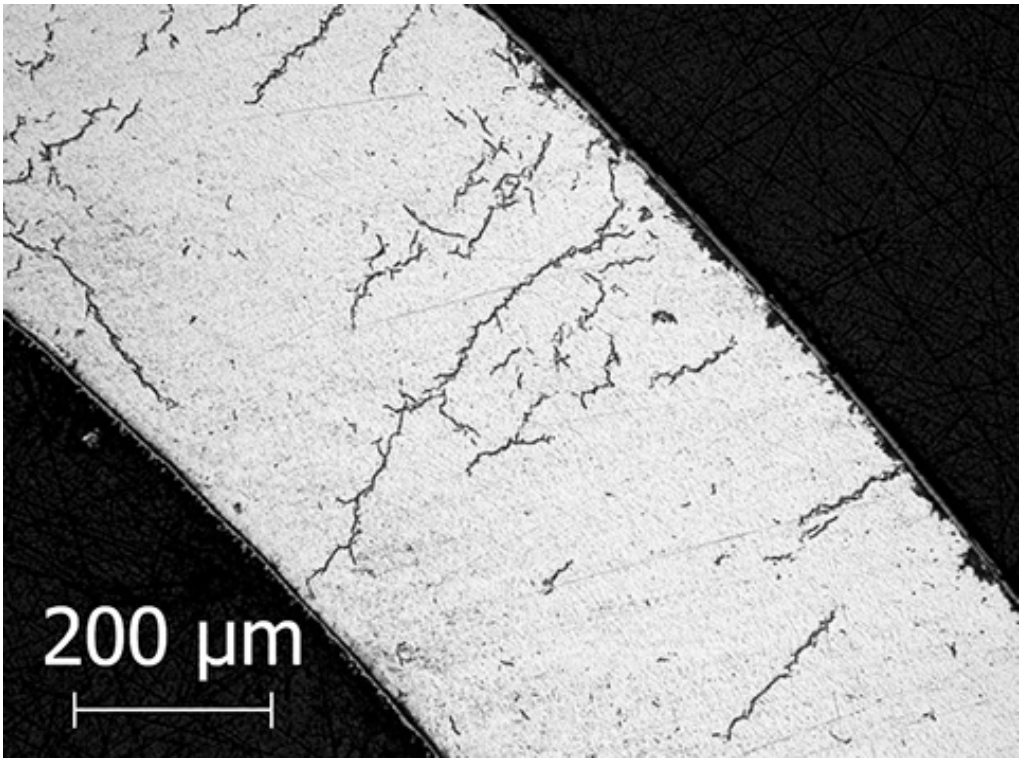

Figure 75: Longest radial hydride (80% RHCF) observed in irradiated M5® with 58±15 wppm hydrogen following RHT at 400°C/90-MPa (651E3).

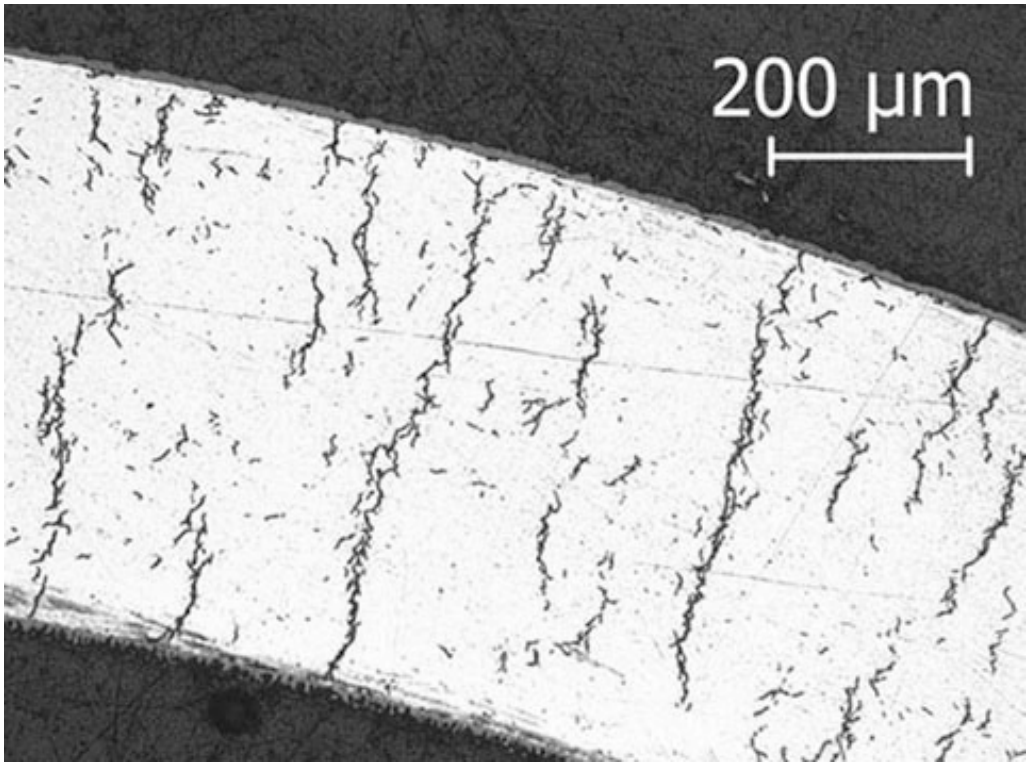

Figure 76: Longest radial hydride (≈95% RHCF) observed in irradiated M5® with 80±7 wppm hydrogen following RHT at 350°C/89-MPa (652F2).

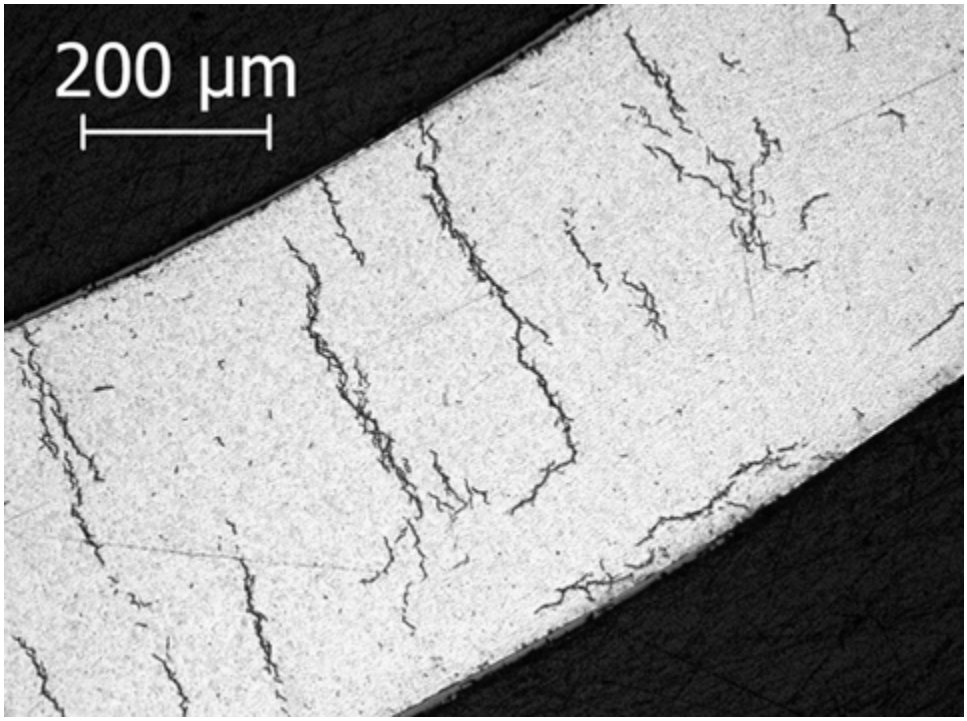

Figure 77: Long radial hydride (70% RHCF) observed in irradiated M5® with 72±10 wppm hydrogen following RHT at 400°C/111-MPa (651E5). Longer radial hydrides (100% RHCF) occurred at locations with cracks.

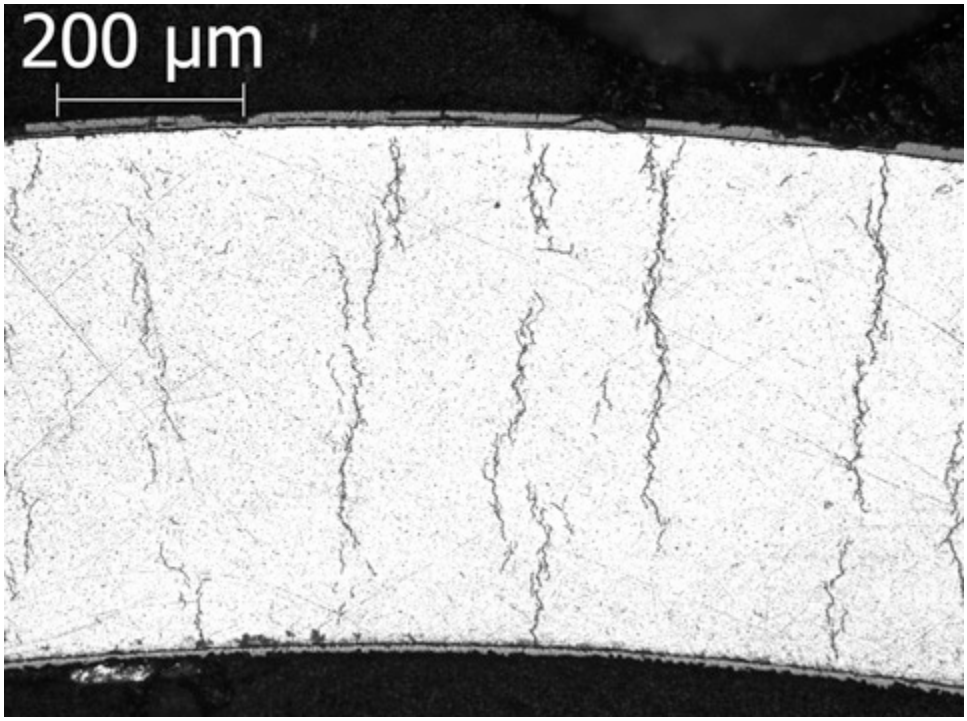

Figure 78: Long radial hydride (80% RHCF) observed in irradiated M5® with 94±6 wppm hydrogen following RHT at 400°C/142-MPa (645D). Longer radial hydrides (99% RHCF) occurred at locations with cracks.

Table 2 Summary of radial hydride results and parameters influencing radial hydride precipitation in irradiated M5® cladding segments following radial hydride treatment.

Parameter	FHT Rod 30AE14 654B	ANL Rodlet 651E3	ANL Rodlet 652F2	ANL Rodlet 651E5	ANL Rodlet 645D
Average Burnup, GWd/MTU	54	68	70	68	63
h_{ox}, µm	10±1	9±1	11±1	8±1	13±0
C_H, wppm	TBD	58±15	80±7	72±10	94±6
PCT, °C	401	400	350	400	400
T_D, °C	TBD	290	315	307	206±5
T_P, °C	TBD	335	285	285	329
σ_θ(PCT), MPa	52	90	89	111	142
$\sigma_\theta(T_P)$, MPa	TBD	67	74	94	127
Average RHCF, %	19±12	37±17	44±18	54±16	62±17
Maximum RHCF, %	59	96	100	100	99
# of Data Points	65	95	204	35	36

6. DISCUSSION AND SUMMARY

Characterization of M5® Sibling Pin Cladding

Two M5® segments were characterized: (a) from as-irradiated fuel rod 30AD05 at an axial location ≈3300 mm from the bottom of the rod and (b) from heat-treated (FHT) fuel rod 30AE14 at axial locations of ≈3360 mm and ≈3390 mm from the bottom of the fuel rod. Outer diameters (≈9.4 mm) were uniform along each 90-mm-long segment and in the expected range for the M5®-clad fuel rods irradiated to 54 GWd/MTU. The oxide layer was thicker (13 µm) for the as-irradiated segment and thinner (10 µm) for the FHT segment. These oxide layer thicknesses, along with images of hydrides, suggest C_H values of 90±10 wppm and 80±10 wppm, respectively, for as-irradiated and FHT segments. Precise values will be obtained by direct measurement. Metallographic examination results, along with diameter measurements and the ORNL-reported end-of-life (EOL) rod internal pressure (RIP) at 25°C (3.2 MPa), were used to calculate the cladding hoop stress (52 MPa) at the heat-treatment temperature (401°C) just prior to cooling initiation at 3.6°C/h. Excluding the possibility of partial annealing of irradiation damage, overheating to 485°C during the early phase of the 8-h hold time would have had no effect on radial hydride precipitation. Micro-hardness tests will be performed by ORNL to determine if partial annealing occurred during overheating. Assuming 80-wppm hydrogen content, full dissolution of hydrides would have occurred during the heating ramp at 315°C and initiation of precipitation would have occurred at 250°C during the cooling ramp at a hoop stress of about 40 MPa. The width and effective length of radial hydrides for the FHT cladding were compared to results previously obtained. In general, radial hydrides in the FHT cladding appeared thinner and more discontinuous than radial hydrides that formed during cooling at higher stress levels. Allowing for gaps of ≤5 µm between radial hydrides in the continuity assessment, the RHCF for the two FHT surfaces examined was 19±12% with a maximum value of 59%. As shown in Fig. 79, these results are consistent with previous results for irradiated M5® cladding samples with higher RHCF values after cooling at higher hoop stress levels.

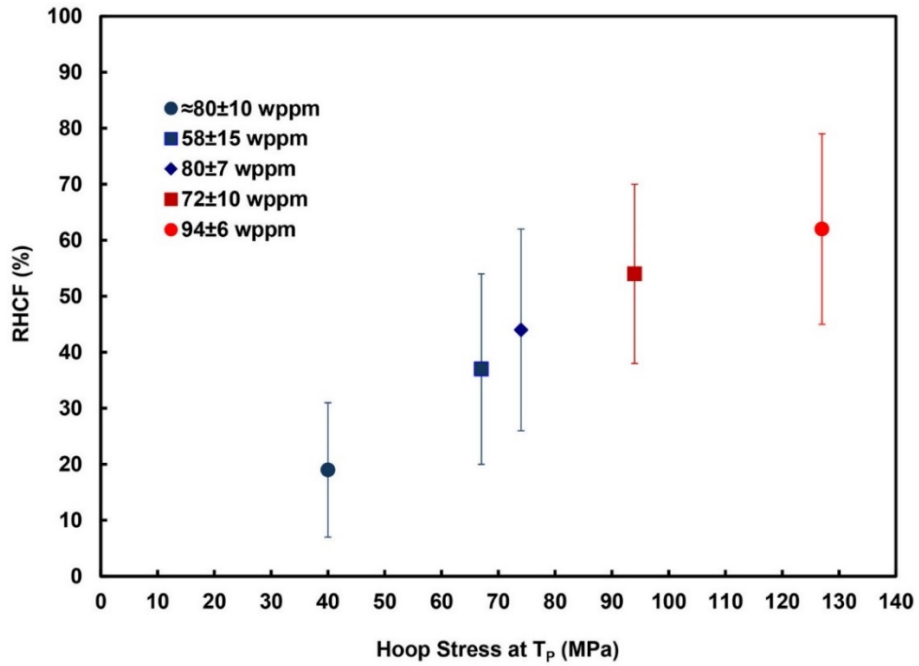

Figure 79: RHCF in irradiated M5® cladding versus hoop stress at the precipitation initiation temperature (T_P).

End-of-Life (EOL) Rod Internal Pressure (RIP)

In parallel with conducting radial-hydride related experiments, ANL has worked with ORNL, PNNL, EPRI, and international colleagues from Spain and Korea to expand the database for EOL RIP. Significant progress has been made in this area since the results presented in 2018 [19]. ORNL [4] and PNNL [5, 18] have measured EOL-RIP values for 18 sibling pins with burnups in the range of 49−60 GWd/MTU. These data are particularly important as the design and operating conditions for the 17×17 sibling pins are more consistent with current fuel rods than the legacy fuel rods irradiated during 1975−1990. Also, colleagues from the Korea Atomic Energy Research Institute (KAERI) have provided 46 data points for fuel rods irradiated to 15−58 GWd/MTU [20−21]. Figure 80 shows the legacy database and the newer data points provided by ORNL, PNNL, and KAERI. It is interesting to note that all data collected to date show that the EOL-RIP values are ≤5 MPa at 25°C. Extrapolation of 5 MPa to drying-storage temperatures, and accounting for the fuel rod external pressure during storage, suggests that peak hoop stresses will be too low to cause radial-hydride-induced embrittlement. Integral Fuel Burnable Poison (IFBA) fuel rods, with fuel-pellet coatings of a zirconium-boride compound enriched in B-10, are expected to have higher EOL-RIP values (≈6 MPa at 25°C) at <62 GWd/MTU average burnup. The IFBA fuel rods clad in ZIRLO® and Optimized ZIRLO® may have DTT values >50°C because of higher EOL RIPs. Westinghouse Electric Company (WEC) will provide EOL-RIP digital data for four IFBA fuel rods, along with data for standard UO_2 fueled rods, after the updated non-disclosure agreement has been signed by DOE National Laboratories and industry partners. The WEC-published plot in Ref. 22 contains overlapping data points, some of which may already be plotted in Fig. 80. Also, it is not yet clear that the reference temperature is 25°C for all WEC data points.

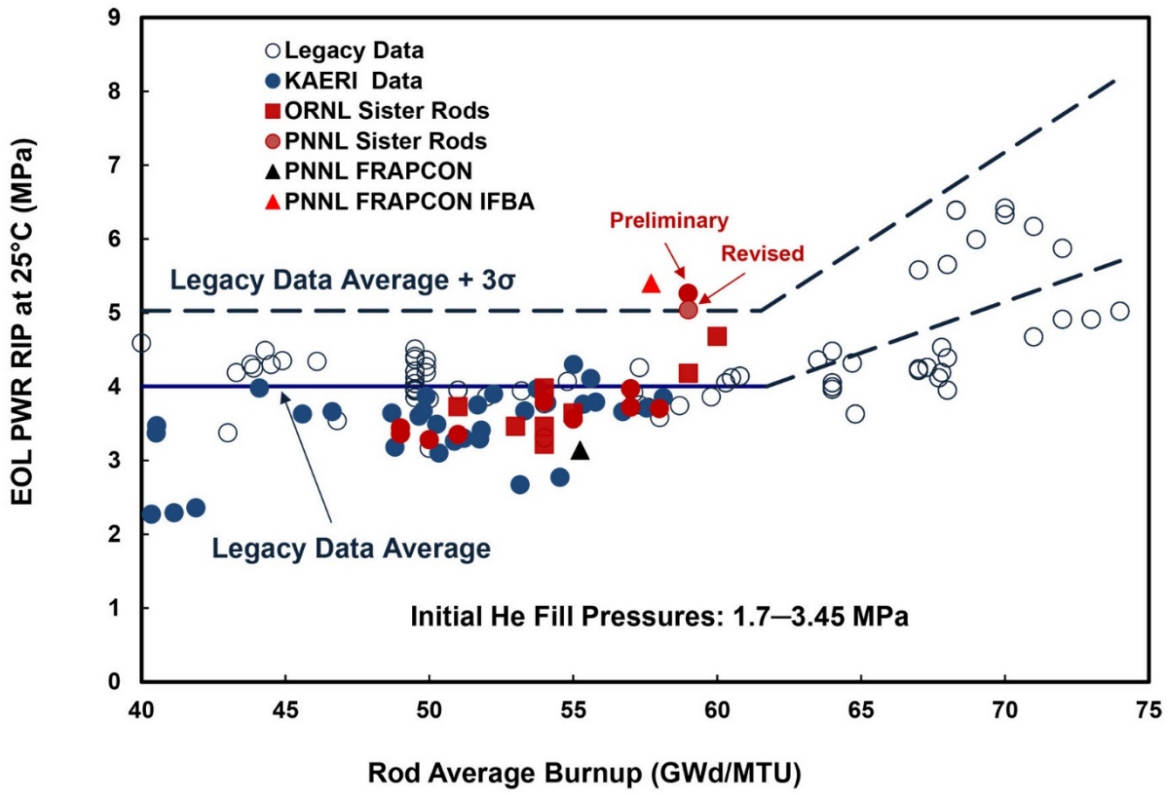

Figure 80: End-of-life (EOL) rod internal pressure (RIP) data extrapolated to 25°C for fuel rods with standard UO_2 fuel pellets clad in Zry-4, LT Zry-4, ZIRLO®, and M5®.

Ductility Transition Temperature (DTT) for HBU-Fuel ZIRLO® Cladding

Ductility data have been documented [7] for HBU-fuel ZIRLO® cladding following RHT at 350°C and 400°C and peak hoop stresses of 80-111 MPa. These samples contained a wide range of hydrogen contents (350−650 wppm), were exposed to different PCT values (including up to three temperature cycles), and had different minimum temperatures (200°C and 130°C) at which controlled 5°C/h was maintained. Although the DTT for these samples exhibited a very strong RHT-stress dependence, comparison of results was somewhat clouded by sample-to-sample differences and RHT differences. The last two tests were conducted using very similar segments that were separated by only 160 mm in the parent fuel rod and were subjected to the same RHT thermal treatment (350°C PCT, one thermal cycle, and controlled cooling at 5°C/h to 130°C). The only significant difference was the peak RHT hoop stress: (a) 87 MPa for rodlet 646D and (b) 96 MPa for rodlet 646B. The DTT for the 87-MPa RHT rodlet was 28°C. The DTT for the 96-MPa rodlet was in the range of 138±5°C depending on the validity of the ductility data point at 170°C. Section 4 presents FEA calculations and RHCF results from metallographic examinations that strongly support the validity of the data for the 170°C-tested ring that was a few mm under the top end-fixture insert. This results in a DTT of 143°C and confirms the high sensitivity of HBU-fuel ZIRLO® DTT to peak RHT hoop stresses within the range of about 90±5 MPa

RHT and RCT Guidance Document for ASTM

Sections 2−3 and part of Section 4 contain detailed procedures for conducting RHT and for both conducting RCTs and determining ductility from load-displacement curves. Analytical and experimental results generated to date are sufficient for completing the ASTM guidance document on RHT and RCT. The difference between a guidance document and a standard is that round-robin testing is required for a standard. It is difficult and perhaps pointless to conduct round-robin tests without full knowledge of the material contained in the guidance document. Following ASTM acceptance of the guidance document, consideration will be given to conducting a round robin and developing an ASTM standard.

The RHT and RCT guidance documented in Sections 2−4 contains too much detail for those not conducting or planning to conduct such tests. As such, these details will not be summarized here. However, there are four key points worth highlighting. RCT ductility is actually the ductility of the ring structure. The plastic displacement of the ring is normalized to the pre-RCT outer diameter to give the structure ductility. However, this relative displacement does not represent the plastic strain in the ring. Comparison of FEA-calculated maximum plastic strain in the ring to the structure ductility indicates that the structural ductility is generally greater than even the maximum material elastic and/or plastic strain. The second key point addressed by FEA calculations is the length of the stress discontinuity region between the welded end and the point at which the pressurized tube is subjected to axially uniform hoop stresses. This distance is about $0.6\times D_{mo}$ for samples with 9.4−9.5 mm metal outer diameter. The third key point is that the cladding ring is stress free prior to the initial elastic loading. However, for rings displaced far enough to induce material plasticity, which is highly non-uniform across the cladding wall and along the circumference, significant residual stresses are present in the ring after unloading. This difference between loading and unloading likely explains the observation that the unloading slope is always less than the loading slope for rings that experience plastic deformation. Finally, RHT hoop stresses quoted in ANL documentation, as well as by the international experimental and modeling community, are the wall-averaged hoop stresses. It is important to note the presence of a hoop-stress gradient across the cladding wall. For the last ZIRLO® test (646B), the inner-surface, average, and outer-surface hoop stresses were 103 MPa, 96 MPa, and 90 MPa, respectively. Thus, there are actually two factors that contribute to the precipitation of longer radial hydrides within the inner half of ZIRLO® cladding: (a) higher hoop stress and (b) lower concentration of circumferential hydrides at the PCT.

Page intentionally blank

REFERENCES

[1] Montgomery, Rose, Bruce Bevard, Robert N. Morris, James Goddard, Jr., Susan K. Smith, and Jianwei Hu, *Sister Rod Nondestructive Examination Final Report*, SFWD-SFWST-2017-000003 Rev. 1, ORNL/SPR-2017/484 Rev. 1, May 16, 2018.

[2] Saltzstein, Sylvia J., Mike Billone, Brady Hanson, and John Scaglione, "Visualization of the High-Burnup Spent Fuel Rod Phase 1 Test Plan: Technical Memo," SAND2018-8042 O, Jul. 18, 2018.

[3] Ahn, T., H. Akhavannik, G. Bjorkman, F.C. Chang, W. Reed, A., Rigato, D. Tang, R.D. Torres, B.H. White, and V. Wilson, *Dry Storage and Transportation of High Burnup Spent Nuclear Fuel*, NUREG-2224, July 2018 draft report for public comment.

[4] Montgomery, Rose, Robert N. Morris, Ralph Ilgner, Benjamin Roach, Jy-An Wang, Zachery Burns, James T. Dixon, and Stephanie M. Curlin, *Sister Rod Destructive Examinations (FY19)*, ORNL/SPR-2019/1251 Revision 1, Sep. 27, 2019.

[5] Shimskey, RW, JR Allred, RC Daniel, MK Edwards, J Geeting, PJ MacFarlan, LI Richmond, TS Scott, and BD Hanson, *PNNL Phase 1 Update on Sibling Pin Destructive Examination Results*, PNNL-29179, Sep. 27, 2019.

[6] Billone, M.C., "Ductility of High-Exposure ZIRLO™ Cladding following Drying and Storage", Proc. of IHLRWM 2019, Knoxville, TN, April 14-18, 2019.

[7] Billone, M.C., *Ductility of High-Burnup-Fuel ZIRLO™ following Drying and Storage*, ANL-19/14, Jun. 30, 2019 Rev. 3.

[8] Geelhood, K.J., W.G. Lusher, and C.E. Beyer, *PNNL Stress/Strain Correlation for Zircaloy*, Pacific Northwest National Laboratory Report PNNL-17700, July 2008.

[9] Geelhood, K.J., W.G. Lusher, and P.A. Raynaud, *Material Property Correlations: Comparison Between FRACAON-3.5, FRAPCON-1.5, and MATPRO*, NUREG/CR-7024, Rev. 1, October 31, 2014, ML14296A063.

[10] Billone, M.C., T.A. Burtseva, and Y. Yan, *Ductile-to-Brittle Transition Temperature for High-Burnup Zircaloy-4 and ZIRLO™ Cladding Alloys Exposed to Simulated Drying-Storage Conditions*, Argonne National Laboratory Report ANL-13/13, NRC ADAMS ML12181A238, Sept. 2012.

[11] Billone, M.C., T.A. Burtseva, and R.E. Einziger, "Ductile-to-Brittle Transition Temperature for High-Burnup Cladding Alloys Exposed to Simulated Drying-Storage Conditions," J. Nucl. Mater. **433**, 431–448 (2013).

[12] Fourgeaud, S, J. Desquines, M. Pettit, C. Getrey and G. Sert, "Mechanical characteristics of fuel rod claddings in transport conditions," Packaging, Transport, Storage & Security of Radioactive Material, Vol 20, no. 2 (2009), pp 69-76.

[13] Billone, M.C., T.A. Burtseva, and Y.Y. Liu, *Baseline Studies for Ring Compression Testing of High-Burnup Fuel Cladding*, Argonne National Laboratory Report ANL-12/58, FCRD-USED-2013-000040, Nov. 23, 2012.

[14] Billone, M.C., T.A. Burtseva, Z. Han, and Y.Y. Liu, *Embrittlement and DBTT of High-Burnup PWR Fuel Cladding Alloys*, Argonne National Laboratory Report ANL-13/16, FCRD-UFD-2013-000401, Sept. 30, 2013.

[15] Billone, M.C. and T.A. Burtseva, *Effects of Lower Drying-Storage Temperatures on the Ductility of High-Burnup PWR Cladding*, Argonne National Laboratory Report ANL-16/16, FCRD-UFD-2016-000065, Aug. 30, 2016.

[16] Kammenzind, B.F., D.G. Franklin, H.R. Peters, and W.J. Duffin, "Hydrogen Pickup and Redistribution in Alpha-Annealed Zircaloy-4," *Zirconium in the Nuclear Industry: 11th Intl. Symp.*, ASTM STP 1295, E.R. Bradley and G.P. Sabol, Eds., ASTM, pp. 338–370, 1996.

[17] Kearns, J.J., "Terminal Solubility and Partitioning of Hydrogen in the Alpha Phase of Zirconium, Zircaloy-2 and Zircaloy-4," J. Nucl. Mater. **22**, 292–303, 1967.

[18] Hanson, B.D., personal communication,"F35K13 EOL RIP" email, Dec. 3, 2019.

[19] Billone, M.C. and T.A. Burtseva, *Results of Ring Compression Tests*, Argonne National Laboratory Report ANL-18/36, SFWD-SFWST-2018-000510, Sep. 28, 2018.

[20] Kim, J., H. Yoon, D. Kook, and Y. Kim, "A Study on the Initial Characteristics of Domestic Spent Nuclear Fuels for Long Term Dry Storage," Nucl. Eng. Tech. **45**, 3 (Jun. 2013) 377−383.

[21] Kim, J., J-D Hong, Y-S Yang, and D-H Kook, "Rod internal pressure of spent nuclear fuel and its effects on cladding degradation during dry storage," J. Nucl. Mater. 492 (2017) 253-259.

[22] Pan, G., R. Montgomery, D.B. Mitchell, and B.D. Hanson, "Characteristics and Performance of ZIRLO Cladding Used Fuel," Proc. TOP FUEL 2019, Sep. 22−27, Seattle, WA, WAAP-11196.